



Jet energy scale measurements and their systematic uncertainties in proton–proton collisions at $\sqrt{s} = 13$ TeV with the ATLAS detector

The ATLAS Collaboration

Jet energy scale measurements and their systematic uncertainties are reported for jets measured with the ATLAS detector using proton–proton collision data with a center-of-mass energy of $\sqrt{s} = 13$ TeV, corresponding to an integrated luminosity of 3.2 fb^{-1} collected during 2015 at the LHC. Jets are reconstructed from energy deposits forming topological clusters of calorimeter cells, using the anti- k_r algorithm with radius parameter $R = 0.4$. Jets are calibrated with a series of simulation-based corrections and *in situ* techniques. *In situ* techniques exploit the transverse momentum balance between a jet and a reference object such as a photon, Z boson, or multijet system for jets with $20 < p_T < 2000$ GeV and pseudorapidities of $|\eta| < 4.5$, using both data and simulation. An uncertainty in the jet energy scale of less than 1% is found in the central calorimeter region ($|\eta| < 1.2$) for jets with $100 < p_T < 500$ GeV. An uncertainty of about 4.5% is found for low- p_T jets with $p_T = 20$ GeV in the central region, dominated by uncertainties in the corrections for multiple proton–proton interactions. The calibration of forward jets ($|\eta| > 0.8$) is derived from dijet p_T balance measurements. For jets of $p_T = 80$ GeV, the additional uncertainty for the forward jet calibration reaches its largest value of about 2% in the range $|\eta| > 3.5$ and in a narrow slice of $2.2 < |\eta| < 2.4$.

Contents

1	Introduction	3
2	The ATLAS detector	3
3	Jet reconstruction	5
4	Data and Monte Carlo simulation	6
5	Jet energy scale calibration	7
5.1	Pile-up corrections	7
5.2	Jet energy scale and η calibration	9
5.3	Global sequential calibration	11
5.4	<i>In situ</i> calibration methods	12
5.4.1	η -intercalibration	15
5.4.2	Z+jet and γ +jet balance	18
5.4.3	Multijet balance	22
5.4.4	<i>In situ</i> combination	23
6	Systematic uncertainties	25
7	Conclusions	31

1 Introduction

Jets are a prevalent feature of the final state in high-energy proton–proton (pp) interactions at CERN’s Large Hadron Collider (LHC). Jets, made of collimated showers of hadrons, are important elements in many Standard Model (SM) measurements and in searches for new phenomena. They are reconstructed using a clustering algorithm run on a set of input four-vectors, typically obtained from topologically associated energy deposits, charged-particle tracks, or simulated particles.

This paper details the methods used to calibrate the four-momenta of jets in Monte Carlo (MC) simulation and in data collected by the ATLAS detector [1, 2] at a center-of-mass energy of $\sqrt{s} = 13$ TeV during the 2015 data-taking period of Run 2 at the LHC. The jet energy scale (JES) calibration consists of several consecutive stages derived from a combination of MC-based methods and *in situ* techniques. MC-based calibrations correct the reconstructed jet four-momentum to that found from the simulated stable particles within the jet. The calibrations account for features of the detector, the jet reconstruction algorithm, jet fragmentation, and the busy data-taking environment resulting from multiple pp interactions, referred to as pile-up. *In situ* techniques are used to measure the difference in jet response between data and MC simulation, with residual corrections applied to jets in data only. The 2015 jet calibration builds on procedures developed for the 2011 data [3] collected at $\sqrt{s} = 7$ TeV during Run 1. Aspects of the jet calibration, particularly those related to pile-up [4], were also developed on 2012 data collected at $\sqrt{s} = 8$ TeV during Run 1.

This paper is organized as follows. Section 2 describes the ATLAS detector, with an emphasis on the sub-detectors relevant for jet reconstruction. Section 3 describes the jet reconstruction inputs and algorithms, highlighting changes in 2015. Section 4 describes the 2015 data set and the MC generators used in the calibration studies. Section 5 details the stages of the jet calibration, with particular emphasis on the 2015 *in situ* calibrations and their combination. Section 6 lists the various systematic uncertainties in the JES and describes their combination into a reduced set of nuisance parameters.

2 The ATLAS detector

The ATLAS detector consists of an inner detector tracking system spanning the pseudorapidity¹ range $|\eta| < 2.5$, sampling electromagnetic and hadronic calorimeters covering the range $|\eta| < 4.9$, and a muon spectrometer spanning $|\eta| < 2.7$. A detailed description of the ATLAS experiment can be found in Ref. [1].

Charged-particle tracks are reconstructed in the inner detector (ID), which consists of three subdetectors: a silicon pixel tracker closest to the beamline, a microstrip silicon tracker, and a straw-tube transition radiation tracker farthest from the beamline. The ID is surrounded by a thin solenoid providing an axial magnetic field of 2 T, allowing the measurement of charged-particle momenta. In preparation for Run 2, a new innermost layer of the silicon pixel tracker, the insertable B-layer (IBL) [5], was introduced at a

¹ The ATLAS reference system is a Cartesian right-handed coordinate system, with the nominal collision point at the origin. The anticlockwise beam direction defines the positive z -axis, while the positive x -axis is defined as pointing from the collision point to the center of the LHC ring and the positive y -axis points upwards. The azimuthal angle ϕ is measured around the beam axis, and the polar angle θ is measured with respect to the z -axis. Pseudorapidity is defined as $\eta = -\ln[\tan(\theta/2)]$, rapidity is defined as $y = 0.5 \ln[(E + p_z)/(E - p_z)]$, where E is the energy and p_z is the z -component of the momentum, and transverse energy is defined as $E_T = E \sin \theta$.

radial distance of 3.3 cm from the beamline to improve track reconstruction, pile-up mitigation, and the identification of jets initiated by b -quarks.

The ATLAS calorimeter system consists of inner electromagnetic calorimeters surrounded by hadronic calorimeters. The calorimeters are segmented in η and ϕ , and each region of the detector has at least three calorimeter readout layers to allow the measurement of longitudinal shower profiles. The high-granularity electromagnetic calorimeters use liquid argon (LAr) as the active material with lead absorbers in both the barrel ($|\eta| < 1.475$) and endcap ($1.375 < |\eta| < 3.2$) regions. An additional LAr presampler layer in front of the electromagnetic calorimeter within $|\eta| < 1.8$ measures the energy deposited by particles in the material upstream of the electromagnetic calorimeter. The hadronic Tile calorimeter incorporates plastic scintillator tiles and steel absorbers in the barrel ($|\eta| < 0.8$) and extended barrel ($0.8 < |\eta| < 1.7$) regions, with photomultiplier tubes (PMT) aggregating signals from a group of neighboring tiles. Scintillating tiles in the region between the barrel and the extended barrel of the Tile calorimeter serve a similar purpose to that of the presampler and were extended to increase their area of coverage during the shutdown leading up to Run 2. A LAr hadronic calorimeter with copper absorbers covers the hadronic endcap region ($1.5 < |\eta| < 3.2$). A forward LAr calorimeter with copper and tungsten absorbers covers the forward calorimeter region ($3.1 < |\eta| < 4.9$).

The analog signals from the LAr detectors are sampled digitally once per bunch crossing over four bunch crossings. Signals are converted to an energy measurement using an optimal digital filter, calculated from dedicated calibration runs [6, 7]. The signal was previously reconstructed from five bunch crossings in Run 1, but the use of four bunch crossings was found to provide similar signal reconstruction performance with a reduced bandwidth demand. The LAr readout is sensitive to signals from the preceding 24 bunch crossings during 25 ns bunch-spacing operation in Run 2. This is in contrast to the 12 bunch-crossing sensitivity during 50 ns operation in Run 1, increasing the sensitivity to out-of-time pile-up from collisions in the preceding bunch crossings. The LAr signals are shaped [6] to reduce the measurement sensitivity to pile-up, with the shaping optimized for the busier pile-up conditions at 25 ns. In contrast, the fast readout of the Tile calorimeter [8] reduces the signal sensitivity to out-of-time pile-up from collisions in neighboring bunch crossings.

The muon spectrometer (MS) [1] surrounds the ATLAS calorimeters and measures muon tracks within $|\eta| < 2.7$ using three layers of precision tracking chambers and dedicated trigger chambers. A system of three superconducting air-core toroidal magnets provides a magnetic field for measuring muon momenta.

The ATLAS trigger system begins with a hardware-based Level 1 (L1) trigger followed by a software-based high-level trigger (HLT) [9]. The L1 trigger is designed to accept events at an average 100 kHz rate, and accepted a peak rate of 70 kHz in 2015. The HLT is designed to accept events that are written out to disk at an average rate of 1 kHz and reached a peak rate of 1.4 kHz in 2015. For the trigger, jet candidates are constructed from coarse calorimeter towers using a sliding-window algorithm at L1, and are fully reconstructed in the HLT. Electrons and photons are triggered in the pseudorapidity range $|\eta| < 2.5$, where the electromagnetic calorimeter is finely segmented and track reconstruction is available. Compact electromagnetic energy deposits triggered at L1 are used as the seeds for the HLT algorithms, which are designed to identify electrons based on calorimeter and fast track reconstruction. The muon trigger at L1 is based on a coincidence of trigger chamber layers. The parameters of muon candidate tracks are then derived in the HLT by fast reconstruction algorithms in both the ID and MS. Events used in the jet calibration are selected from regions of kinematic phase space where the relevant triggers are fully efficient.

3 Jet reconstruction

The calorimeter jets used in the following studies are reconstructed at the electromagnetic energy scale (EM scale) with the anti- k_t algorithm [10] and radius parameter $R = 0.4$ using the FASTJET 2.4.3 software package [11]. A collection of three-dimensional, massless, positive-energy topological clusters (topo-clusters) [12, 13] made of calorimeter cell energies are used as input to the anti- k_t algorithm. Topo-clusters are built from neighboring calorimeter cells containing a significant energy above a noise threshold that is estimated from measurements of calorimeter electronic noise and simulated pile-up noise. The calorimeter cell energies are measured at the EM scale, corresponding to the energy deposited by electromagnetically interacting particles. Jets are reconstructed with the anti- k_t algorithm if they pass a p_T threshold of 7 GeV.

In 2015 the simulated noise levels used in the calibration of the topo-cluster reconstruction algorithm were updated using observations from Run 1 data and accounting for different data-taking conditions in 2015. This results in an increase in the simulated noise at the level of 10% with respect to the Run 1 simulation in the barrel region of the detector, and a slightly larger increase in the forward region [4]. The noise thresholds of the topo-cluster reconstruction were increased accordingly. The topo-cluster reconstruction algorithm was also improved in 2015, with topo-clusters now forbidden from being seeded by the presampler layers. This restricts jet formation from low-energy pile-up depositions that do not penetrate the calorimeters.

Jets referred to as *truth* jets are reconstructed using the anti- k_t algorithm with $R = 0.4$ using stable, final-state particles from MC generators as input. Candidate particles are required to have a lifetime of $c\tau > 10$ mm and muons, neutrinos, and particles from pile-up activity are excluded. Truth jets are therefore defined as being measured at the particle-level energy scale. Truth jets with $p_T > 7$ GeV and $|\eta| < 4.5$ are used in studies of jet calibration using MC simulation. Reconstructed calorimeter jets are geometrically matched to truth jets using the distance measurement² ΔR .

Tracks from charged particles used in the jet calibration are reconstructed within the full acceptance of the ID ($|\eta| < 2.5$). The track reconstruction was updated in 2015 to include the IBL and uses a neural network clustering algorithm [14], improving the separation of nearby tracks and the reconstruction performance in the high-luminosity conditions of Run 2. Reconstructed tracks are required to have a $p_T > 500$ MeV and to be associated with the hard-scatter vertex, defined as the primary vertex with at least two associated tracks and the largest p_T^2 sum of associated tracks. Tracks must satisfy quality criteria based on the number of hits in the ID subdetectors. Tracks are assigned to jets using ghost association [15], a procedure that treats them as four-vectors of infinitesimal magnitude during the jet reconstruction and assigns them to the jet with which they are clustered.

Muon track segments are used in the jet calibration as a proxy for the uncaptured jet energy carried by energetic particles passing through the calorimeters without being fully absorbed. The segments are partial tracks constructed from hits in the MS [16] which serve as inputs to fully reconstructed tracks. Segments are assigned to jets using the method of ghost association described above for tracks, with each segment treated as an input four-vector of infinitesimal magnitude to the jet reconstruction.

² The distance between two four-vectors is defined as $\Delta R = \sqrt{(\Delta\eta)^2 + (\Delta\phi)^2}$, where $\Delta\eta$ is their distance in pseudorapidity and $\Delta\phi$ is their azimuthal distance. The distance with respect to a jet is calculated from its principal axis.

4 Data and Monte Carlo simulation

Several MC generators are used to simulate pp collisions for the various jet calibration stages and for estimating systematic uncertainties in the JES. A sample of dijet events is simulated at next-to-leading-order (NLO) accuracy in perturbative QCD using POWHEG-Box 2.0 [17–19]. The hard scatter is simulated with a $2 \rightarrow 3$ matrix element that is interfaced with the CT10 parton distribution function (PDF) set [20]. The dijet events are showered in PYTHIA 8.186 [21], with additional radiation simulated to the leading-logarithmic approximation through p_T -ordered parton showers [22]. The simulation parameters of the underlying event, parton showering, and hadronization are set according to the A14 event tune [23]. For *in situ* analyses, samples of Z bosons with jets (Z +jet) are similarly produced with POWHEG+PYTHIA using the CT10 PDF set and the AZPHINLO event tune [24]. Samples of multijets and of photons with jets (γ +jet) are generated in PYTHIA, with the $2 \rightarrow 2$ matrix element convolved with the NNPDF2.3LO PDF set [25], and using the A14 event tune.

For studies of the systematic uncertainties, the SHERPA 2.1 [26] generator is used to simulate all relevant processes in dijet, Z +jet, and γ +jet events. SHERPA uses multileg $2 \rightarrow N$ matrix elements that are matched to parton showers following the CKKW [27] prescription. The CT10 PDF set and default SHERPA event tune are used. The multijet systematic uncertainties are studied using the Herwig++ 2.7 [28, 29] generator, with the $2 \rightarrow 2$ matrix element convolved with the CTEQ6L1 PDF set [30]. Herwig++ simulates additional radiation through angle-ordered parton showers, and is configured with the UE-EE-5 event tune [31].

Pile-up interactions can occur within the bunch crossing of interest (in-time) or in neighboring bunch crossings (out-of-time), altering the measured energy of a hard-scatter jet or leading to the reconstruction of additional, spurious jets. Pile-up effects are modeled using PYTHIA, simulated with underlying-event characteristics using the NNPDF2.3LO PDF set and A14 event tune. A number of these interactions are overlaid onto each hard-scatter event following a Poisson distribution about the mean number of additional pp collisions per bunch crossing (μ) of the event. The value of μ is proportional to the predicted instantaneous luminosity assigned to the MC event. It is simulated according to the expected distribution in the 2015 data-taking period and subsequently reweighted to the measured distribution. Events are overlaid both in-time with the simulated hard scatter and out-of-time for nearby bunches. The number of in-time and out-of-time pile-up interactions associated with an event is correlated with the number of reconstructed primary vertices (N_{PV}) and with μ , respectively, providing a method for estimating the per-event pile-up contribution.

Generated events are propagated through a full simulation [32] of the ATLAS detector based on Geant4 [33] which describes the interactions of the particles with the detector. Hadronic showers are simulated with the FTFP BERT model, whereas the QGSP BERT model was used in Run 1 [34]. A parameterized simulation of the ATLAS calorimeter called AtIfast-II (AFII) [32] is used for faster MC production, and a dedicated MC-based calibration is derived for AFII samples.

The data set used in this study consists of 3.2 fb^{-1} of pp collisions collected by ATLAS between August and December of 2015 with all subdetectors operational. The LHC was operated at $\sqrt{s} = 13 \text{ TeV}$, with bunch crossing intervals of 25 ns. The mean number of interactions per bunch crossing was estimated through luminosity measurements [35] to be on average $\langle \mu \rangle = 13.7$. The specific trigger requirements and object selections vary among the *in situ* analyses and are described in the relevant sections.

5 Jet energy scale calibration

Figure 1 presents an overview of the 2015 ATLAS calibration scheme for EM-scale calorimeter jets. This calibration restores the jet energy scale to that of truth jets reconstructed at the particle-level energy scale. Each stage of the calibration corrects the full four-momentum unless otherwise stated, scaling the jet p_T , energy, and mass.

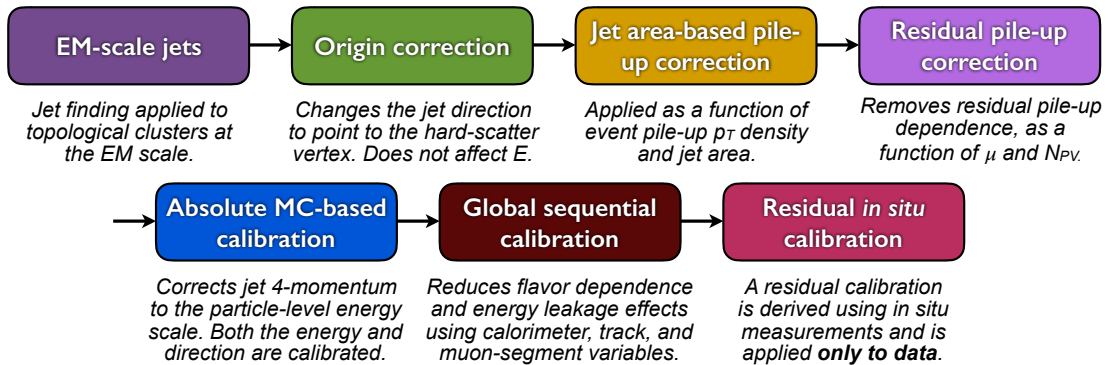


Figure 1: Calibration stages for EM-scale jets. Other than the origin correction, each stage of the calibration is applied to the four-momentum of the jet.

First, the origin correction recalculates the four-momentum of jets to point to the hard-scatter primary vertex rather than the center of the detector, while keeping the jet energy constant. This correction improves the η resolution of jets, as measured from the difference between reconstructed jets and truth jets in MC simulation. The η resolution improves from roughly 0.06 to 0.045 at a jet p_T of 20 GeV and from 0.03 to below 0.006 above 200 GeV. The origin correction procedure in 2015 is identical to that used in the 2011 calibration [3].

Next, the pile-up correction removes the excess energy due to in-time and out-of-time pile-up. It consists of two components; an area-based p_T density subtraction [15], applied at the per-event level, and a residual correction derived from the MC simulation, both detailed in Section 5.1. The *absolute* JES calibration corrects the jet four-momentum to the particle-level energy scale, as derived using truth jets in dijet MC events, and is discussed in Section 5.2. Further improvements to the reconstructed energy and related uncertainties are achieved through the use of calorimeter, MS, and track-based variables in the global sequential calibration, as discussed in Section 5.3. Finally, a residual *in situ* calibration is applied to correct jets in data using well-measured reference objects, including photons, Z bosons, and calibrated jets, as discussed in Section 5.4. The full treatment and reduction of the systematic uncertainties is discussed in Section 6.

5.1 Pile-up corrections

The pile-up contribution to the JES in the 2015 data-taking environment differs in several ways from Run 1. The larger center-of-mass energy affects the jet p_T dependence on pile-up-sensitive variables, while the switch from 50 to 25 ns bunch spacing increases the amount of out-of-time pile-up. In addition, the higher topo-clustering noise thresholds alter the impact of pile-up on the JES. The pile-up correction is

therefore evaluated using updated MC simulations of the 2015 detector and beam conditions. The pile-up correction in 2015 is derived using the same methods developed in 2012 [4], summarized in the following paragraphs.

First, an area-based method subtracts the per-event pile-up contribution to the p_T of each jet according to its area. The pile-up contribution is calculated from the median p_T density ρ of jets in the η - ϕ plane. The calculation of ρ uses only positive-energy topo-clusters with $|\eta| < 2$ that are clustered using the k_t algorithm [10, 36] with radius parameter $R = 0.4$. The k_t algorithm is chosen for its sensitivity to soft radiation, and is only used in the area-based method. The central $|\eta|$ selection is necessitated by the higher calorimeter occupancy in the forward region. The p_T density of each jet is taken to be p_T/A , where the area A of a jet is calculated using ghost association. In this procedure, simulated ghost particles of infinitesimal momentum are added uniformly in solid angle to the event before jet reconstruction. The area of a jet is then measured from the relative number of ghost particles associated with a jet after clustering. The median of the p_T density is used for ρ to reduce the bias from hard-scatter jets which populate the high- p_T tails of the distribution.

The ρ distribution of events with a given N_{PV} is shown for MC simulation in Figure 2, and has roughly the same magnitude at 13 TeV as seen at 8 TeV. At 13 TeV the increase in the center-of-mass energy is offset by the higher noise thresholds and the larger out-of-time pile-up, the latter reducing the average energy readout of any given cell due to the inherent pile-up suppression of the bipolar shaping of LAr signals [6]. The ratio of the ρ -subtracted jet p_T to the uncorrected jet p_T is taken as a correction factor applied to the jet four-momentum, and does not affect the jet η and ϕ coordinates.

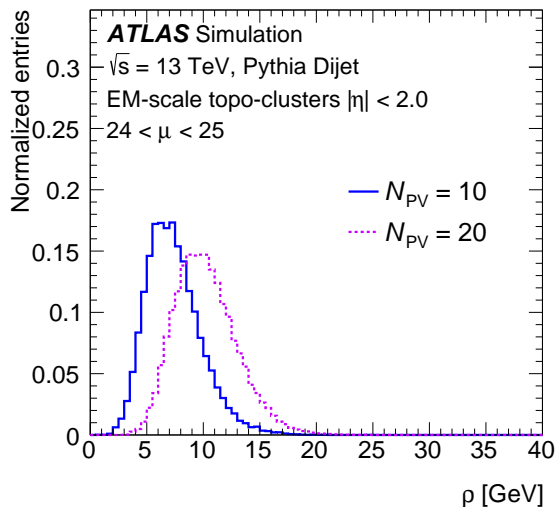


Figure 2: Per-event median p_T density, ρ , at $N_{PV} = 10$ (solid) and $N_{PV} = 20$ (dotted) for $24 < \mu < 25$ as found in MC simulation.

The ρ calculation is derived from the central, lower-occupancy regions of the calorimeter, and does not fully describe the pile-up sensitivity in the forward calorimeter region or in the higher-occupancy core of high- p_T jets. It is therefore observed that after this correction some dependence of the anti- k_t jet p_T on the amount of pile-up remains, and an additional residual correction is derived. A dependence is seen on N_{PV} , sensitive to in-time pile-up, and μ , sensitive to out-of-time pile-up. The residual p_T dependence is measured as the difference between the reconstructed jet p_T and truth jet p_T , with the latter being

insensitive to pile-up. Reconstructed jets with $p_T > 10$ GeV are geometrically matched to truth jets within $\Delta R = 0.3$.

The residual p_T dependence on N_{PV} (α) and on μ (β) are observed to be fairly linear and independent of one another, as was found in 2012 MC simulation. Linear fits are used to derive the initial α and β coefficients separately in bins of p_T^{truth} and $|\eta|$. Both the α and β coefficients are then seen to have a logarithmic dependence on p_T^{truth} , and logarithmic fits are performed in the range $20 < p_T^{\text{truth}} < 200$ GeV for each bin of $|\eta|$. In each $|\eta|$ bin, the fitted value at $p_T^{\text{truth}} = 25$ GeV is taken as the nominal α and β coefficients, reflecting the dependence in the p_T region where pile-up is most relevant. The logarithmic fits over the full p_T^{truth} range are used for a p_T -dependent systematic uncertainty in the residual pile-up dependence. Finally, linear fits are performed to the binned coefficients as a function of $|\eta|$ in 4 regions, $|\eta| < 1.2$, $1.2 < |\eta| < 2.2$, $2.2 < |\eta| < 2.8$, and $2.8 < |\eta| < 4.5$. This reduces the effects of statistical fluctuations and allows the α and β coefficients to be smoothly sampled in $|\eta|$, particularly in regions of varying dependence. The pile-up-corrected p_T , after the area-based and residual corrections, is given by

$$p_T^{\text{corr}} = p_T^{\text{reco}} - \rho \times A - \alpha \times (N_{PV} - 1) - \beta \times \mu,$$

where p_T^{reco} refers to the EM-scale p_T of the reconstructed jet before any pile-up corrections are applied.

The dependence of the area-based and residual corrections on N_{PV} and μ are shown as a function of $|\eta|$ in Figure 3. The shape of the residual correction is comparable to that found in 2012 MC simulation, except in the forward region ($|\eta| > 2.5$) of Figure 3(a), where it is found to be larger by 0.2 GeV. This difference in the in-time pile-up term is primarily caused by higher topo-cluster noise thresholds, which are more consequential in the forward region.

Two *in situ* validation studies are performed and no statistically significant difference is observed in the jet p_T dependence on N_{PV} or μ between 2015 data and MC simulation. Four systematic uncertainties are introduced to account for MC mismodeling of N_{PV} , μ , and the ρ topology, as well as the p_T dependence of the N_{PV} and μ terms used in the residual pile-up correction. The ρ topology uncertainty encapsulates the uncertainty in the underlying event contribution to ρ through the use of several distinct MC event generators and final-state topologies. The uncertainties in the modeling of N_{PV} and μ are taken as the difference between MC simulation and data in the *in situ* validation studies. The p_T -dependent uncertainty in the residual pile-up dependence is derived from the full logarithmic fits to α and β . Both the *in situ* validation studies and the systematic uncertainties are described in detail in Ref. [4].

5.2 Jet energy scale and η calibration

The *absolute* jet energy scale and η calibration corrects the reconstructed jet four-momentum to the particle-level energy scale and accounts for biases in the jet η reconstruction. Such biases are primarily caused by the transition between different calorimeter technologies and sudden changes in calorimeter granularity. The calibration is derived from the PYTHIA MC sample using reconstructed jets after the application of the origin and pile-up corrections. The JES calibration is derived first as a correction of the reconstructed jet energy to the truth jet energy [3]. Reconstructed jets are geometrically matched to truth jets within $\Delta R = 0.3$. Only isolated jets are used, to avoid any ambiguities in the matching of calorimeter jets to truth jets. An isolated calorimeter jet is required to have no other calorimeter jet of $p_T > 7$ GeV within $\Delta R = 0.6$, and only one truth jet of $p_T^{\text{truth}} > 7$ GeV within $\Delta R = 1.0$.

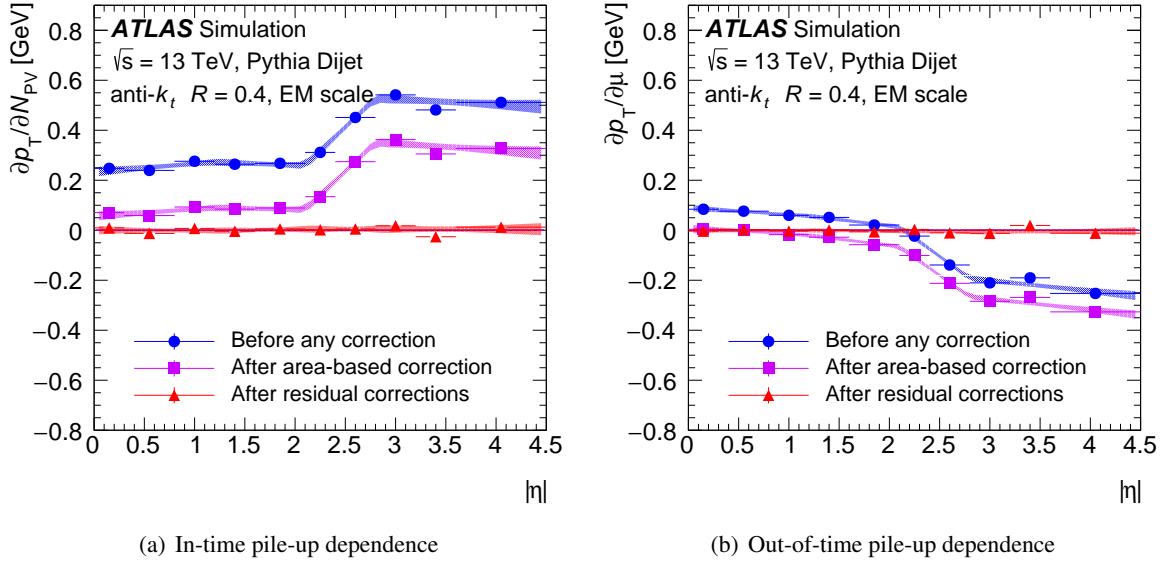


Figure 3: Dependence of EM-scale anti- k_t jet p_T on (a) in-time pile-up (N_{PV} averaged over μ) and (b) out-of-time pile-up (μ averaged over N_{PV}) as a function of $|\eta|$ for $p_T^{\text{truth}} = 25$ GeV. The dependence is shown in bins of $|\eta|$ before pile-up corrections (blue circle), after the area-based correction (violet square), and after the residual correction (red triangle). The shaded bands represent the 68% confidence intervals of the linear fits in 4 regions of $|\eta|$. The values of the fitted dependence on in-time and out-of-time pile-up after the area-based correction (purple shaded band) are taken as the residual correction factors α and β , respectively.

The average energy response is defined as the mean of a Gaussian fit to the core of the $E^{\text{reco}}/E^{\text{truth}}$ distribution for jets, binned in E^{truth} and η_{det} . The response is derived as a function of η_{det} , the jet η pointing from the geometric center of the detector, to remove any ambiguity as to which region of the detector is measuring the jet. The response in the full ATLAS simulation is shown in Figure 4(a). Gaps and transitions between calorimeter subdetectors result in a lower energy response due to absorbed or undetected particles, evident when parameterized by η_{det} . A numerical inversion procedure is used to derive corrections in E^{reco} from E^{truth} , as detailed in Ref. [13]. The average response is parameterized as a function of E^{reco} and the jet calibration factor is taken as the inverse of the average energy response. Good closure of the JES calibration is seen across the entire η range, compatible with that seen in the 2011 calibration. As in 2011, a small non-closure on the order of a few percent is seen for low- p_T jets due to a slightly non-Gaussian energy response and jet reconstruction threshold effects, both of which impact the response fits.

A bias is seen in the reconstructed jet η , shown in Figure 4(b) as a function of $|\eta_{\text{det}}|$. It is largest in jets that encompass two calorimeter regions with different energy responses caused by changes in calorimeter geometry or technology. This artificially increases the energy of one side of the jet with respect to the other, altering the reconstructed four-momentum. The barrel–endcap ($|\eta_{\text{det}}| \sim 1.4$) and endcap–forward ($|\eta_{\text{det}}| \sim 3.1$) transition regions can be clearly seen in Figure 4(b) as susceptible to this effect. A second correction is therefore derived as the difference between the reconstructed η^{reco} and truth η^{truth} , parameterized as a function of E^{truth} and η_{det} . A numerical inversion procedure is again used to derive corrections in E^{reco} from E^{truth} . Unlike the other calibration stages, the η calibration alters only the jet p_T and η , not the full four-momentum. Jets calibrated with the full jet energy scale and η calibration are considered to

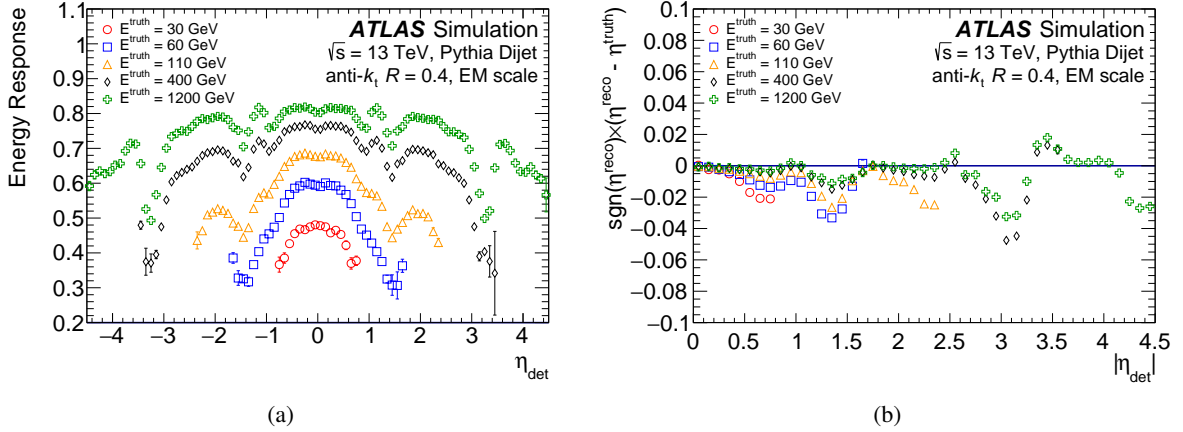


Figure 4: (a) The average energy response as a function of η_{det} for jets of a truth energy of 30, 60, 110, 400, and 1200 GeV. The energy response is shown after origin and pile-up corrections are applied. (b) The signed difference between the truth jet η^{truth} and the reconstructed jet η^{reco} due to biases in the jet reconstruction. This bias is addressed with an η correction applied as a function of η_{det} .

be at the EM+JES.

An *absolute* JES and η calibration is also derived for fast simulation samples using the same methods with a PYTHIA MC sample simulated with AFII. An additional JES uncertainty is introduced for AFII samples to account for a small non-closure in the calibration, particularly beyond $|\eta| \sim 3.2$, due to the approximate treatment of hadronic showers in the forward calorimeters. This uncertainty is about 1% at a jet p_T of 20 GeV and falls rapidly with increasing p_T .

5.3 Global sequential calibration

Following the previous jet calibrations, residual dependencies of the JES on longitudinal and transverse features of the jet are observed. The calorimeter response and the jet reconstruction are sensitive to fluctuations in the jet particle composition and the distribution of energy within the jet. The average particle composition and shower shape of a jet varies between initiating particles, most notably between quark- and gluon-initiated jets. A quark-initiated jet will often include hadrons with a higher fraction of the jet p_T that penetrate further into the calorimeter, while a gluon-initiated jet will typically contain more particles of softer p_T , leading to a lower calorimeter response and a wider transverse profile. Five observables are identified that improve the resolution of the JES through the global sequential calibration (GSC), a procedure explored in the 2011 calibration [13].

For each observable, an independent jet four-momentum correction is derived as a function of p_T^{truth} and $|\eta_{\text{det}}|$ by inverting the reconstructed jet response in MC events. Both the numerical inversion procedure and the method to geometrically match reconstructed jets to truth jets are outlined in Section 5.2. An overall constant is multiplied to each numerical inversion to ensure the average energy is unchanged at each stage. The effect of each correction is therefore to remove the dependence of the jet response on each observable while conserving the overall energy scale at the EM+JES. Corrections for each observable are applied independently and sequentially to the jet four-momentum, neglecting correlations between observables.

No improvement in resolution was found from including such correlations or altering the sequence of the corrections.

The five stages of the GSC account for the dependence of the jet response on (in order):

1. f_{Tile0} , the fraction of jet energy measured in the first layer of the hadronic Tile calorimeter ($|\eta_{\text{det}}| < 1.7$);
2. f_{LAr3} , the fraction of jet energy measured in the third layer of the electromagnetic LAr calorimeter ($|\eta_{\text{det}}| < 3.5$);
3. n_{trk} , the number of tracks with $p_{\text{T}} > 1$ GeV ghost-associated with the jet ($|\eta_{\text{det}}| < 2.5$);
4. \mathcal{W}_{trk} , the average p_{T} -weighted transverse distance in the η - ϕ plane between the jet axis and all tracks of $p_{\text{T}} > 1$ GeV ghost-associated to the jet ($|\eta_{\text{det}}| < 2.5$);
5. n_{segments} , the number of muon track segments ghost-associated with the jet ($|\eta_{\text{det}}| < 2.7$).

The n_{segments} correction reduces the tails of the response distribution caused by high- p_{T} jets that are not fully contained in the calorimeter, referred to as punch-through jets. The first four corrections are derived as a function of jet p_{T} , while the punch-through correction is derived as a function of jet energy, being more correlated with the energy escaping the calorimeters.

The underlying distributions of these five observables are fairly well modeled by MC simulation. Slight differences with data have a negligible impact on the GSC as long as the dependence of the average jet response on the observables is well modeled in MC simulation. This average response dependence was tested using the dijet tag-and-probe method developed in 2011 and detailed in Section 12.1 of Ref. [13]. The average p_{T} asymmetry between back-to-back jets was again measured in 2015 data as a function of each observable and found to be compatible between data and MC simulation, with differences small compared to the size of the proposed corrections.

The jet p_{T} response in MC simulation as a function of each of these observables is shown in Figure 5 for several regions of $p_{\text{T}}^{\text{truth}}$. The distributions are shown at various stages of the GSC to reflect the relative disagreement at the stage when each correction is derived. The dependence of the jet response on each observable is reduced to less than 2% after the full GSC is applied, with small deviations from unity reflecting the correlations between observables that are unaccounted for in the corrections. The distribution of each observable in MC simulation is shown in the bottom panels in Figure 5. The spike at zero in the f_{Tile0} distribution of Figure 5(a) at low $p_{\text{T}}^{\text{truth}}$ reflects jets that are fully contained in the electromagnetic calorimeter and do not deposit energy in the Tile calorimeter. The negative tail in the f_{LAr3} distribution of Figure 5(b) (and, to a lesser extent, in the f_{Tile0} distribution of Figure 5(a)) at low $p_{\text{T}}^{\text{truth}}$ reflects calorimeter noise fluctuations.

5.4 *In situ* calibration methods

The last stages of the jet calibration account for differences in the jet response between data and MC simulation. Such differences arise from the imperfect description of the detector response and detector material in MC simulation, as well as in the simulation of the hard scatter, underlying event, pile-up, jet formation, and electromagnetic and hadronic interactions with the detector. Differences between data and MC simulation are quantified by balancing the p_{T} of a jet against other well-measured reference objects.

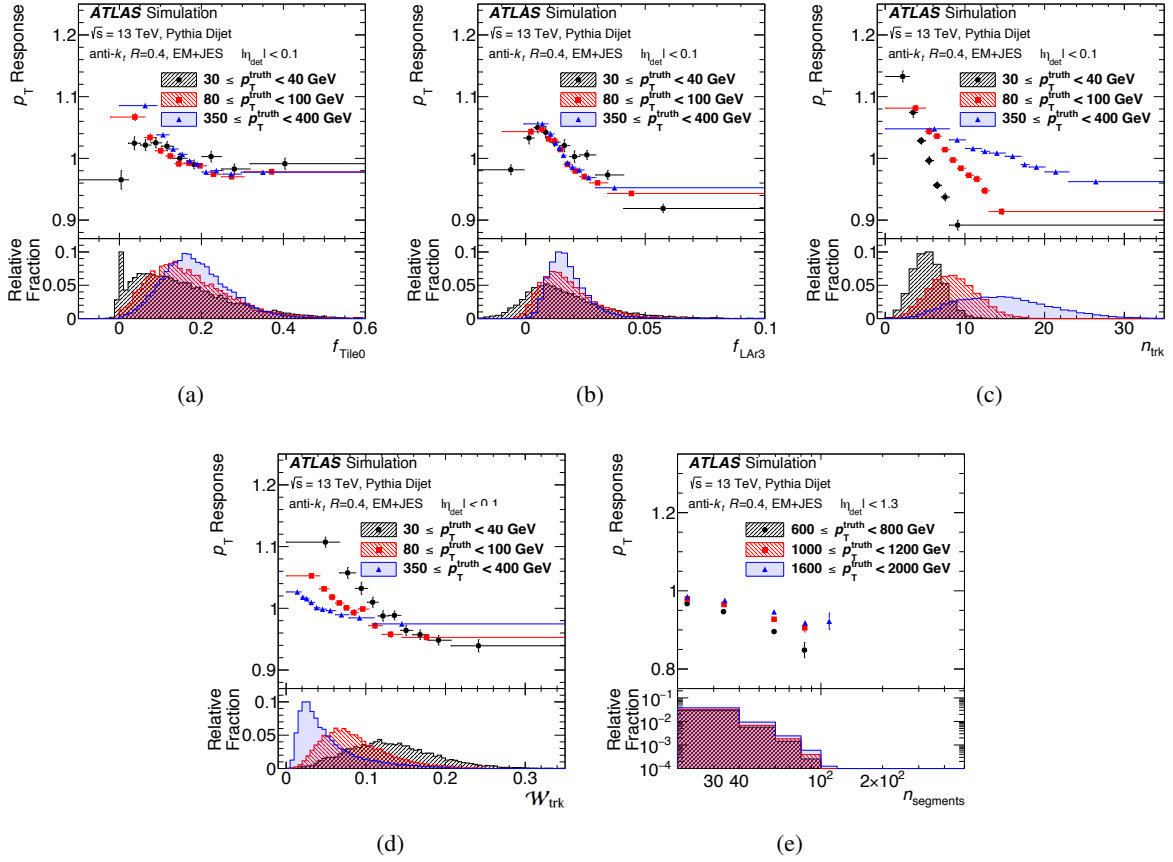


Figure 5: The average jet response in MC simulation as a function of the GSC variables for three ranges of p_T^{truth} . These include (a) the fractional energy in the first Tile calorimeter layer, (b) the fractional energy in the third LAr calorimeter layer, (c) the number of tracks per jet, (d) the p_T -weighted track width, and (e) the number of muon track segments per jet. Jets are calibrated with the EM+JES scheme and have GSC corrections applied for the preceding observables. The calorimeter distributions (a) and (b) are shown with no GSC corrections applied, the track-based distributions (d) and (c) are shown with both preceding calorimeter corrections applied, and the punch-through distribution (e) is shown with the four calorimeter and track-based corrections applied. Jets are constrained to $|\eta| < 0.1$ for the distributions of calorimeter and track-based observables and $|\eta| < 1.3$ for the muon n_{segments} distribution. The distributions of the underlying observables in MC simulation are shown in the lower panels for each p_T^{truth} region, normalized to unity. The shading in the legend reflects the shading of the distributions in the lower panel.

The η -intercalibration corrects the average response of forward jets to that of well-measured central jets using dijet events. Three other *in situ* calibrations correct for differences in the average response of central jets with respect to those of well-measured reference objects, each focusing on a different p_T region using Z boson, photon, and multijet systems. For each *in situ* calibration the response $\mathcal{R}_{in\ situ}$ is defined in data and MC simulation as the average ratio of jet p_T to reference object p_T , binned in regions of the reference object p_T . It is proportional to the response of the calorimeter to jets at the EM+JES, but is also sensitive to secondary effects such as gluon radiation and the loss of energy outside of the jet cone. Event selections are designed to reduce the impact of such secondary effects. Assuming that these secondary effects are

well modeled in the MC simulation, the ratio

$$c = \frac{\mathcal{R}_{in\ situ}^{data}}{\mathcal{R}_{in\ situ}^{MC}} \quad (1)$$

is a useful estimate of the ratio of the JES in data and MC simulation. Through numerical inversion a correction is derived to the jet four-momentum. The correction is derived as a function of jet p_T , and also as a function of jet η in the η -intercalibration.

Events used in the *in situ* calibration analyses are required to satisfy common selection criteria. At least one reconstructed primary vertex is required with at least two associated tracks of $p_T > 500$ MeV. Jets are required to satisfy data-quality criteria that discriminate against calorimeter noise bursts, cosmic rays, and other non-collision backgrounds. Spurious jets from pile-up are identified and rejected through the exploitation of track-based variables by the jet vertex tagger (JVT) [4]. Jets with $p_T < 50$ GeV and $|\eta_{det}| < 2.4$ are required to be associated with the primary vertex at the medium JVT working point, accepting 92% of hard-scatter jets and rejecting 98% of pile-up jets.

The η -intercalibration corrects the jet energy scale of forward jets ($0.8 < |\eta_{det}| < 4.5$) to that of central jets ($|\eta_{det}| < 0.8$) in a dijet system, and is discussed in Section 5.4.1. The Z/γ +jet balance analyses use a well-calibrated photon or Z boson, the latter decaying into an electron or muon pair, to measure the p_T response of the recoiling jet in the central region up to a p_T of about 950 GeV, as discussed in Section 5.4.2. Finally, the multijet balance (MJB) analysis calibrates central ($|\eta| < 1.2$), high- p_T jets ($300 < p_T < 2000$ GeV) recoiling against a collection of well-calibrated, lower- p_T jets, as discussed in Section 5.4.3. While the Z/γ +jet and MJB calibrations are derived from central jets, their corrections are applicable to forward jets whose energy scales have been equalized by the η -intercalibration procedure. The calibration constants derived in each of these analyses following Eq. (1) are statistically combined into a final *in situ* calibration covering the full kinematic region, as discussed in Section 5.4.4.

The η -intercalibration, Z/γ +jet, and MJB calibrations are derived and applied sequentially, with systematic uncertainties propagated through the chain. Systematic uncertainties reflect three effects:

1. uncertainties arising from potential mismodeling of physics effects;
2. uncertainties in the measurement of the kinematics of the reference object;
3. uncertainties in the modeling of the p_T balance due to the selected event topology.

Systematic uncertainties arising from mismodeling of certain physics effects are estimated through the use of two distinct MC event generators. The difference between the two predictions is taken as the modeling uncertainty. Uncertainties in the kinematics of reference objects are propagated from the 1σ uncertainties in their own calibration. Uncertainties related to the event topology are addressed by varying the event selections for each *in situ* calibration and comparing the effect on the p_T -response balance between data and MC simulation.

Systematic uncertainty estimates depend upon data and MC samples with event yields that fluctuate when applying the systematic uncertainty variations. To obtain results that are statistically significant, the binning of $\mathcal{R}_{in\ situ}$ in p_T and η is dynamically determined for each variation using a bootstrapping procedure [37]. In this procedure, pseudo-experiments are derived from the data or MC simulation by sampling each event with a weight taken from a Poisson distribution with a mean of one. Each pseudo-experiment

therefore emphasizes a unique subset of the data or MC simulation while maintaining statistical correlations between the nominal and varied samples. The statistical uncertainty of the response variation between the nominal and varied configuration is then taken as the RMS across the pseudo-experiments, and each varied configuration is rebinned until a target significance of a few standard deviations is achieved. Bins are combined only in regions where the observed response in p_T is nearly constant so that no significant features are removed.

5.4.1 η -intercalibration

In the η -intercalibration [3], well-measured jets in the central region of the detector ($|\eta_{\text{det}}| < 0.8$) are used to derive a residual calibration for jets in the forward region ($0.8 < |\eta_{\text{det}}| < 4.5$). The two jets are expected to be balanced in p_T at leading order in QCD, and any imbalance can be attributed to differing responses in the calorimeter regions, which are typically less understood in the forward region. Dijet topologies are selected in which the two leading jets are back-to-back in ϕ and there is no substantial contamination from a third jet. The calibration is derived from the ratio of the jet p_T responses in data and MC simulation in bins of p_T and η_{det} . Two distinct NLO MC event generators are used, POWHEG+PYTHIA and SHERPA, with the former taken as the nominal generator. The events are generated with a $2 \rightarrow 3$ leading-order matrix element, increasing the accuracy of the dijet balance for events sensitive to the rejection criteria for the third jet.

The jet p_T balance is quantified by the asymmetry

$$\mathcal{A} = \frac{p_T^{\text{probe}} - p_T^{\text{ref}}}{p_T^{\text{avg}}},$$

where p_T^{probe} is the transverse momentum of the forward jet, p_T^{ref} is the transverse momentum of the jet in a well-calibrated reference region, and p_T^{avg} is the average p_T of the two jets. The asymmetry is a useful quantity as the distribution is Gaussian in fixed bins of p_T^{avg} , whereas $p_T^{\text{probe}}/p_T^{\text{ref}}$ is not. Given that the asymmetry is Gaussian, the relative jet response with respect to the reference region may be written as

$$\left\langle \frac{p_T^{\text{probe}}}{p_T^{\text{ref}}} \right\rangle \approx \frac{2 + \langle \mathcal{A} \rangle}{2 - \langle \mathcal{A} \rangle},$$

where $\langle \mathcal{A} \rangle$ is the mean value of the asymmetry distribution for a bin of p_T^{avg} and η_{det} .

Events used in the η -intercalibration follow from a combination of single-jet triggers with various p_T thresholds in regions of either $|\eta_{\text{det}}| < 3.1$ or $|\eta_{\text{det}}| > 2.8$. Triggers are only used in regions of kinematic phase space in which they are 99% efficient. Triggers may also be prescaled, randomly rejecting a set fraction of events to satisfy bandwidth considerations, and the event weight is scaled proportionally. Events are required to have at least two jets with $p_T > 25$ GeV and with $|\eta_{\text{det}}| < 4.5$. Events that include a third jet with relatively substantial p_T , $p_T^{\text{jet3}} > 0.4 p_T^{\text{avg}}$, are rejected. The two leading jets are also required to be fairly back-to-back, such that $\Delta\phi > 2.5$ rad.

The residual calibration is derived from the ratio of the jet responses in data and the POWHEG+PYTHIA sample. The SHERPA sample is used to provide a systematic uncertainty in the MC modeling. The full range of $|\eta_{\text{det}}| < 4.5$ is used to derive calibrations for statistically significant regions of p_T^{avg} , offering an improvement on the 2011 calibration that extrapolated the measurement from a constrained region

$|\eta_{\text{det}}| < 2.7$ due to statistical considerations. A two-dimensional sliding Gaussian kernel [3] is used to reduce statistical fluctuations while preserving the shape of the MC-to-data ratio and to extrapolate the average response into regions of low statistics.

Two η -intercalibration methods are performed that provide complementary results. In the central reference method, central regions ($|\eta_{\text{det}}| < 0.8$) are used as references to measure the relative jet response in the forward probe bins ($0.8 < |\eta_{\text{det}}| < 4.5$). In the matrix method, numerous independent reference regions are chosen and the relative jet response in a given forward probe bin is measured relative to all reference regions simultaneously. The response relative to the central region is then obtained as a function of $p_{\text{T}}^{\text{avg}}$ and η_{det} through a set of linear equations. The matrix method takes advantage of a larger data set by allowing multiple reference regions, including forward ones, increasing the statistical precision of the calibration.

The binning is chosen such that each reference region is statistically significant in data and POWHEG+PYTHIA samples. Some reference regions, particularly for forward probe bins, may not be statistically significant for the SHERPA sample due to its smaller sample size. Such regions are ignored in the combined fit of the response, leading to small fluctuations in the SHERPA response, which are smoothed in p_{T} and η_{det} by the two-dimensional sliding Gaussian kernel.

The relative jet responses derived from the two methods show agreement at the level of 2%, within the uncertainty of the methods. A slightly larger response is seen in the most forward bins ($|\eta_{\text{det}}| > 2.5$) in the matrix method, as seen in 2011. This difference exists in the response in both data and MC simulation, and the MC-to-data ratio is consistent between methods. The matrix method is used to derive the nominal calibration in the following results, with the central reference method providing validation. As in the 2011 calibration, γ +jet events are also used to validate the response in the forward regions, and show good agreement between data and MC simulation in the forward region.

The relative jet response is shown in Figure 6 for both data and the two MC samples, parameterized by p_{T} in two η_{det} ranges and by η_{det} in two p_{T} ranges. The level of modeling agreement, taken between POWHEG+PYTHIA and SHERPA, is significantly better than in previous results and is generally within 1%, with larger differences at low p_{T} and in forward η_{det} regions. This improved agreement is not due to any changes to the method but results from better overall particle-level agreement, particularly the improved modeling of the third-jet radiation by the NLO POWHEG+PYTHIA and SHERPA generators over that of the LO PYTHIA and HERWIG generators used in the 2011 calibration. The particle-level response was also measured with a POWHEG-Box sample showered with Herwig++, and shows a similar level of agreement as found between POWHEG+PYTHIA and SHERPA. Uncertainties are calculated in a given bin by shifting the observed asymmetry with all reference regions and recalculating the response. While accurate for data and POWHEG+PYTHIA, this can lead to statistical uncertainties that do not cover the observed fluctuations in SHERPA, but that do not affect the final systematic uncertainty derived from the smoothed difference between MC samples.

The response in data is consistently larger than that in both MC samples and in the 2011 data for the forward detector region for all p_{T} ranges. This is due to the reduction in the number of samples used to reconstruct pulses in the LAr calorimeter from five to four, which is sensitive to differences in the pulse shape between data and MC simulation. The reduction was predicted to increase the response in the forward region, as seen in a comparison of Run 1 data processed using both five and four samples. The expected increase matches that seen in 2015 data, and is corrected for by the η -intercalibration procedure.

The effect was predicted to be particularly large for $2.3 < |\eta_{\text{det}}| < 2.6$ due to details of the jet reconstruction in calorimeter transition regions. To fully account for this effect, a finer binning of $\Delta\eta_{\text{det}}$ is used in this region.

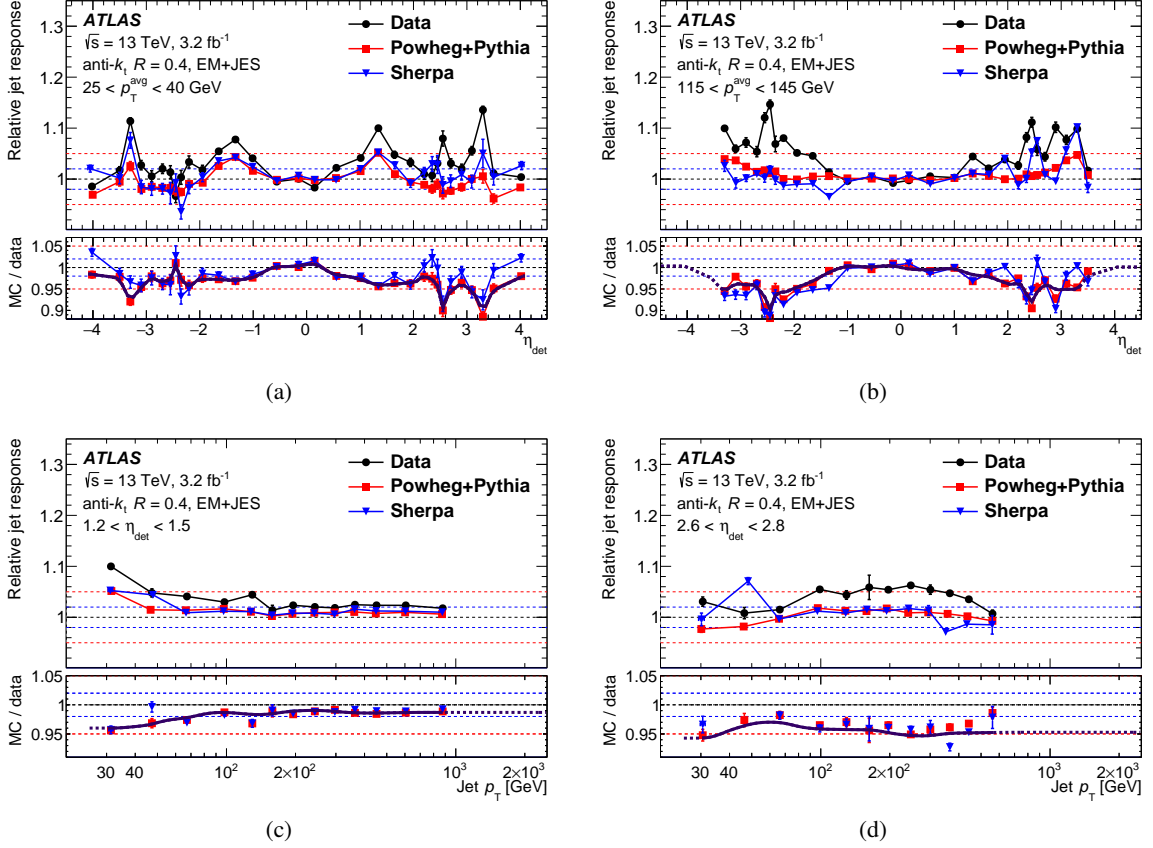


Figure 6: Relative response of EM+JES jets as a function of η at (a) low p_T and (b) high p_T , and as a function of jet p_T within the ranges of (c) $1.2 < \eta_{\text{det}} < 1.5$ and (d) $2.6 < \eta_{\text{det}} < 2.8$. The bottom panels show the MC-to-data ratios, and the overlaid curve reflects the smoothed *in situ* correction, appearing solid in the regions in which it is derived and dotted in the regions to which it is extrapolated by the two-dimensional sliding Gaussian kernel. Results are obtained with the matrix method. The binning is optimized for data and POWHEG+PYTHIA, and fluctuations in the response in SHERPA are not statistically significant. Horizontal dotted lines are drawn in all at 1 ± 0.02 , and 1 ± 0.05 to guide the eye.

The systematic uncertainties account for physics and detector mismodelings as well as the effect of the event topology on the modeling of the p_T balance. They are derived as a function of p_T and $|\eta_{\text{det}}|$, with no statistically significant variations observed between positive and negative η_{det} . The dominant uncertainty due to MC mismodeling is taken as the difference in the smoothed jet response between POWHEG+PYTHIA and SHERPA. The estimation of systematic uncertainties due to pile-up and the choice of event topology are similar to those of the 2011 calibration [3], but now use the bootstrapping procedure to ensure statistical significance. These uncertainties, including those from varying the $\Delta\phi$ separation requirement between the two leading jets and the third-jet veto requirement, are usually small compared to the MC uncertainty and are therefore summed in quadrature with it into a single physics mismodeling uncertainty, with a negligible loss of correlation information. Two additional and separate uncertainties

are derived to account for statistical fluctuations and the observed non-closure of the calibration for $2.0 < |\eta_{\text{det}}| < 2.6$, primarily due to the LAr pulse reconstruction effects described above. The latter is taken as the difference between data and the nominal MC event generator after repeating the analysis with the derived calibration applied to data. The total η -intercalibration uncertainty is shown in Figure 7 as a function of η_{det} for two jet p_{T} values.

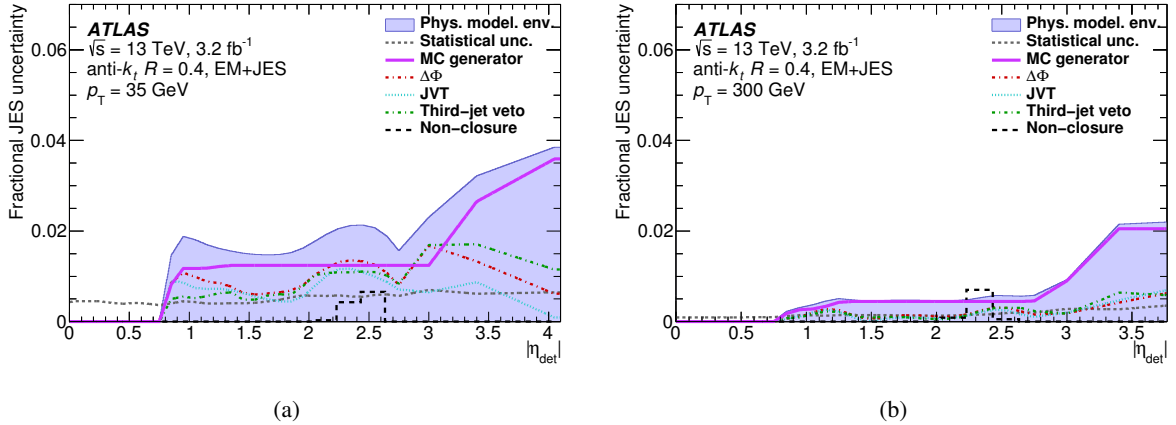


Figure 7: Systematic uncertainties of EM+JES jets as a function of $|\eta_{\text{det}}|$ at (a) $p_{\text{T}} = 35$ GeV and at (b) $p_{\text{T}} = 300$ GeV in the η -intercalibration. The physics mismodeling envelope includes the uncertainty derived from the alternative MC event generator as well as the uncertainties of the JVT, $\Delta\phi$, and third-jet veto event selections. Also shown are the statistical uncertainties of the MC-to-data response ratio and the localized non-closure uncertainty for $2.0 < |\eta_{\text{det}}| < 2.6$. Small fluctuations in the uncertainties are statistically significant and are smoothed in the combination, described in Section 5.4.4.

5.4.2 Z+jet and γ +jet balance

An *in situ* calibration of jets up to 950 GeV and with $|\eta| < 0.8$ is derived through the p_{T} balance of a jet against a Z boson or a photon. Z/ γ +jet calibrations rely on the independent measurement and calibration of the energy of a photon or of the lepton decay products of a Z boson, through the decay channels of $Z \rightarrow e^+e^-$ and $Z \rightarrow \mu^+\mu^-$. Bosons are ideal candidates for reference objects as they are precisely measured: muons from tracks in the ID and MS and photons and electrons through their relatively narrow showers in the electromagnetic calorimeter and the independent measurement of electron tracks in the ID. The Z+jet calibration is limited to the statistically significant p_{T} range of Z boson production of $20 < p_{\text{T}} < 500$ GeV. The γ +jet calibration is limited by the small number of events at high p_{T} and by both dijet contamination and an artificial reduction of the number of events due to the prescaled triggers at low p_{T} , limiting the calibration to $36 < p_{\text{T}} < 950$ GeV.

Two techniques are used to derive the response with respect to the Z boson and photon [3]. The Direct Balance (DB) technique measures the ratio of a fully reconstructed jet's p_{T} , calibrated up to the η -intercalibration stage, and a reference object's p_{T} . The use of a fully reconstructed and calibrated jet allows the calibration to be applied to jets in a straightforward manner. For a $2 \rightarrow 2$ Z/ γ +jet event, the p_{T} of the jet can be expected to balance that of the reference object. However, the DB technique can be affected by additional parton radiation contributing to the recoil of the boson, appearing as subleading jets.

This is mitigated through a selection against events with a second jet of significant p_T and a minimum requirement on $\Delta\phi$, the azimuthal angle between the Z/γ boson and the jet, to ensure they are sufficiently back-to-back in ϕ . The component of the boson p_T perpendicular to the jet axis is also ignored, with the reference p_T defined as

$$p_T^{\text{ref}} = p_T^{Z/\gamma} \times \cos(\Delta\phi).$$

The DB technique is also affected by out-of-cone radiation, consisting of the energy lost outside of the reconstructed jet's cone of $R = 0.4$ due to fragmentation processes. The out-of-cone radiation may lead to a p_T imbalance between a jet and the reference boson, and is estimated by measuring the profile of tracks around the jet axis [3].

The Missing- E_T Projection Fraction (MPF) technique instead derives a p_T balance between the full hadronic recoil in an event and the reference boson. The average MPF response is defined as

$$\mathcal{R}_{\text{MPF}} = \left\langle 1 + \frac{\hat{n}_{\text{ref}} \cdot \vec{E}_T^{\text{miss}}}{p_T^{\text{ref}}} \right\rangle, \quad (2)$$

where \mathcal{R}_{MPF} is the calorimeter response to the hadronic recoil, \hat{n}_{ref} is the direction of the reference object, and p_T^{ref} is the transverse momentum of the reference object. The \vec{E}_T^{miss} in Eq. (2) is calculated directly from all the topo-clusters of calorimeter cells, calibrated at the EM scale, and is corrected with the p_T of the minimum ionizing muons in $Z \rightarrow \mu\mu$ events. No correction is needed for electrons or photons as their calorimeter response is nearly unity.

The MPF technique utilizes the full hadronic recoil of an event rather than a single reconstructed jet. The MPF response is therefore less sensitive to the jet definition, radius parameter, and out-of-cone radiation than the DB response, with reconstructed jets only explicitly used in the event selections. The MPF technique is less sensitive to the generally ϕ -symmetric pile-up and underlying-event activity. As the MPF technique is not derived from a reconstructed jet the correction does not directly reflect the energy within the reconstructed jet's cone. The out-of-cone uncertainty derived for the DB technique is therefore applied as an estimate of the effect of showering and jet topology. As the MPF technique does not use jets directly, the impact of the GSC is accounted for by applying a correction to the cluster-based \vec{E}_T^{miss} , equal to the difference in momentum of the leading jet with and without the GSC. The results from this method are compared with those using no GSC and those with the GSC applied to all jets in the event, with negligible differences seen in the MC-to-data response ratio.

The response of the jet (DB) or hadronic recoil (MPF) is measured in both data and MC simulation, and a residual correction is derived using the MC-to-data ratio. The two methods are complementary and they are both pursued to check the compatibility of the measured response. The results below present the Z +jet results using the MPF technique and the γ +jet results using the DB technique.

For both techniques the average response is initially derived in bins of p_T^{ref} . In each bin of p_T^{ref} , a maximum-likelihood fit is performed using a modified Poisson distribution extended to non-integer values. The fit range is limited to twice the RMS of the response distribution around the mean to minimize the effect of MC mismodeling in the tails of the distribution. The average response is taken as the mean of the best-fit Poisson distribution. For 2015 data, a new procedure is used to reparameterize the average balance from the reference object p_T to the corresponding jet p_T , better representing the mismeasured jet to which the calibration is applied. This procedure is used after the calibration is derived by finding the average jet p_T , without Z/γ +jet calibrations applied, within each bin of reference p_T .

Events in the Z +jet selection are required to have a leading jet with $p_T > 10$ GeV, and in the γ +jet selection are required to have a leading jet with $p_T > 20$ GeV. In the γ +jet DB (Z +jet MPF) technique, the leading jet must sufficiently balance the reference boson in the azimuthal plane, requiring $\Delta\phi(\text{jet}, Z(\gamma)) > 2.8$ (2.9) rad. To reduce contamination from events with significant hadronic radiation, a selection of $p_T^{\text{second}} < \max(15 \text{ GeV}, 0.1 \times p_T^{\text{ref}})$ is placed on the second jet, ordered by p_T , in the γ +jet DB technique. For the Z +jet MPF technique, this selection is mostly looser as \mathcal{R}_{MPF} is less sensitive to QCD radiation, requiring the second jet to have $p_T^{\text{second}} < \max(12 \text{ GeV}, 0.3 \times p_T^{\text{ref}})$.

Electrons [38] (muons [16]) used in the Z +jet events are required to pass basic quality and isolation cuts, and to fall within the range $|\eta| < 2.47$ (2.4). Events are selected based on the lowest- p_T unscaled single-electron or single-muon trigger. Electrons that fall in the transition region between the barrel and the endcap of the electromagnetic calorimeter ($1.37 < |\eta| < 1.52$) are rejected. Both leptons are required to have $p_T > 20$ GeV, and the invariant mass of the opposite-charge pairs must be consistent with the Z boson mass, with $66 < m_{\ell\ell} < 116$ GeV. Photons [38] used in the γ +jet events must satisfy tight selection criteria and be within the range $|\eta| < 1.37$ with $p_T > 25$ GeV. Events are selected based on a combination of fully efficient single-photon triggers. Energy isolation criteria are applied to the photon showers to discriminate photons from π^0 decays and to maximize the suppression of jets misidentified as photons [39]. Jets within $\Delta R = 0.35$ of a lepton are removed from consideration in the Z +jet selection, while jets within $\Delta R = 0.2$ of photons are similarly removed from consideration in both the Z +jet and γ +jet selections.

The average response in Z/γ +jet events as a function of jet p_T is shown in Figure 8 for data and two MC samples. For the DB technique in γ +jet events, the response is slightly below unity, reflecting the fraction of p_T falling outside of the reconstructed jet cone. For the MPF technique in Z +jet events, \mathcal{R}_{MPF} is significantly below unity, reflecting that the Z boson is fully calibrated while the topo-clusters used in calculating the hadronic recoil are at the EM scale. However, in both cases the data and MC simulation are in agreement, with the MC-to-data ratio within $\sim 5\%$ of unity for both MC samples. The rise in \mathcal{R}_{MPF} at low p_T in Figure 8(a) is caused by the jet reconstruction threshold.

Systematic uncertainties in the MC-to-data response ratios are shown in Figure 9. In both the DB and MPF techniques the event selections are varied to estimate the impact of the choice of event topology on the MC mismodeling of the p_T response. Variations are made to the selection criteria for the second-jet p_T and $\Delta\phi$ between the leading jet and reference object to assess the effect of additional parton radiation. The effect of pile-up suppression is similarly studied by varying the JVT cut about its nominal value. Potential MC event generator mismodeling is explored by repeating the analyses with alternative MC event generators, with the difference in the MC-to-data response ratios taken as a systematic uncertainty. Uncertainties in the energy (momentum) scale and resolution of electrons and photons (muons) are estimated from studies of $Z \rightarrow ee$ ($Z \rightarrow \mu\mu$) measurements in data [16, 38]. Variations of $\pm 1\sigma$ are propagated through the analyses to the MC-to-data response ratios. A purity uncertainty in the γ +jet balance accounts for the contamination from multijet events arising from jets appearing as fake photons. The effect of this contamination on the MC-to-data response ratio is studied by relaxing the photon identification criteria. The uncertainty due to out-of-cone radiation is derived from differences between data and MC simulation in the transverse momentum of charged-particle tracks around the jet axis. The bootstrapping procedure is used to ensure only statistically significant variations of the response are included in the uncertainties.

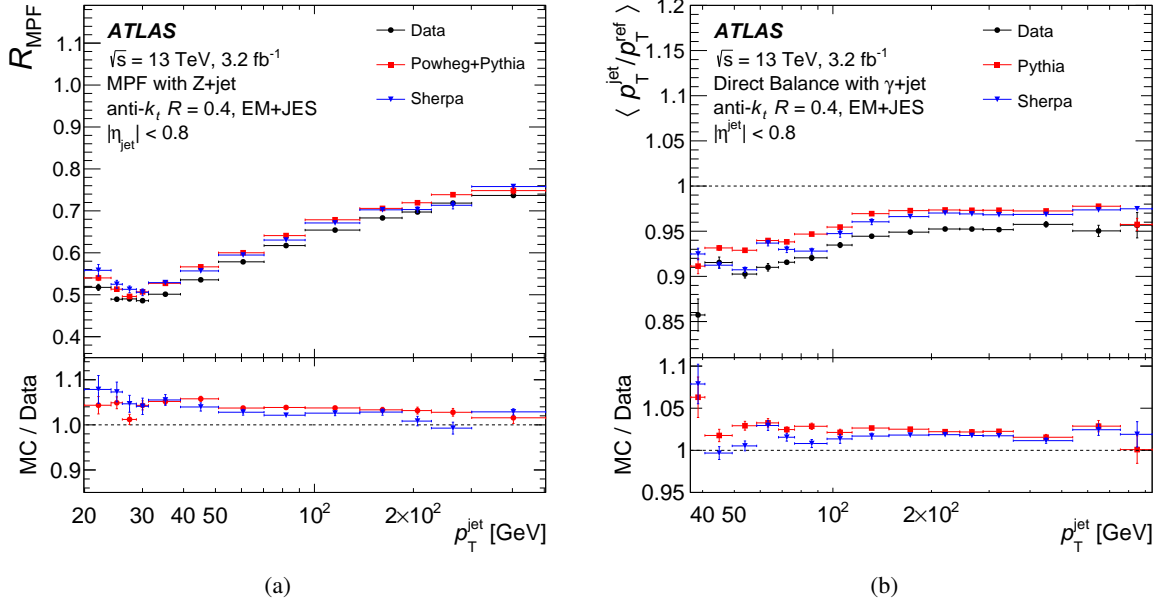


Figure 8: The average (a) MPF response in Z+jet events and (b) Direct Balance jet p_T response in γ +jet events as a function of jet p_T for EM+JES jets calibrated up to the η -intercalibration. The response is given for data and two distinct MC samples, and the MC-to-data ratio plots in the bottom panels reflect the derived *in situ* corrections. A dotted line is drawn at unity in the top-right panel and bottom panels to guide the eye.

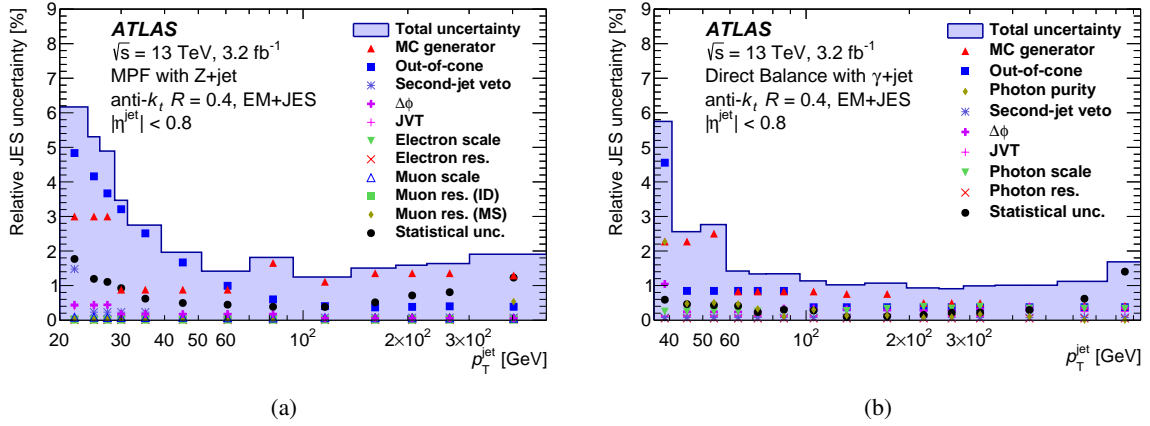


Figure 9: Systematic uncertainties of EM+JES jets, calibrated up to the η -intercalibration, as a function of jet p_T for (a) Z+jet events using the MPF technique and (b) γ +jet events using the Direct Balance technique. Uncertainties account for out-of-cone radiation and variations of the JVT, $\Delta\phi$, second-jet veto, and photon purity event selections. Uncertainties are also propagated from the electron and photon energy scale and resolution and the muon momentum scale and resolution in the ID and MS. Also shown are the statistical uncertainties of the MC-to-data response ratio and the uncertainty derived from an alternative MC event generator. Small fluctuations in the uncertainties are statistically significant and are smoothed in the combination, described in Section 5.4.4.

5.4.3 Multijet balance

The multijet balance (MJB) [3] is the last stage of the *in situ* calibration and is used to extend the calibrations to a p_T of 2 TeV. Topologies with three or more jets are used to balance a high- p_T jet against a recoil system composed of several lower- p_T jets. The recoil jets are of sufficiently low p_T as to be in the range of Z/γ +jet calibrations and are therefore fully calibrated. The Z/γ +jet input calibrations are combined using the procedure outlined in Section 5.4.4.

The leading jet is taken as the highest- p_T jet of an event and the four-momenta of all other subleading jets are combined into a recoil-system four-momentum. The leading jet is calibrated only up to the η -intercalibration stage, and is therefore at the same scale as the jets explored by the Z/γ +jet methods. A p_T limit of 950 GeV is imposed on each subleading jet to ensure they are fully calibrated by the Z/γ +jet methods. A consequence of this limit is the rejection of events with very high- p_T leading jets, which often have subleading jets with p_T above this limit. These events are recovered through the use of multiple iterations of the MJB method, with the previously derived MJB calibration being applied to higher- p_T subleading jets. The new p_T limit on the subleading jets is determined by the statistical reach of the previous iteration of the MJB method. Using 2015 data, the MJB method is able to cover a range of $300 < p_T < 2000$ GeV using two iterations.

The average response between the leading jet and recoil system, \mathcal{R}_{MJB} , is defined as

$$\mathcal{R}_{\text{MJB}} = \left\langle \frac{p_T^{\text{leading}}}{p_T^{\text{recoil}}} \right\rangle,$$

where p_T^{leading} is the transverse momentum of the highest- p_T jet and p_T^{recoil} is from the vectorial sum of all subleading jets. The response is initially binned as a function of p_T^{recoil} , corresponding to the well-calibrated reference object. As with the Z/γ +jet calibrations, a new procedure is used for 2015 data to reparameterize the response from p_T^{recoil} to p_T^{leading} . This procedure is applied after the calibration is derived by finding the average p_T^{leading} , without Z/γ +jet or MJB calibrations applied, within each bin of p_T^{recoil} .

Events entering the MJB calibration are recorded using a combination of fully efficient single-jet triggers used in distinct regions of p_T^{recoil} . Events are required to have at least three jets with $p_T > 25$ GeV and $|\eta_{\text{det}}| < 2.8$, with the leading jet required to be central ($|\eta_{\text{det}}| < 1.2$). Events dominated by a dijet p_T balance are rejected if the second jet's p_T is a considerable fraction of the recoil system's p_T , with a p_T asymmetry requirement of $p_T^{\text{asymmetry}} = p_T^{\text{second}}/p_T^{\text{recoil}} < 0.8$. The azimuthal angle between the leading jet and the recoil system, α^{MJB} , must satisfy the requirement $|\alpha^{\text{MJB}} - \pi| < 0.3$ rad, ensuring the p_T of the recoil system is balanced against that of the leading jet. Contamination of the leading jet from other jets is minimized by requiring the absolute value of the azimuthal angle, β^{MJB} , between the leading jet and the nearest jet with $p_T > 0.25 p_T^{\text{leading}}$ to be greater than 1 rad.

The response \mathcal{R}_{MJB} is shown for data and MC simulation in Figure 10(a). As expected, an offset is seen between data and MC simulation, reflecting that the recoil system in data is fully calibrated to the *in situ* stage while the leading jet is only partially calibrated. The response is below unity, particularly at low p_T , reflecting the bias in \mathcal{R}_{MJB} due to the leading-jet isolation requirement, which is well modeled in MC simulation. The MC-to-data ratio of \mathcal{R}_{MJB} , given by Eq. (1), is seen in the bottom panel of Figure 10(a). A fairly constant correction of 2% is derived, up from 1% in 2011. This increase is partially due to changes

in the simulation of hadronic showers in Geant4 as well as the response drift in the Tile calorimeter PMTs, which will be directly corrected in future data reprocessing.

Systematic uncertainties in the MC-to-data response ratio as a function of p_T^{leading} are shown in Figure 10(b). They reflect 1σ uncertainties derived from the MJB event selection, MC modeling, and jet calibration. Event selection uncertainties are derived by varying the event selections and examining the impact on the MC-to-data ratio. The 1σ variations were conservatively found in 2011 to be ± 0.1 rad for α^{MJB} , ± 0.5 rad for β^{MJB} , ± 5 GeV for $p_T^{\text{threshold}}$, and ± 0.1 for $p_T^{\text{asymmetry}}$. The uncertainty due to MC modeling is taken as the difference in the MJB correction between the nominal PYTHIA generator and Herwig++. Uncertainties in the calibration of subleading jets are taken from the input *in situ* calibrations, with each component individually varied by $\pm 1\sigma$ and propagated through each MJB iteration. The JES uncertainties related to the pile-up, punch-through, flavor composition, and flavor response are also propagated through each iteration in the 2015 calibration. The bootstrapping procedure is used to ensure statistical significance for each systematic uncertainty, with each pseudo-experiment independently propagated through the iterations. The combined uncertainty is generally below 1.5%, consistent with that from the 2011 calibration.

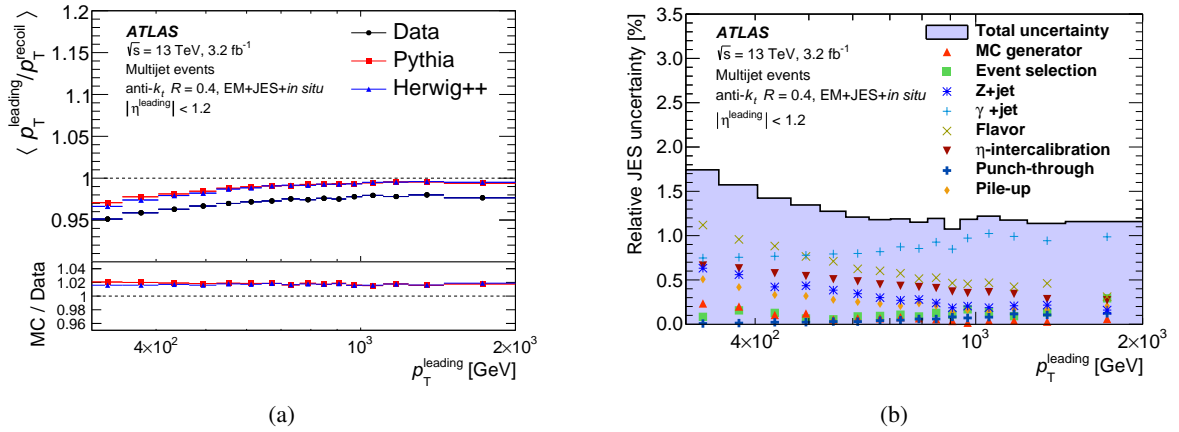


Figure 10: (a) Average p_T response of the leading EM+JES jet, calibrated up to the η -intercalibration, in multijet events as a function of p_T^{leading} . The Z/ γ +jet calibrations are applied only to subleading jets in the recoil system. The response is given for data and two distinct MC event generators, and the MC-to-data response ratio in the bottom panel reflects the derived *in situ* correction. (b) Systematic uncertainties in the ratio account for variations of the event selection, MC mismodeling, and propagated uncertainties from the Z+jet, γ +jet, η -intercalibration, flavor, punch-through, and pile-up studies. Small fluctuations in the uncertainties are statistically significant and are smoothed during the combination, described in Section 5.4.4.

5.4.4 *In situ* combination

The data-to-MC ratio and the associated systematic uncertainties derived from the orthogonal Z+jet, γ +jet, and MJB calibrations are combined across overlapping regions of jet p_T [3]. For each method, the results are recast into a common, fine binning in p_T by interpolating second-order polynomial splines. Each *in situ* method is assigned a p_T -dependent weight through a χ^2 minimization, using as inputs the response ratios and their uncertainties in each p_T bin. A method's weight is therefore increased in p_T

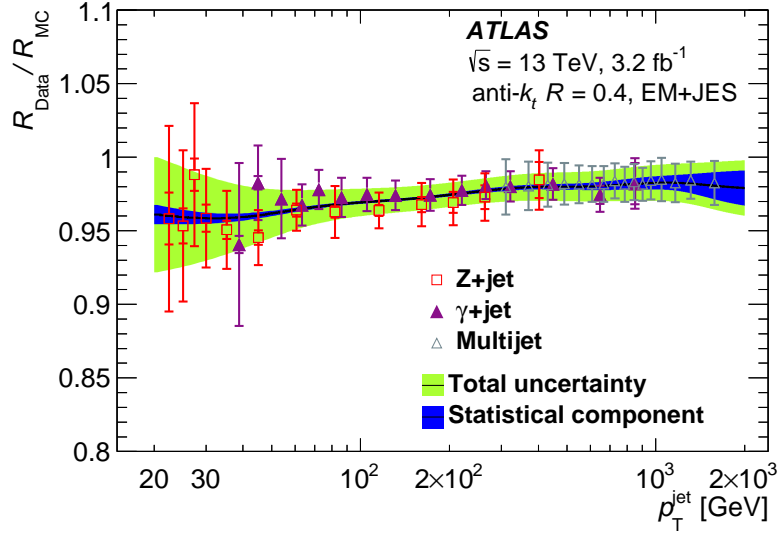


Figure 11: Ratio of the EM+JES jet response in data to that in the nominal MC event generator as a function of jet p_T for Z+jet, γ +jet, and multijet *in situ* calibrations. The final derived correction (black line) and its statistical (dark blue) and total (light green) uncertainty bands are also shown.

regions of smaller relative uncertainty and smaller bin size, with the combination favoring the method of greatest precision in each region. The combined data-to-MC ratio is smoothed with a sliding Gaussian kernel to reduce statistical fluctuations.

The combined data-to-MC ratio is shown in Figure 11 alongside the Z+jet, γ +jet, and MJB ratios in their original binnings. The inverse of the combined data-to-MC ratio is taken as the *in situ* correction applied to data. The combined correction is 4% at low p_T and decreases to 2% at 2 TeV. This is a larger correction than seen in 2011, but it is expected due to changes in the simulation of hadronic showers in Geant4 and the slight PMT down-drift in the Tile calorimeter. The individual *in situ* results show good agreement with one another in the various regions of overlapping p_T . The differences between *in situ* measurements are quantified with $\sqrt{\chi^2/N_{\text{dof}}}$, which is generally below 1.

The systematic uncertainties are averaged and smoothed with the same combination procedure through a linear transformation [3, 13]. One at a time, each uncertainty source of each *in situ* method is shifted coherently by 1σ , within the method's original binning. The binning interpolation and combination are then repeated with the nominal weighting of the methods. In this procedure, the various systematic uncertainties are treated independently of one another and as fully correlated across p_T . Their independent treatment during the combination allows for alternative correlation assumptions at a later stage, and the difference between treating correlations before and after the combination are found to be negligible. The difference between the shifted combined correction factor and the nominal is taken as the 1σ variation for each uncertainty source. The Z/ γ +jet uncertainties have a one-to-one correlation with the corresponding uncertainties propagated through the MJB technique. Therefore, for each of these uncertainties, the correction factors of the *in situ* methods are shifted coherently by 1σ , before the binning interpolation and combination steps.

If the nominal corrections from different *in situ* methods disagree in a p_T bin, such that the tension factor $\sqrt{\chi^2/N_{\text{dof}}}$ is above 1, the uncertainty from each source is scaled by the tension factor in that bin. In the 2015 calibration, a tension factor of ~ 1.1 was found only in the narrow p_T region between 45 and 50 GeV.

As with the nominal result, each systematic uncertainty component is smoothed using a sliding Gaussian kernel.

6 Systematic uncertainties

The final calibration includes a set of 80 JES systematic uncertainty terms propagated from the individual calibrations and studies, listed in Table 1. The majority (67) of uncertainties come from the Z/γ -jet and MJB *in situ* calibrations and account for assumptions made in the event topology, MC simulation, sample statistics, and propagated uncertainties of the electron, muon, and photon energy scales. The remaining 13 uncertainties are derived from other sources. Four pile-up uncertainties are included to account for potential MC mismodeling of N_{PV} , μ , ρ , and the residual p_T dependence. Three η -intercalibration uncertainties account for potential physics mismodeling, statistical uncertainties, and the method non-closure in the $2.0 < |\eta_{\text{det}}| < 2.6$ region. Three additional uncertainties account for differences in the jet response and simulated jet composition of light-quark, b -quark, and gluon-initiated jets. As in the 2011 calibration, the flavor response uncertainties are derived by comparing the average jet response for each jet flavor using PYTHIA and Herwig++. The flavor composition uncertainty is analysis dependent, and is either derived from MC samples in the relevant phase-space, or is assumed to be a 50% quark and 50% gluon composition with a conservative 100% uncertainty. An uncertainty in the GSC punch-through correction is also considered, derived as the maximum difference between the jet responses in data and MC simulation as a function of the number of muon segments. One AFII modeling uncertainty accounts for non-closure in the absolute JES calibration of fast-simulation jets, and is applied only to AFII MC samples. A high- p_T jet uncertainty is derived from single-particle response studies [34] and is applied to jets with $p_T > 2$ TeV, beyond the reach of the *in situ* methods.

The full combination of all uncertainties is shown in Figure 12 as a function of p_T at $\eta = 0$ and as a function of η at $p_T = 80$ GeV, assuming a flavor composition taken from the inclusive dijet selection in PYTHIA. Each uncertainty is generally treated independently of the others but fully correlated across p_T and η . Exceptions are the electron and photon energy scale measurements, which are treated as fully correlated. The uncertainty is largest at low p_T , starting at 4.5% and decreasing to 1% at 200 GeV. It rises after 200 GeV due to the statistical uncertainties related to the *in situ* calibrations, and increases sharply after 2 TeV where MJB measurements end and larger uncertainties are taken from the single-particle response. The uncertainty is fairly constant as a function of η and reaches a maximum of 2.5% for the most forward jets. A sharp feature can be seen in the region $2.0 < |\eta| < 2.6$ due to the non-closure uncertainty of the η -intercalibration.

The complete set of systematic uncertainties provides a detailed understanding of the many factors that influence the JES. Uncertainties are generally derived in specific regions of jet p_T and η , and the correlation of uncertainties between two jets with different kinematics can vary in strength. For the set of variables $\{p_T, \eta\}$, the Pearson correlation coefficient (C) between two jets is used to quantify the correlations, and is defined as

$$C(\{p_T, \eta\}_1, \{p_T, \eta\}_2) = \frac{\text{Cov}(\{p_T, \eta\}_1, \{p_T, \eta\}_2)}{\sqrt{\text{Cov}(\{p_T, \eta\}_1, \{p_T, \eta\}_1) \times \text{Cov}(\{p_T, \eta\}_2, \{p_T, \eta\}_2)}}, \quad (3)$$

where Cov is the covariance of the systematic uncertainties between the two sets of variables.

Name	Description
Z+jet	
Electron scale	Uncertainty in the electron energy scale
Electron resolution	Uncertainty in the electron energy resolution
Muon scale	Uncertainty in the muon momentum scale
Muon resolution (ID)	Uncertainty in muon momentum resolution in the ID
Muon resolution (MS)	Uncertainty in muon momentum resolution in the MS
MC generator	Difference between MC event generators
JVT	Jet vertex tagger uncertainty
$\Delta\phi$	Variation of $\Delta\phi$ between the jet and Z boson
2nd jet veto	Radiation suppression through second-jet veto
Out-of-cone	Contribution of particles outside the jet cone
Statistical	Statistical uncertainty over 13 regions of jet p_T
γ+jet	
Photon scale	Uncertainty in the photon energy scale
Photon resolution	Uncertainty in the photon energy resolution
MC generator	Difference between MC event generators
JVT	Jet vertex tagger uncertainty
$\Delta\phi$	Variation of $\Delta\phi$ between the jet and γ
2nd jet veto	Radiation suppression through second-jet veto
Out-of-cone	Contribution of particles outside the jet cone
Photon purity	Purity of sample in γ +jet balance
Statistical	Statistical uncertainty over 15 regions of jet p_T
Multijet balance	
α^{MJB} selection	Angle between leading jet and recoil system
β^{MJB} selection	Angle between leading jet and closest subleading jet
MC generator	Difference between MC event generators
$p_T^{\text{asymmetry}}$ selection	Second jet's p_T contribution to the recoil system
Jet p_T threshold	Jet p_T threshold
Statistical components	Statistical uncertainty over 16 regions of p_T^{leading}
η-intercalibration	
Physics mismodeling	Envelope of the MC, pile-up, and event topology variations
Non-closure	Non-closure of the method in the $2.0 < \eta_{\text{det}} < 2.6$ region
Statistical component	Statistical uncertainty
Pile-up	
μ offset	Uncertainty of the μ modeling in MC simulation
N_{PV} offset	Uncertainty of the N_{PV} modeling in MC simulation
ρ topology	Uncertainty of the per-event p_T density modeling in MC simulation
p_T dependence	Uncertainty in the residual p_T dependence
Jet flavor	
Flavor composition	Uncertainty in the jet composition between quarks and gluons
Flavor response	Uncertainty in the jet response of gluon-initiated jets
b -jet	Uncertainty in the jet response of b -quark-initiated jets
Punch-through	Uncertainty in GSC punch-through correction
AFII non-closure	Difference in the absolute JES calibration using AFII
Single-particle response	High- p_T jet uncertainty from single-particle and test-beam measurements

Table 1: Summary of the systematic uncertainties in the JES, including those propagated from electron, photon, and muon energy scale calibrations [16, 38].

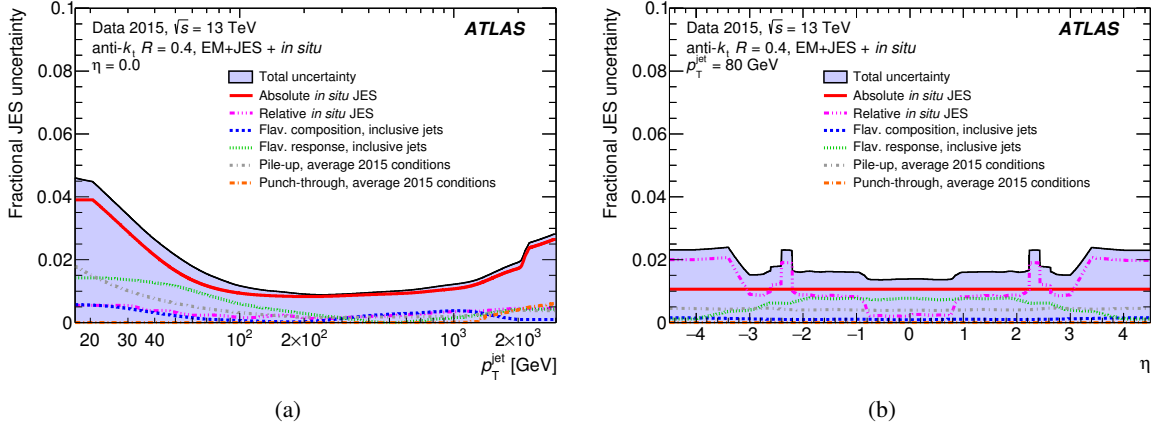


Figure 12: Combined uncertainty in the JES of fully calibrated jets as a function of (a) jet p_T at $\eta = 0$ and (b) η at $p_T = 80$ GeV. Systematic uncertainty components include pile-up, punch-through, and uncertainties propagated from the Z/γ +jet and MJB (absolute *in situ* JES) and η -intercalibration (relative *in situ* JES). The flavor composition and response uncertainties assume a quark and gluon composition taken from PYTHIA dijet MC simulation (inclusive jets).

The jet–jet correlation matrix, including all 80 uncertainties, is shown as a function of jet p_T ($\eta^{\text{jet}1} = \eta^{\text{jet}2} = 0$) in Figure 13(a) and as a function of jet η ($p_T^{\text{jet}1} = p_T^{\text{jet}2} = 60$ GeV) in Figure 13(b). Regions of strong correlation ($C \sim 1$) are shown in mid-tone red, and of weak correlation ($C \sim 0$) in dark blue. In the p_T correlation map, features are visible at low, medium, high, and very high p_T , corresponding to the kinematic phase space of the *in situ* p_T -balance calibrations and the single-particle response. In the η correlation map the correlation is strongest in the central and forward η regions of the η -intercalibration. Strong jet–jet correlations are seen as a function of η due to the dominance of the MC modeling term in the η -intercalibration. Correlations due to the non-closure uncertainty, being most significant for $2.2 < |\eta| < 2.4$, are seen to be localized in a narrow η region, as expected.

While the 80 uncertainties provide the most accurate understanding of the JES uncertainty, a number of physics analyses would be hampered by the implementation and evaluation of them all. Furthermore, many would receive no discernible benefit from the rigorous conservation of all correlations. For these cases a reduced set of nuisance parameters (NPs) is made available that seeks to preserve as precisely as possible the correlations across jet p_T and η .

As a first step, the global reduction [3] is performed through an eigen-decomposition of the 67 p_T -dependent *in situ* uncertainties following from the Z/γ +jet and MJB calibrations. The five principal components of greatest magnitude are kept separate and the remaining components are quadratically combined into a single NP, treating them as independent of one another. This reduces the number of independent *in situ* uncertainty sources from 67 to 6 NPs, with only percent-level losses to the correlations between jets. The difference in correlation, given by Eq. (3), between the full NP representation and the reduced representation as a function of jet p_T is given in Figure 14(a), showing the losses to be small and constrained in kinematic phase space.

A new procedure is introduced for 2015 data to further reduce the remaining 19 NPs (6 *in situ* p_T -balance NPs and 13 others) into a smaller, strongly reduced representation. Various combinations of the remaining NPs into three components are attempted, and NPs within a single component are quadratically combined.

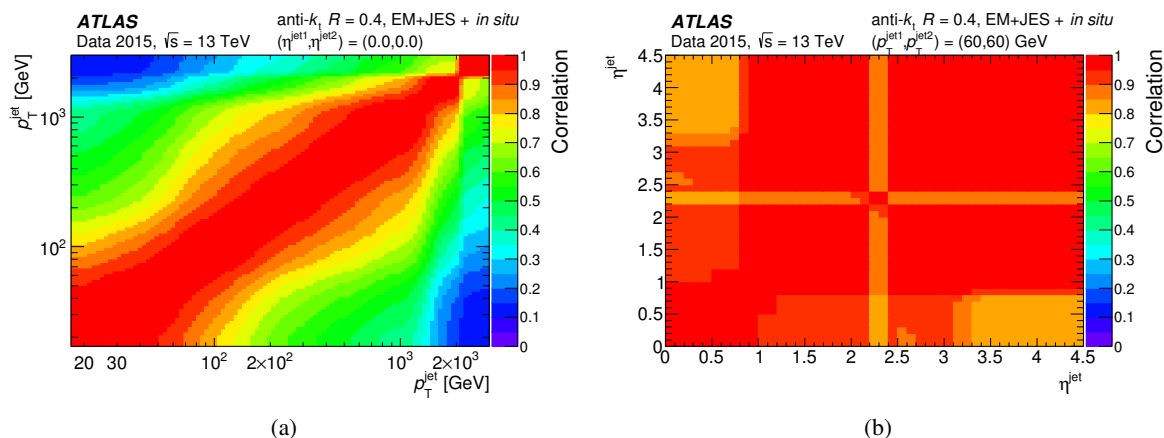


Figure 13: The full correlation matrix between two jets using all 80 uncertainty sources as a function of (a) p_T^{jet} for $\eta^{\text{jet}1} = \eta^{\text{jet}2} = 0$ and (b) η^{jet} for $p_T^{\text{jet}1} = p_T^{\text{jet}2} = 60$ GeV. Regions of strong correlation are visible at low, medium, high, and very high p_T corresponding to the Z +jet, γ +jet, and MJB calibrations and the single-particle response, as well as in the central and forward jet η regions from the η -intercalibration.

The combinations attempt to group NPs into p_T and η regions where they are most relevant, thereby minimizing the correlation loss and reducing the potential for artificial correlation structures across large regions of jet kinematic phase space. Combinations that group NPs that are dominant in low-, medium-, and high- p_T kinematic regimes are therefore generally favored. The η -intercalibration non-closure uncertainty (Section 5.4.1), being fairly large and localized, and the AFII uncertainty, being specific to a certain type of MC simulation, are not included in this procedure. This procedure is performed using PYTHIA MC simulation, assuming a conservative 50% quark and 50% gluon composition with a 100% uncertainty.

The correlation loss between a strongly reduced representation NP_{red} and the full representation NP_{full} is generally non-negligible, as seen in the matrix of the jet–jet p_T correlation differences shown in Figure 14(b). For two jets with $\eta = 0$, the maximum (mean) p_T correlation loss is -0.39 (-0.13), and is largest between jets in very different kinematic phase space. This simple mean is taken as the average correlation loss over the fine logarithmic p_T bins, excluding bins in kinematically forbidden regions. Sensitivity to this correlation loss is analysis dependent and is determined by the regions in jet p_T – η phase space where the analysis events fall. To allow analyses to probe their sensitivity to this loss, a set of four different strongly reduced representations $\{\text{NP}_{\text{red}}\}$ is generated which varies the regions of greatest correlation loss between them. Each NP_{red} combines the components in a unique way, with different kinematic regions becoming better or worse descriptions of the full correlation matrix. The sensitivity of an analysis to the correlation loss can be quantified by examining the effect of each NP_{red} on the final analysis observable. The four NP_{red} are each derived to focus on one of the following correlation scenarios:

1. the general representation with low-, medium-, and high- p_T kinematic regimes;
2. preservation of low- p_T vs medium- p_T correlation structure as well as η dependencies;
3. preservation of medium- p_T vs high- p_T correlation structure;
4. preservation of very high- p_T correlation structure.

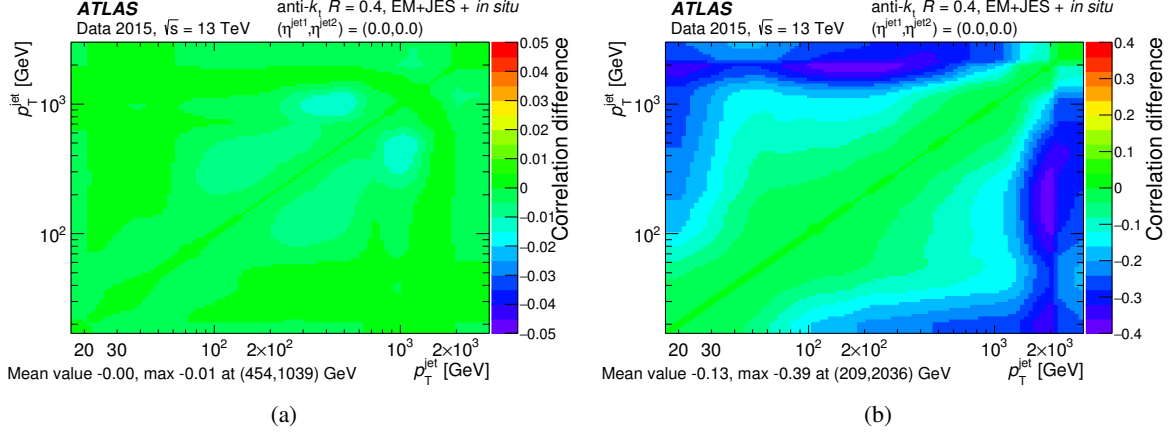


Figure 14: Jet-jet correlation losses after applying (a) the global reduction and (b) subsequent strong reduction as a function of p_T^{jet} for $\eta^{\text{jet}1} = \eta^{\text{jet}2} = 0$. The correlation loss is relatively minor from the global reduction and larger from the strong reduction in certain kinematic regions.

When deriving a reduced representation, it can be useful to highlight exceptional uncertainties or vary the way in which they are combined. An uncertainty may exhibit a large anti-correlation across p_T or η , and the anti-correlation information is lost when summed in quadrature with other uncertainties to form a single NP. If such an uncertainty is non-negligible, it is useful to isolate it as a single strongly reduced NP. For uncertainties derived from the comparison of two MC event generators, the correlation structure is not well defined. These NPs can be split into two identical components of complementary weight, such that their combination sums to the original uncertainty for all points in the p_T - η phase space. The split NP can then be divided between two strongly reduced NPs, changing the correlation information in certain kinematic regions. A reduced representation can also recover the correlation information from globally subdominant eigenvectors that were initially combined in the preceding eigen-decomposition. These eigenvectors are smaller overall than others but may be dominant for specific kinematic regions. By keeping these eigenvectors separate until the strong reduction procedure, the correlation structure in kinematic regions of interest can be better probed, at the expense of an increased loss in the overall global correlation structure.

To ensure the set of four reduced representations $\{\text{NP}_{\text{red}}\}$ is suitable in bracketing the full correlation matrix, a metric is defined to quantify the uncovered correlation loss of any derived set. The metric measures the maximum correlation difference between any two reduced representations $\text{NP}_{\text{red}} \in \{\text{NP}_{\text{red}}\}$ and compares it with the smallest difference between the full representation NP_{full} and any NP_{red} . If the difference between any two NP_{red} is larger than that of any NP_{red} and NP_{full} , then analyses that bracket their sensitivity to correlation loss with $\{\text{NP}_{\text{red}}\}$ are conservative with respect to any differences with the full representation. The metric to quantify the uncovered correlation loss of any derived $\{\text{NP}_{\text{red}}\}$ is defined as

$$\min_{i \in \{\text{NP}_{\text{red}}\}} |C_{\text{full}} - C_{\text{red}}^i| - \max_{i, j \in \{\text{NP}_{\text{red}}\}, i \neq j} |C_{\text{red}}^i - C_{\text{red}}^j|, \quad (4)$$

where C_{full} is the correlation coefficient for the full NP set and C_{red} is that of a reduced NP representation. The metric is calculated throughout the jet-jet p_T - η phase space, and is not allowed to be greater than

zero.

This uncovered correlation loss is shown in Figure 15 for several points in the four-dimensional jet–jet p_T – η phase space. It is shown as a function of p_T for several distinct regions of η in steps of $\Delta\eta = 0.5$. For each η region, the maximum correlation loss not covered by differences between the reduced representations is above the level of -0.3 with a mean at or above -0.01 . The regions of maximum difference are very limited in kinematic phase space and therefore have a minimal impact, with the strongly reduced representation procedure probing almost all of the JES correlation structure. The majority of ATLAS searches using 2015 data have been shown to be insensitive to this limited loss of correlation information and have used the strongly reduced NPs successfully, such as the dijet [40] and multijet [41] resonance searches.

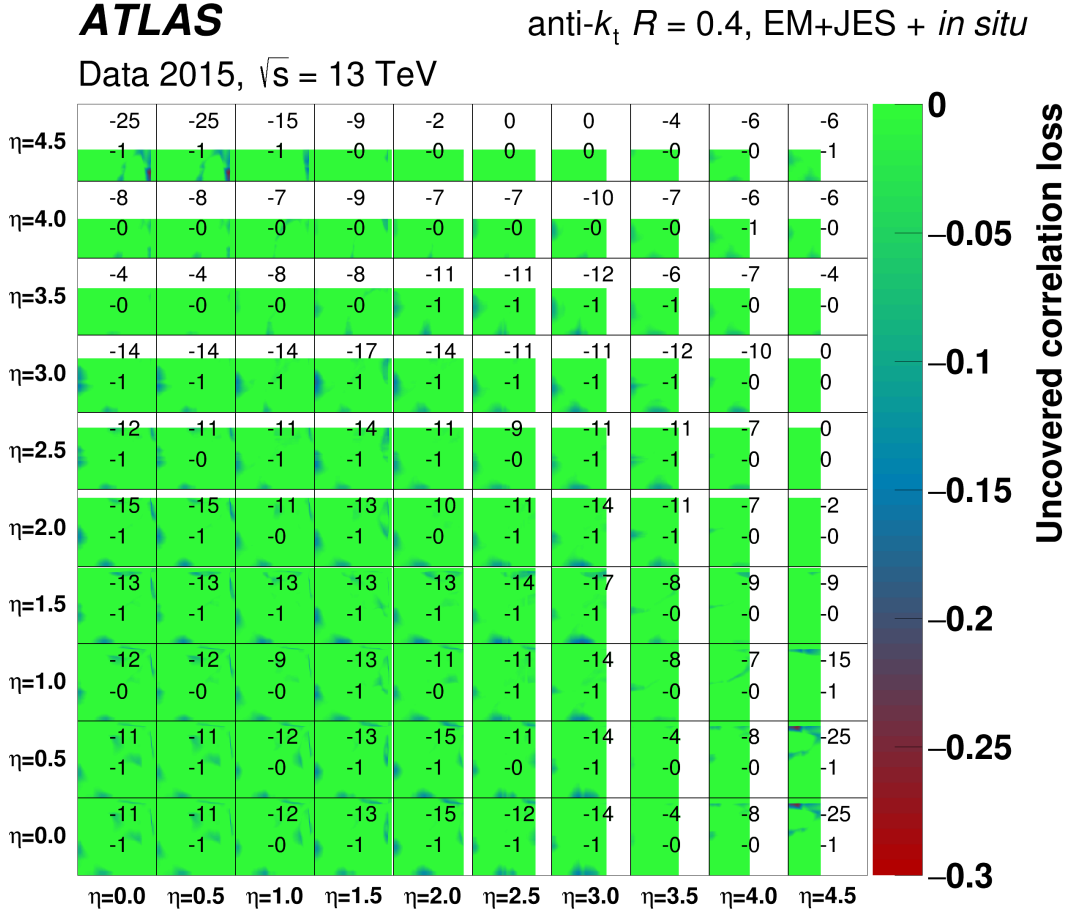


Figure 15: Uncovered jet–jet correlation loss between the full NP representation and the set of strongly reduced representations, showing regions which are not fully covered by the strongly reduced set of four representations. The uncovered correlation loss is calculated by the metric given in Eq. (4). The uncovered correlation loss is explored in the four-dimensional jet–jet p_T – η phase space. Each subplot shows the uncovered correlation loss as a function of p_T , and subplots are shown for several regions of η in steps of $\Delta\eta = 0.5$. White regions represent the kinematically forbidden phase space beyond the reach of $\sqrt{s} = 13$ TeV. The top (bottom) number in each subplot gives the maximum (mean) uncovered correlation loss, multiplied by a factor of 100 for visibility, with the mean excluding kinematically forbidden regions.

7 Conclusions

The derivation of the 2015 ATLAS calibration of the jet energy scale is presented for EM-scale anti- k_t $R = 0.4$ jets. An area-based pile-up correction and a pile-up-sensitive residual correction are derived to reduce contamination from the busy detector environment at a bunch spacing of 25 ns. Absolute jet energy scale and η calibrations are derived from Monte Carlo simulation to correct the jet four-momentum to the particle-level energy scale and to improve the jet angular resolution. The global sequential calibration is derived from p_T -sensitive observables to improve the jet resolution and to account for the differing energy response between quark- and gluon-initiated jets.

In situ calibrations are derived using 3.2 fb^{-1} of $\sqrt{s} = 13 \text{ TeV}$ proton–proton collision data collected by ATLAS in 2015 at the LHC. Dijet events are selected to measure the p_T - and η -dependent response of forward jets with respect to central jets. A p_T -dependent correction is derived by balancing the p_T of jets against reference photons and Z bosons decaying into electrons and muons. A final correction is derived for higher- p_T jets through multijet events in which the highest- p_T jet is significantly more energetic than the others. The *in situ* corrections are combined in their overlapping p_T ranges to provide a single consistent calibration at a level of 4% at 20 GeV and 2% at 2 TeV.

The uncertainty in the jet energy scale is consistent with previous results in 2011 using 7 TeV data, and is at a level of 4.5% at 20 GeV, 1% at 200 GeV, and 2% at 2 TeV for an inclusive dijet sample. The uncertainties are fairly constant with respect to η , and a dedicated uncertainty is introduced for $2.0 < |\eta| < 2.6$ to account for details in the calorimeter energy reconstruction. A new method for combining systematic uncertainties into a strongly reduced set while preserving correlations is described. The full set of 80 uncertainties is reduced to five, and the correlation information loss is probed through a set of four unique combination scenarios.

Acknowledgements

We thank CERN for the very successful operation of the LHC, as well as the support staff from our institutions without whom ATLAS could not be operated efficiently.

We acknowledge the support of ANPCyT, Argentina; YerPhI, Armenia; ARC, Australia; BMWFW and FWF, Austria; ANAS, Azerbaijan; SSTC, Belarus; CNPq and FAPESP, Brazil; NSERC, NRC and CFI, Canada; CERN; CONICYT, Chile; CAS, MOST and NSFC, China; COLCIENCIAS, Colombia; MSMT CR, MPO CR and VSC CR, Czech Republic; DNRF and DNSRC, Denmark; IN2P3-CNRS, CEA-DSM/IRFU, France; SRNSF, Georgia; BMBF, HGF, and MPG, Germany; GSRT, Greece; RGC, Hong Kong SAR, China; ISF, I-CORE and Benozziyo Center, Israel; INFN, Italy; MEXT and JSPS, Japan; CNRST, Morocco; NWO, Netherlands; RCN, Norway; MNiSW and NCN, Poland; FCT, Portugal; MNE/IFA, Romania; MES of Russia and NRC KI, Russian Federation; JINR; MESTD, Serbia; MSSR, Slovakia; ARRS and MIZŠ, Slovenia; DST/NRF, South Africa; MINECO, Spain; SRC and Wallenberg Foundation, Sweden; SERI, SNSF and Cantons of Bern and Geneva, Switzerland; MOST, Taiwan; TAEK, Turkey; STFC, United Kingdom; DOE and NSF, United States of America. In addition, individual groups and members have received support from BCKDF, the Canada Council, CANARIE, CRC, Compute Canada, FQRNT, and the Ontario Innovation Trust, Canada; EPLANET, ERC, ERDF, FP7, Horizon 2020 and Marie Skłodowska-Curie Actions, European Union; Investissements d’Avenir Labex and IDEX, ANR, Région Auvergne and Fondation Partager le Savoir, France; DFG and AvH Foundation,

Germany; Herakleitos, Thales and Aristeia programmes co-financed by EU-ESF and the Greek NSRF; BSF, GIF and Minerva, Israel; BRF, Norway; CERCA Programme Generalitat de Catalunya, Generalitat Valenciana, Spain; the Royal Society and Leverhulme Trust, United Kingdom.

The crucial computing support from all WLCG partners is acknowledged gratefully, in particular from CERN, the ATLAS Tier-1 facilities at TRIUMF (Canada), NDGF (Denmark, Norway, Sweden), CC-IN2P3 (France), KIT/GridKA (Germany), INFN-CNAF (Italy), NL-T1 (Netherlands), PIC (Spain), ASGC (Taiwan), RAL (UK) and BNL (USA), the Tier-2 facilities worldwide and large non-WLCG resource providers. Major contributors of computing resources are listed in Ref. [42].

References

- [1] ATLAS Collaboration, *The ATLAS Experiment at the CERN Large Hadron Collider*, *JINST* **3** (2008) S08003.
- [2] ATLAS Collaboration, *Performance of the ATLAS detector using first collision data*, *JHEP* **09** (2010) 056, arXiv: [1005.5254 \[hep-ex\]](#).
- [3] ATLAS Collaboration, *Jet energy measurement and its systematic uncertainty in proton–proton collisions at $\sqrt{s} = 7$ TeV with the ATLAS detector*, *Eur. Phys. J. C* **75** (2015) 17, arXiv: [1406.0076 \[hep-ex\]](#).
- [4] ATLAS Collaboration, *Performance of pile-up mitigation techniques for jets in pp collisions at $\sqrt{s} = 8$ TeV using the ATLAS detector*, *Eur. Phys. J. C* **76** (2016) 581, arXiv: [1510.03823 \[hep-ex\]](#).
- [5] ATLAS Collaboration, *ATLAS Insertable B-Layer Technical Design Report*, ATLAS-TDR-19, 2010, URL: <https://cds.cern.ch/record/1291633>, *ATLAS Insertable B-Layer Technical Design Report Addendum*, ATLAS-TDR-19-ADD-1, 2012, URL: <https://cds.cern.ch/record/1451888>.
- [6] H. Abreu et al., *Performance of the electronic readout of the ATLAS liquid argon calorimeters*, *JINST* **5** (2010) P09003.
- [7] W. E. Cleland and E. G. Stern, *Signal processing considerations for liquid ionization calorimeters in a high rate environment*, *Nucl. Instrum. Meth. A* **338** (1994) 467.
- [8] ATLAS Collaboration, *Readiness of the ATLAS Tile Calorimeter for LHC collisions*, *Eur. Phys. J. C* **70** (2010) 1193, arXiv: [1007.5423 \[hep-ex\]](#).
- [9] ATLAS Collaboration, *Performance of the ATLAS Trigger System in 2015*, (2016), arXiv: [1611.09661 \[hep-ex\]](#).
- [10] M. Cacciari, G. P. Salam, and G. Soyez, *The anti- k_t jet clustering algorithm*, *JHEP* **04** (2008) 063, arXiv: [0802.1189 \[hep-ph\]](#).
- [11] M. Cacciari, G. P. Salam, and G. Soyez, *FastJet user manual*, *Eur. Phys. J. C* **72** (2012) 1896, arXiv: [1111.6097 \[hep-ph\]](#).
- [12] ATLAS Collaboration, *Topological cell clustering in the ATLAS calorimeters and its performance in LHC Run 1*, (2016), arXiv: [1603.02934 \[hep-ex\]](#).

- [13] ATLAS Collaboration, *Jet energy measurement with the ATLAS detector in proton–proton collisions at $\sqrt{s} = 7$ TeV*, *Eur. Phys. J. C* **73** (2013) 2304, arXiv: [1112.6426 \[hep-ex\]](#).
- [14] ATLAS Collaboration, *A neural network clustering algorithm for the ATLAS silicon pixel detector*, *JINST* **9** (2014) P09009, arXiv: [1406.7690 \[hep-ex\]](#).
- [15] M. Cacciari and G. P. Salam, *Pileup subtraction using jet areas*, *Phys. Lett. B* **659** (2008) 119, arXiv: [0707.1378 \[hep-ph\]](#).
- [16] ATLAS Collaboration, *Muon reconstruction performance of the ATLAS detector in proton–proton collision data at $\sqrt{s} = 13$ TeV*, *Eur. Phys. J. C* **76** (2016) 292, arXiv: [1603.05598 \[hep-ex\]](#).
- [17] P. Nason, *A New method for combining NLO QCD with shower Monte Carlo algorithms*, *JHEP* **11** (2004) 040, arXiv: [hep-ph/0409146](#).
- [18] S. Frixione, P. Nason, and C. Oleari, *Matching NLO QCD computations with Parton Shower simulations: the POWHEG method*, *JHEP* **11** (2007) 070, arXiv: [0709.2092 \[hep-ph\]](#).
- [19] S. Alioli, P. Nason, C. Oleari, and E. Re, *A general framework for implementing NLO calculations in shower Monte Carlo programs: the POWHEG BOX*, *JHEP* **06** (2010) 043, arXiv: [1002.2581 \[hep-ph\]](#).
- [20] H.-L. Lai et al., *New parton distributions for collider physics*, *Phys. Rev. D* **82** (2010) 074024, arXiv: [1007.2241 \[hep-ph\]](#).
- [21] T. Sjöstrand, S. Mrenna, and P. Z. Skands, *A Brief Introduction to PYTHIA 8.1*, *Comput. Phys. Commun.* **178** (2008) 852, arXiv: [0710.3820 \[hep-ph\]](#).
- [22] R. Corke and T. Sjöstrand, *Improved parton showers at large transverse momenta*, *Eur. Phys. J. C* **69** (2010) 1, arXiv: [1003.2384 \[hep-ph\]](#).
- [23] ATLAS Collaboration, *ATLAS Pythia 8 tunes to 7 TeV data*, ATL-PHYS-PUB-2014-021, 2014, URL: <https://cds.cern.ch/record/1966419>.
- [24] ATLAS Collaboration, *Example ATLAS tunes of PYTHIA8, PYTHIA6 and POWHEG to an observable sensitive to Z boson transverse momentum*, ATL-PHYS-PUB-2013-017, 2013, URL: <https://cds.cern.ch/record/1629317>.
- [25] S. Carrazza, S. Forte, and J. Rojo, *Parton Distributions and Event Generators*, (2013) 89, arXiv: [1311.5887 \[hep-ph\]](#).
- [26] T. Gleisberg, S. Hoeche, F. Krauss, M. Schonherr, S. Schumann, et al., *Event generation with SHERPA 1.1*, *JHEP* **02** (2009) 007, arXiv: [0811.4622 \[hep-ph\]](#).
- [27] S. Catani, F. Krauss, R. Kuhn, and B. R. Webber, *QCD matrix elements + parton showers*, *JHEP* **11** (2001) 063, arXiv: [hep-ph/0109231](#).
- [28] M. Bahr et al., *Herwig++ Physics and Manual*, *Eur. Phys. J. C* **58** (2008) 639, arXiv: [0803.0883 \[hep-ph\]](#).
- [29] G. Corcella et al., *HERWIG 6: An Event generator for hadron emission reactions with interfering gluons (including supersymmetric processes)*, *JHEP* **01** (2001) 010, arXiv: [hep-ph/0011363](#).
- [30] J. Pumplin et al., *New generation of parton distributions with uncertainties from global QCD analysis*, *JHEP* **07** (2002) 012, arXiv: [hep-ph/0201195](#).

- [31] S. Gieseke, C. Rohr, and A. Siodmok, *Colour reconnections in Herwig++*, *Eur. Phys. J. C* **72** (2012) 2225, arXiv: [1206.0041 \[hep-ph\]](#).
- [32] ATLAS Collaboration, *The ATLAS Simulation Infrastructure*, *Eur. Phys. J. C* **70** (2010) 823, arXiv: [1005.4568 \[hep-ex\]](#).
- [33] S. Agostinelli et al., *GEANT4: A simulation toolkit*, *Nucl. Instrum. Meth. A* **506** (2003) 250.
- [34] ATLAS Collaboration, *A measurement of the calorimeter response to single hadrons and determination of the jet energy scale uncertainty using LHC Run-1 pp-collision data with the ATLAS detector*, *Eur. Phys. J. C* **77** (2017) 26, arXiv: [1607.08842 \[hep-ex\]](#).
- [35] ATLAS Collaboration, *Luminosity determination in pp collisions at $\sqrt{s} = 8$ TeV using the ATLAS detector at the LHC*, *Eur. Phys. J. C* **76** (2016) 653, arXiv: [1608.03953 \[hep-ex\]](#).
- [36] S. D. Ellis and D. E. Soper, *Successive combination jet algorithm for hadron collisions*, *Phys. Rev. D* **48** (1993) 3160, arXiv: [hep-ph/9305266](#).
- [37] G. Bohm and G. Zech, *Introduction to statistics and data analysis for physicists*, Hamburg: Verl. Dt. Elektronen-Synchrotron, 2010 336, ISBN: [978-3-935702-41-6](#).
- [38] ATLAS Collaboration, *Electron and photon energy calibration with the ATLAS detector using LHC Run 1 data*, *Eur. Phys. J. C* **74** (2014) 3071, arXiv: [1407.5063 \[hep-ex\]](#).
- [39] ATLAS Collaboration, *Measurement of the inclusive isolated prompt photon cross section in pp collisions at $\sqrt{s} = 7$ TeV with the ATLAS detector*, *Phys. Rev. D* **83** (2011) 052005, arXiv: [1012.4389 \[hep-ex\]](#).
- [40] ATLAS Collaboration, *Search for New Phenomena in Dijet Mass and Angular Distributions from pp Collisions at $\sqrt{s} = 13$ TeV with the ATLAS Detector*, *Phys. Lett. B* **754** (2016) 302, arXiv: [1512.01530 \[hep-ex\]](#).
- [41] ATLAS Collaboration, *Search for strong gravity in multijet final states produced in pp collisions at $\sqrt{s} = 13$ TeV using the ATLAS detector at the LHC*, *JHEP* **03** (2016) 026, arXiv: [1512.02586 \[hep-ex\]](#).
- [42] ATLAS Collaboration, *ATLAS Computing Acknowledgements 2016–2017*, ATL-GEN-PUB-2016-002, URL: <https://cds.cern.ch/record/2202407>.

The ATLAS Collaboration

M. Aaboud^{137d}, G. Aad⁸⁸, B. Abbott¹¹⁵, J. Abdallah⁸, O. Abidinov^{12,*}, B. Abeloos¹¹⁹, S.H. Abidi¹⁶¹, O.S. AbouZeid¹³⁹, N.L. Abraham¹⁵¹, H. Abramowicz¹⁵⁵, H. Abreu¹⁵⁴, R. Abreu¹¹⁸, Y. Abulaiti^{148a,148b}, B.S. Acharya^{167a,167b,a}, S. Adachi¹⁵⁷, L. Adamczyk^{41a}, J. Adelman¹¹⁰, M. Adersberger¹⁰², T. Adye¹³³, A.A. Affolder¹³⁹, T. Agatonovic-Jovin¹⁴, C. Agheorghiesei^{28c}, J.A. Aguilar-Saavedra^{128a,128f}, S.P. Ahlen²⁴, F. Ahmadov^{68,b}, G. Aielli^{135a,135b}, S. Akatsuka⁷¹, H. Akerstedt^{148a,148b}, T.P.A. Åkesson⁸⁴, A.V. Akimov⁹⁸, G.L. Alberghi^{22a,22b}, J. Albert¹⁷², P. Albicocco⁵⁰, M.J. Alconada Verzini⁷⁴, M. Aleksa³², I.N. Aleksandrov⁶⁸, C. Alexa^{28b}, G. Alexander¹⁵⁵, T. Alexopoulos¹⁰, M. Alhroob¹¹⁵, B. Ali¹³⁰, M. Aliev^{76a,76b}, G. Alimonti^{94a}, J. Alison³³, S.P. Alkire³⁸, B.M.M. Allbrooke¹⁵¹, B.W. Allen¹¹⁸, P.P. Allport¹⁹, A. Aloisio^{106a,106b}, A. Alonso³⁹, F. Alonso⁷⁴, C. Alpigiani¹⁴⁰, A.A. Alshehri⁵⁶, M. Alstaty⁸⁸, B. Alvarez Gonzalez³², D. Álvarez Piqueras¹⁷⁰, M.G. Alviggi^{106a,106b}, B.T. Amadio¹⁶, Y. Amaral Coutinho^{26a}, C. Amelung²⁵, D. Amidei⁹², S.P. Amor Dos Santos^{128a,128c}, A. Amorim^{128a,128b}, S. Amoroso³², G. Amundsen²⁵, C. Anastopoulos¹⁴¹, L.S. Ancu⁵², N. Andari¹⁹, T. Andeen¹¹, C.F. Anders^{60b}, J.K. Anders⁷⁷, K.J. Anderson³³, A. Andreazza^{94a,94b}, V. Andrei^{60a}, S. Angelidakis⁹, I. Angelozzi¹⁰⁹, A. Angerami³⁸, A.V. Anisenkov^{111,c}, N. Anjos¹³, A. Annovi^{126a,126b}, C. Antel^{60a}, M. Antonelli⁵⁰, A. Antonov^{100,*}, D.J. Antrim¹⁶⁶, F. Anulli^{134a}, M. Aoki⁶⁹, L. Aperio Bella³², G. Arabidze⁹³, Y. Arai⁶⁹, J.P. Araque^{128a}, V. Araujo Ferraz^{26a}, A.T.H. Arce⁴⁸, R.E. Ardell⁸⁰, F.A. Arduh⁷⁴, J-F. Arguin⁹⁷, S. Argyropoulos⁶⁶, M. Arik^{20a}, A.J. Armbruster¹⁴⁵, L.J. Armitage⁷⁹, O. Arnaez¹⁶¹, H. Arnold⁵¹, M. Arratia³⁰, O. Arslan²³, A. Artamonov⁹⁹, G. Artoni¹²², S. Artz⁸⁶, S. Asai¹⁵⁷, N. Asbah⁴⁵, A. Ashkenazi¹⁵⁵, L. Asquith¹⁵¹, K. Assamagan²⁷, R. Astalos^{146a}, M. Atkinson¹⁶⁹, N.B. Atlay¹⁴³, K. Augsten¹³⁰, G. Avolio³², B. Axen¹⁶, M.K. Ayoub¹¹⁹, G. Azuelos^{97,d}, A.E. Baas^{60a}, M.J. Baca¹⁹, H. Bachacou¹³⁸, K. Bachas^{76a,76b}, M. Backes¹²², M. Backhaus³², P. Bagnaia^{134a,134b}, H. Bahrasemani¹⁴⁴, J.T. Baines¹³³, M. Bajic³⁹, O.K. Baker¹⁷⁹, E.M. Baldin^{111,c}, P. Balek¹⁷⁵, F. Balli¹³⁸, W.K. Balunas¹²⁴, E. Banas⁴², Sw. Banerjee^{176,e}, A.A.E. Bannoura¹⁷⁸, L. Barak³², E.L. Barberio⁹¹, D. Barberis^{53a,53b}, M. Barbero⁸⁸, T. Barillari¹⁰³, M-S Barisits³², T. Barklow¹⁴⁵, N. Barlow³⁰, S.L. Barnes^{36c}, B.M. Barnett¹³³, R.M. Barnett¹⁶, Z. Barnovska-Blenessy^{36a}, A. Baroncelli^{136a}, G. Barone²⁵, A.J. Barr¹²², L. Barranco Navarro¹⁷⁰, F. Barreiro⁸⁵, J. Barreiro Guimarães da Costa^{35a}, R. Bartoldus¹⁴⁵, A.E. Barton⁷⁵, P. Bartos^{146a}, A. Basalae¹²⁵, A. Bassalat^{119,f}, R.L. Bates⁵⁶, S.J. Batista¹⁶¹, J.R. Batley³⁰, M. Battaglia¹³⁹, M. Bauce^{134a,134b}, F. Bauer¹³⁸, H.S. Bawa^{145,g}, J.B. Beacham¹¹³, M.D. Beattie⁷⁵, T. Beau⁸³, P.H. Beauchemin¹⁶⁵, P. Bechtel²³, H.P. Beck^{18,h}, K. Becker¹²², M. Becker⁸⁶, M. Beckingham¹⁷³, C. Becot¹¹², A.J. Beddall^{20e}, A. Beddall^{20b}, V.A. Bednyakov⁶⁸, M. Bedognetti¹⁰⁹, C.P. Bee¹⁵⁰, T.A. Beermann³², M. Begalli^{26a}, M. Begel²⁷, J.K. Behr⁴⁵, A.S. Bell⁸¹, G. Bella¹⁵⁵, L. Bellagamba^{22a}, A. Bellerive³¹, M. Bellomo¹⁵⁴, K. Belotskiy¹⁰⁰, O. Beltramello³², N.L. Belyaev¹⁰⁰, O. Benary^{155,*}, D. Bencheikroun^{137a}, M. Bender¹⁰², K. Bendtz^{148a,148b}, N. Benekos¹⁰, Y. Benhammou¹⁵⁵, E. Benhar Nocchioli¹⁷⁹, J. Benitez⁶⁶, D.P. Benjamin⁴⁸, M. Benoit⁵², J.R. Bensinger²⁵, S. Bentvelsen¹⁰⁹, L. Beresford¹²², M. Beretta⁵⁰, D. Berge¹⁰⁹, E. Bergeaas Kuutmann¹⁶⁸, N. Berger⁵, J. Beringer¹⁶, S. Berlendis⁵⁸, N.R. Bernard⁸⁹, G. Bernardi⁸³, C. Bernius¹⁴⁵, F.U. Bernlochner²³, T. Berry⁸⁰, P. Berta¹³¹, C. Bertella^{35a}, G. Bertoli^{148a,148b}, F. Bertolucci^{126a,126b}, I.A. Bertram⁷⁵, C. Bertsche⁴⁵, D. Bertsche¹¹⁵, G.J. Besjes³⁹, O. Bessidskaia Bylund^{148a,148b}, M. Bessner⁴⁵, N. Besson¹³⁸, C. Betancourt⁵¹, A. Bethani⁸⁷, S. Bethke¹⁰³, A.J. Bevan⁷⁹, J. Beyer¹⁰³, R.M. Bianchi¹²⁷, O. Biebel¹⁰², D. Biedermann¹⁷, R. Bielski⁸⁷, N.V. Biesuz^{126a,126b}, M. Biglietti^{136a}, J. Bilbao De Mendizabal⁵², T.R.V. Billoud⁹⁷, H. Bilokon⁵⁰, M. Bindi⁵⁷, A. Bingul^{20b}, C. Bini^{134a,134b}, S. Biondi^{22a,22b}, T. Bisanz⁵⁷, C. Bittrich⁴⁷, D.M. Bjergaard⁴⁸, C.W. Black¹⁵², J.E. Black¹⁴⁵, K.M. Black²⁴, D. Blackburn¹⁴⁰, R.E. Blair⁶, T. Blazek^{146a}, I. Bloch⁴⁵, C. Blocker²⁵, A. Blue⁵⁶, W. Blum^{86,*}, U. Blumenschein⁷⁹, S. Blunier^{34a}, G.J. Bobbink¹⁰⁹,

V.S. Bobrovnikov^{111,c}, S.S. Bocchetta⁸⁴, A. Bocci⁴⁸, C. Bock¹⁰², M. Boehler⁵¹, D. Boerner¹⁷⁸, D. Bogavac¹⁰², A.G. Bogdanchikov¹¹¹, C. Bohm^{148a}, V. Boisvert⁸⁰, P. Bokan^{168,i}, T. Bold^{41a}, A.S. Boldyrev¹⁰¹, A.E. Bolz^{60b}, M. Bomben⁸³, M. Bona⁷⁹, M. Boonekamp¹³⁸, A. Borisov¹³², G. Borissov⁷⁵, J. Bortfeldt³², D. Bortoletto¹²², V. Bortolotto^{62a,62b,62c}, K. Bos¹⁰⁹, D. Boscherini^{22a}, M. Bosman¹³, J.D. Bossio Sola²⁹, J. Boudreau¹²⁷, J. Bouffard², E.V. Bouhova-Thacker⁷⁵, D. Boumediene³⁷, C. Bourdarios¹¹⁹, S.K. Boutle⁵⁶, A. Boveia¹¹³, J. Boyd³², I.R. Boyko⁶⁸, J. Bracinik¹⁹, A. Brandt⁸, G. Brandt⁵⁷, O. Brandt^{60a}, U. Bratzler¹⁵⁸, B. Brau⁸⁹, J.E. Brau¹¹⁸, W.D. Breaden Madden⁵⁶, K. Brendlinger⁴⁵, A.J. Brennan⁹¹, L. Brenner¹⁰⁹, R. Brenner¹⁶⁸, S. Bressler¹⁷⁵, D.L. Briglin¹⁹, T.M. Bristow⁴⁹, D. Britton⁵⁶, D. Britzger⁴⁵, F.M. Brochu³⁰, I. Brock²³, R. Brock⁹³, G. Brooijmans³⁸, T. Brooks⁸⁰, W.K. Brooks^{34b}, J. Brosamer¹⁶, E. Brost¹¹⁰, J.H. Broughton¹⁹, P.A. Bruckman de Renstrom⁴², D. Bruncko^{146b}, A. Bruni^{22a}, G. Bruni^{22a}, L.S. Bruni¹⁰⁹, B.H. Brunt³⁰, M. Bruschi^{22a}, N. Bruscinò²³, P. Bryant³³, L. Bryngemark⁴⁵, T. Buanes¹⁵, Q. Buat¹⁴⁴, P. Buchholz¹⁴³, A.G. Buckley⁵⁶, I.A. Budagov⁶⁸, F. Buehrer⁵¹, M.K. Bugge¹²¹, O. Bulekov¹⁰⁰, D. Bullock⁸, T.J. Burch¹¹⁰, H. Burckhart³², S. Burdin⁷⁷, C.D. Burgard⁵¹, A.M. Burger⁵, B. Burghgrave¹¹⁰, K. Burka⁴², S. Burke¹³³, I. Burmeister⁴⁶, J.T.P. Burr¹²², E. Busato³⁷, D. Büscher⁵¹, V. Büscher⁸⁶, P. Bussey⁵⁶, J.M. Butler²⁴, C.M. Buttar⁵⁶, J.M. Butterworth⁸¹, P. Butti³², W. Buttinger²⁷, A. Buzatu^{35c}, A.R. Buzykaev^{111,c}, S. Cabrera Urbán¹⁷⁰, D. Caforio¹³⁰, V.M. Cairo^{40a,40b}, O. Cakir^{4a}, N. Calace⁵², P. Calafiura¹⁶, A. Calandri⁸⁸, G. Calderini⁸³, P. Calfayan⁶⁴, G. Callea^{40a,40b}, L.P. Caloba^{26a}, S. Calvente Lopez⁸⁵, D. Calvet³⁷, S. Calvet³⁷, T.P. Calvet⁸⁸, R. Camacho Toro³³, S. Camarda³², P. Camarri^{135a,135b}, D. Cameron¹²¹, R. Caminal Armadans¹⁶⁹, C. Camincher⁵⁸, S. Campana³², M. Campanelli⁸¹, A. Camplani^{94a,94b}, A. Campoverde¹⁴³, V. Canale^{106a,106b}, M. Cano Bret^{36c}, J. Cantero¹¹⁶, T. Cao¹⁵⁵, M.D.M. Capeans Garrido³², I. Caprini^{28b}, M. Caprini^{28b}, M. Capua^{40a,40b}, R.M. Carbone³⁸, R. Cardarelli^{135a}, F. Cardillo⁵¹, I. Carli¹³¹, T. Carli³², G. Carlino^{106a}, B.T. Carlson¹²⁷, L. Carminati^{94a,94b}, R.M.D. Carney^{148a,148b}, S. Caron¹⁰⁸, E. Carquin^{34b}, S. Carrá^{94a,94b}, G.D. Carrillo-Montoya³², J. Carvalho^{128a,128c}, D. Casadei¹⁹, M.P. Casado^{13,j}, M. Casolino¹³, D.W. Casper¹⁶⁶, R. Castelijns¹⁰⁹, V. Castillo Gimenez¹⁷⁰, N.F. Castro^{128a,k}, A. Catinaccio³², J.R. Catmore¹²¹, A. Cattai³², J. Caudron²³, V. Cavaliere¹⁶⁹, E. Cavallaro¹³, D. Cavalli^{94a}, M. Cavalli-Sforza¹³, V. Cavasinni^{126a,126b}, E. Celebi^{20a}, F. Ceradini^{136a,136b}, L. Cerda Alberich¹⁷⁰, A.S. Cerqueira^{26b}, A. Cerri¹⁵¹, L. Cerrito^{135a,135b}, F. Cerutti¹⁶, A. Cervelli¹⁸, S.A. Cetin^{20d}, A. Chafaq^{137a}, D. Chakraborty¹¹⁰, S.K. Chan⁵⁹, W.S. Chan¹⁰⁹, Y.L. Chan^{62a}, P. Chang¹⁶⁹, J.D. Chapman³⁰, D.G. Charlton¹⁹, C.C. Chau¹⁶¹, C.A. Chavez Barajas¹⁵¹, S. Che¹¹³, S. Cheatham^{167a,167c}, A. Chegwidan⁹³, S. Chekanov⁶, S.V. Chekulaev^{163a}, G.A. Chelkov^{68,l}, M.A. Chelstowska³², C. Chen⁶⁷, H. Chen²⁷, S. Chen^{35b}, S. Chen¹⁵⁷, X. Chen^{35c,m}, Y. Chen⁷⁰, H.C. Cheng⁹², H.J. Cheng^{35a}, A. Cheplakov⁶⁸, E. Cheremushkina¹³², R. Cherkaoui El Moursli^{137e}, V. Chernyatin^{27,*}, E. Cheu⁷, L. Chevalier¹³⁸, V. Chiarella⁵⁰, G. Chiarelli^{126a,126b}, G. Chiodini^{76a}, A.S. Chisholm³², A. Chitan^{28b}, Y.H. Chiu¹⁷², M.V. Chizhov⁶⁸, K. Choi⁶⁴, A.R. Chomont³⁷, S. Chouridou¹⁵⁶, V. Christodoulou⁸¹, D. Chromek-Burckhart³², M.C. Chu^{62a}, J. Chudoba¹²⁹, A.J. Chuinard⁹⁰, J.J. Chwastowski⁴², L. Chytka¹¹⁷, A.K. Ciftci^{4a}, D. Cinca⁴⁶, V. Cindro⁷⁸, I.A. Cioara²³, C. Ciocca^{22a,22b}, A. Ciocio¹⁶, F. Ciotto^{106a,106b}, Z.H. Citron¹⁷⁵, M. Citterio^{94a}, M. Ciubancan^{28b}, A. Clark⁵², B.L. Clark⁵⁹, M.R. Clark³⁸, P.J. Clark⁴⁹, R.N. Clarke¹⁶, C. Clement^{148a,148b}, Y. Coadou⁸⁸, M. Cobal^{167a,167c}, A. Coccaro⁵², J. Cochran⁶⁷, L. Colasurdo¹⁰⁸, B. Cole³⁸, A.P. Colijn¹⁰⁹, J. Collot⁵⁸, T. Colombo¹⁶⁶, P. Conde Muiño^{128a,128b}, E. Coniavitis⁵¹, S.H. Connell^{147b}, I.A. Connelly⁸⁷, S. Constantinescu^{28b}, G. Conti³², F. Conventi^{106a,n}, M. Cooke¹⁶, A.M. Cooper-Sarkar¹²², F. Cormier¹⁷¹, K.J.R. Cormier¹⁶¹, M. Corradi^{134a,134b}, F. Corriveau^{90,o}, A. Cortes-Gonzalez³², G. Cortiana¹⁰³, G. Costa^{94a}, M.J. Costa¹⁷⁰, D. Costanzo¹⁴¹, G. Cottin³⁰, G. Cowan⁸⁰, B.E. Cox⁸⁷, K. Cranmer¹¹², S.J. Crawley⁵⁶, R.A. Creager¹²⁴, G. Cree³¹, S. Crépe-Renaudin⁵⁸, F. Crescioli⁸³, W.A. Cribbs^{148a,148b}, M. Cristinziani²³, V. Croft¹⁰⁸, G. Crossetti^{40a,40b}, A. Cueto⁸⁵, T. Cuhadar Donszelmann¹⁴¹,

A.R. Cukierman¹⁴⁵, J. Cummings¹⁷⁹, M. Curatolo⁵⁰, J. Cúth⁸⁶, H. Czirr¹⁴³, P. Czodrowski³²,
 G. D'amen^{22a,22b}, S. D'Auria⁵⁶, M. D'Onofrio⁷⁷, M.J. Da Cunha Sargedas De Sousa^{128a,128b},
 C. Da Via⁸⁷, W. Dabrowski^{41a}, T. Dado^{146a}, T. Dai⁹², O. Dale¹⁵, F. Dallaire⁹⁷, C. Dallapiccola⁸⁹,
 M. Dam³⁹, J.R. Dandoy¹²⁴, N.P. Dang¹⁷⁶, A.C. Daniells¹⁹, N.S. Dann⁸⁷, M. Danning¹⁷¹,
 M. Dano Hoffmann¹³⁸, V. Dao¹⁵⁰, G. Darbo^{53a}, S. Darmora⁸, J. Dassoulas³, A. Dattagupta¹¹⁸,
 T. Daubney⁴⁵, W. Davey²³, C. David⁴⁵, T. Davidek¹³¹, M. Davies¹⁵⁵, P. Davison⁸¹, E. Dawe⁹¹,
 I. Dawson¹⁴¹, K. De⁸, R. de Asmundis^{106a}, A. De Benedetti¹¹⁵, S. De Castro^{22a,22b}, S. De Cecco⁸³,
 N. De Groot¹⁰⁸, P. de Jong¹⁰⁹, H. De la Torre⁹³, F. De Lorenzi⁶⁷, A. De Maria⁵⁷, D. De Pedis^{134a},
 A. De Salvo^{134a}, U. De Sanctis^{135a,135b}, A. De Santo¹⁵¹, K. De Vasconcelos Corga⁸⁸,
 J.B. De Vivie De Regie¹¹⁹, W.J. Dearnaley⁷⁵, R. Debbe²⁷, C. Debenedetti¹³⁹, D.V. Dedovich⁶⁸,
 N. Dehghanian³, I. Deigaard¹⁰⁹, M. Del Gaudio^{40a,40b}, J. Del Peso⁸⁵, T. Del Prete^{126a,126b},
 D. Delgove¹¹⁹, F. Deliot¹³⁸, C.M. Delitzsch⁵², A. Dell'Acqua³², L. Dell'Asta²⁴, M. Dell'Orso^{126a,126b},
 M. Della Pietra^{106a,106b}, D. della Volpe⁵², M. Delmastro⁵, C. Delporte¹¹⁹, P.A. Delsart⁵⁸,
 D.A. DeMarco¹⁶¹, S. Demers¹⁷⁹, M. Demichev⁶⁸, A. Demilly⁸³, S.P. Denisov¹³², D. Denysiuk¹³⁸,
 D. Derendarz⁴², J.E. Derkaoui^{137d}, F. Derue⁸³, P. Dervan⁷⁷, K. Desch²³, C. Deterre⁴⁵, K. Dette⁴⁶,
 M.R. Devesa²⁹, P.O. Deviveiros³², A. Dewhurst¹³³, S. Dhaliwal²⁵, F.A. Di Bello⁵²,
 A. Di Ciaccio^{135a,135b}, L. Di Ciaccio⁵, W.K. Di Clemente¹²⁴, C. Di Donato^{106a,106b}, A. Di Girolamo³²,
 B. Di Girolamo³², B. Di Micco^{136a,136b}, R. Di Nardo³², K.F. Di Petrillo⁵⁹, A. Di Simone⁵¹,
 R. Di Sipio¹⁶¹, D. Di Valentino³¹, C. Diaconu⁸⁸, M. Diamond¹⁶¹, F.A. Dias³⁹, M.A. Diaz^{34a},
 E.B. Diehl⁹², J. Dietrich¹⁷, S. Díez Cornell⁴⁵, A. Dimitrievska¹⁴, J. Dingfelder²³, P. Dita^{28b}, S. Dita^{28b},
 F. Dittus³², F. Djama⁸⁸, T. Djobava^{54b}, J.I. Djuvsland^{60a}, M.A.B. do Vale^{26c}, D. Dobos³², M. Dobre^{28b},
 C. Doglioni⁸⁴, J. Dolejsi¹³¹, Z. Dolezal¹³¹, M. Donadelli^{26d}, S. Donati^{126a,126b}, P. Dondero^{123a,123b},
 J. Donini³⁷, J. Dopke¹³³, A. Doria^{106a}, M.T. Dova⁷⁴, A.T. Doyle⁵⁶, E. Drechsler⁵⁷, M. Dris¹⁰, Y. Du^{36b},
 J. Duarte-Campderros¹⁵⁵, A. Dubreuil⁵², E. Duchovni¹⁷⁵, G. Duckeck¹⁰², A. Ducourthial⁸³,
 O.A. Ducu^{97,p}, D. Duda¹⁰⁹, A. Dudarev³², A.Ch. Dudder⁸⁶, E.M. Duffield¹⁶, L. Duflost¹¹⁹,
 M. Dührssen³², M. Dumancic¹⁷⁵, A.E. Dumitriu^{28b}, A.K. Duncan⁵⁶, M. Dunford^{60a}, H. Duran Yildiz^{4a},
 M. Düren⁵⁵, A. Durglishvili^{54b}, D. Duschinger⁴⁷, B. Dutta⁴⁵, M. Dyndal⁴⁵, C. Eckardt⁴⁵, K.M. Ecker¹⁰³,
 R.C. Edgar⁹², T. Eifert³², G. Eigen¹⁵, K. Einsweiler¹⁶, T. Ekelof¹⁶⁸, M. El Kacimi^{137c}, R. El Kosseifi⁸⁸,
 V. Ellajosyula⁸⁸, M. Ellert¹⁶⁸, S. Elles⁵, F. Ellinghaus¹⁷⁸, A.A. Elliot¹⁷², N. Ellis³², J. Elmsheuser²⁷,
 M. Elsing³², D. Emelianov¹³³, Y. Enari¹⁵⁷, O.C. Endner⁸⁶, J.S. Ennis¹⁷³, J. Erdmann⁴⁶, A. Ereditato¹⁸,
 G. Ernis¹⁷⁸, M. Ernst²⁷, S. Errede¹⁶⁹, E. Ertel⁸⁶, M. Escalier¹¹⁹, C. Escobar¹²⁷, B. Esposito⁵⁰,
 O. Estrada Pastor¹⁷⁰, A.I. Etienne¹³⁸, E. Etzion¹⁵⁵, H. Evans⁶⁴, A. Ezhilov¹²⁵, M. Ezzi^{137e},
 F. Fabbri^{22a,22b}, L. Fabbri^{22a,22b}, G. Facini³³, R.M. Fakhruddinov¹³², S. Falciano^{134a}, R.J. Falla⁸¹,
 J. Faltova³², Y. Fang^{35a}, M. Fanti^{94a,94b}, A. Farbin⁸, A. Farilla^{136a}, C. Farina¹²⁷, E.M. Farina^{123a,123b},
 T. Farooque⁹³, S. Farrell¹⁶, S.M. Farrington¹⁷³, P. Farthouat³², F. Fassi^{137e}, P. Fassnacht³²,
 D. Fassouliotis⁹, M. Faucci Giannelli⁸⁰, A. Favareto^{53a,53b}, W.J. Fawcett¹²², L. Fayard¹¹⁹,
 O.L. Fedin^{125,q}, W. Fedorko¹⁷¹, S. Feigl¹²¹, L. Felgioni⁸⁸, C. Feng^{36b}, E.J. Feng³², H. Feng⁹²,
 M.J. Fenton⁵⁶, A.B. Fenyuk¹³², L. Feremenga⁸, P. Fernandez Martinez¹⁷⁰, S. Fernandez Perez¹³,
 J. Ferrando⁴⁵, A. Ferrari¹⁶⁸, P. Ferrari¹⁰⁹, R. Ferrari^{123a}, D.E. Ferreira de Lima^{60b}, A. Ferrer¹⁷⁰,
 D. Ferrere⁵², C. Ferretti⁹², F. Fiedler⁸⁶, A. Filipčić⁷⁸, M. Filipuzzi⁴⁵, F. Filthaut¹⁰⁸, M. Fincke-Keeler¹⁷²,
 K.D. Finelli¹⁵², M.C.N. Fiolhais^{128a,128c,r}, L. Fiorini¹⁷⁰, A. Fischer², C. Fischer¹³, J. Fischer¹⁷⁸,
 W.C. Fisher⁹³, N. Flaschel⁴⁵, I. Fleck¹⁴³, P. Fleischmann⁹², R.R.M. Fletcher¹²⁴, T. Flick¹⁷⁸,
 B.M. Flierl¹⁰², L.R. Flores Castillo^{62a}, M.J. Flowerdew¹⁰³, G.T. Forcolin⁸⁷, A. Formica¹³⁸,
 F.A. Förster¹³, A. Forti⁸⁷, A.G. Foster¹⁹, D. Fournier¹¹⁹, H. Fox⁷⁵, S. Fracchia¹⁴¹, P. Francavilla⁸³,
 M. Franchini^{22a,22b}, S. Franchino^{60a}, D. Francis³², L. Franconi¹²¹, M. Franklin⁵⁹, M. Frate¹⁶⁶,
 M. Fraternali^{123a,123b}, D. Freeborn⁸¹, S.M. Fressard-Batranceanu³², B. Freund⁹⁷, D. Froidevaux³²,
 J.A. Frost¹²², C. Fukunaga¹⁵⁸, T. Fusayasu¹⁰⁴, J. Fuster¹⁷⁰, C. Gabaldon⁵⁸, O. Gabizon¹⁵⁴,

A. Gabrielli^{22a,22b}, A. Gabrielli¹⁶, G.P. Gach^{41a}, S. Gadatsch³², S. Gadowski⁸⁰, G. Gagliardi^{53a,53b},
 L.G. Gagnon⁹⁷, C. Galea¹⁰⁸, B. Galhardo^{128a,128c}, E.J. Gallas¹²², B.J. Gallop¹³³, P. Gallus¹³⁰,
 G. Galster³⁹, K.K. Gan¹¹³, S. Ganguly³⁷, J. Gao^{36a}, Y. Gao⁷⁷, Y.S. Gao^{145.g}, F.M. Garay Walls⁴⁹,
 C. García¹⁷⁰, J.E. García Navarro¹⁷⁰, M. Garcia-Sciveres¹⁶, R.W. Gardner³³, N. Garelli¹⁴⁵,
 V. Garonne¹²¹, A. Gascon Bravo⁴⁵, K. Gasnikova⁴⁵, C. Gatti⁵⁰, A. Gaudiello^{53a,53b}, G. Gaudio^{123a},
 I.L. Gavrilenko⁹⁸, C. Gay¹⁷¹, G. Gaycken²³, E.N. Gazis¹⁰, C.N.P. Gee¹³³, J. Geisen⁵⁷, M. Geisen⁸⁶,
 M.P. Geisler^{60a}, K. Gellerstedt^{148a,148b}, C. Gemme^{53a}, M.H. Genest⁵⁸, C. Geng⁹², S. Gentile^{134a,134b},
 C. Gentsos¹⁵⁶, S. George⁸⁰, D. Gerbaudo¹³, A. Gershon¹⁵⁵, S. Ghasemi¹⁴³, M. Ghneimat²³,
 B. Giacobbe^{22a}, S. Giagu^{134a,134b}, P. Giannetti^{126a,126b}, S.M. Gibson⁸⁰, M. Gignac¹⁷¹, M. Gilchriese¹⁶,
 D. Gillberg³¹, G. Gilles¹⁷⁸, D.M. Gingrich^{3,d}, N. Giokaris^{9,*}, M.P. Giordani^{167a,167c}, F.M. Giorgi^{22a},
 P.F. Giraud¹³⁸, P. Giromini⁵⁹, D. Giugni^{94a}, F. Giuli¹²², C. Giuliani¹⁰³, M. Giulini^{60b}, B.K. Gjølsten¹²¹,
 S. Gkaitatzis¹⁵⁶, I. Gkialas⁹, E.L. Gkoukousis¹³⁹, L.K. Gladilin¹⁰¹, C. Glasman⁸⁵, J. Glatzer¹³,
 P.C.F. Glaysheer⁴⁵, A. Glazov⁴⁵, M. Goblirsch-Kolb²⁵, J. Godlewski⁴², S. Goldfarb⁹¹, T. Golling⁵²,
 D. Golubkov¹³², A. Gomes^{128a,128b,128d}, R. Gonçalo^{128a}, R. Goncalves Gama^{26a},
 J. Goncalves Pinto Firmino Da Costa¹³⁸, G. Gonella⁵¹, L. Gonella¹⁹, A. Gongadze⁶⁸,
 S. González de la Hoz¹⁷⁰, S. Gonzalez-Sevilla⁵², L. Goossens³², P.A. Gorbounov⁹⁹, H.A. Gordon²⁷,
 I. Gorelov¹⁰⁷, B. Gorini³², E. Gorini^{76a,76b}, A. Gorišek⁷⁸, A.T. Goshaw⁴⁸, C. Gössling⁴⁶, M.I. Gostkin⁶⁸,
 C.R. Goudet¹¹⁹, D. Goujdami^{137c}, A.G. Goussiou¹⁴⁰, N. Govender^{147b,s}, E. Gozani¹⁵⁴, L. Graber⁵⁷,
 I. Grabowska-Bold^{41a}, P.O.J. Gradin¹⁶⁸, J. Gramling¹⁶⁶, E. Gramstad¹²¹, S. Grancagnolo¹⁷,
 V. Gratchev¹²⁵, P.M. Gravila^{28f}, C. Gray⁵⁶, H.M. Gray³², Z.D. Greenwood^{82,t}, C. Grefe²³,
 K. Gregersen⁸¹, I.M. Gregor⁴⁵, P. Grenier¹⁴⁵, K. Grevtsov⁵, J. Griffiths⁸, A.A. Grillo¹³⁹, K. Grimm⁷⁵,
 S. Grinstein^{13,u}, Ph. Gris³⁷, J.-F. Grivaz¹¹⁹, S. Groh⁸⁶, E. Gross¹⁷⁵, J. Grosse-Knetter⁵⁷, G.C. Grossi⁸²,
 Z.J. Grout⁸¹, A. Grummer¹⁰⁷, L. Guan⁹², W. Guan¹⁷⁶, J. Guenther⁶⁵, F. Guescini^{163a}, D. Guest¹⁶⁶,
 O. Gueta¹⁵⁵, B. Gui¹¹³, E. Guido^{53a,53b}, T. Guillemin⁵, S. Guindon², U. Gul⁵⁶, C. Gumpert³², J. Guo^{36c},
 W. Guo⁹², Y. Guo^{36a}, R. Gupta⁴³, S. Gupta¹²², G. Gustavino^{134a,134b}, P. Gutierrez¹¹⁵,
 N.G. Gutierrez Ortiz⁸¹, C. Gutsche⁸¹, C. Guyot¹³⁸, M.P. Guzik^{41a}, C. Gwenlan¹²², C.B. Gwilliam⁷⁷,
 A. Haas¹¹², C. Haber¹⁶, H.K. Hadavand⁸, N. Haddad^{137e}, A. Hadeef⁸⁸, S. Hageböck²³, M. Hagihara¹⁶⁴,
 H. Hakobyan^{180,*}, M. Haleem⁴⁵, J. Haley¹¹⁶, G. Halladjian⁹³, G.D. Hallewell⁸⁸, K. Hamacher¹⁷⁸,
 P. Hamal¹¹⁷, K. Hamano¹⁷², A. Hamilton^{147a}, G.N. Hamity¹⁴¹, P.G. Hamnett⁴⁵, L. Han^{36a}, S. Han^{35a},
 K. Hanagaki^{69,v}, K. Hanawa¹⁵⁷, M. Hance¹³⁹, B. Haney¹²⁴, P. Hanke^{60a}, J.B. Hansen³⁹, J.D. Hansen³⁹,
 M.C. Hansen²³, P.H. Hansen³⁹, K. Hara¹⁶⁴, A.S. Hard¹⁷⁶, T. Harenberg¹⁷⁸, F. Hariri¹¹⁹, S. Harkusha⁹⁵,
 R.D. Harrington⁴⁹, P.F. Harrison¹⁷³, F. Hartjes¹⁰⁹, N.M. Hartmann¹⁰², M. Hasegawa⁷⁰, Y. Hasegawa¹⁴²,
 A. Hasib⁴⁹, S. Hassani¹³⁸, S. Haug¹⁸, R. Hauser⁹³, L. Hauswald⁴⁷, L.B. Havener³⁸, M. Havranek¹³⁰,
 C.M. Hawkes¹⁹, R.J. Hawkins³², D. Hayakawa¹⁵⁹, D. Hayden⁹³, C.P. Hays¹²², J.M. Hays⁷⁹,
 H.S. Hayward⁷⁷, S.J. Haywood¹³³, S.J. Head¹⁹, T. Heck⁸⁶, V. Hedberg⁸⁴, L. Heelan⁸, K.K. Heidegger⁵¹,
 S. Heim⁴⁵, T. Heim¹⁶, B. Heinemann^{45,w}, J.J. Heinrich¹⁰², L. Heinrich¹¹², C. Heinz⁵⁵, J. Hejbal¹²⁹,
 L. Helary³², A. Held¹⁷¹, S. Hellman^{148a,148b}, C. Helsens³², R.C.W. Henderson⁷⁵, Y. Heng¹⁷⁶,
 S. Henkelmann¹⁷¹, A.M. Henriques Correia³², S. Henrot-Versille¹¹⁹, G.H. Herbert¹⁷, H. Herde²⁵,
 V. Herget¹⁷⁷, Y. Hernández Jiménez^{147c}, G. Herten⁵¹, R. Hertenberger¹⁰², L. Hervas³², T.C. Herwig¹²⁴,
 G.G. Hesketh⁸¹, N.P. Hesse^{163a}, J.W. Hetherly⁴³, S. Higashino⁶⁹, E. Higón-Rodríguez¹⁷⁰, E. Hill¹⁷²,
 J.C. Hill³⁰, K.H. Hiller⁴⁵, S.J. Hillier¹⁹, M. Hils⁴⁷, I. Hinchliffe¹⁶, M. Hirose⁵¹, D. Hirschbuehl¹⁷⁸,
 B. Hiti⁷⁸, O. Hladik¹²⁹, X. Hoad⁴⁹, J. Hobbs¹⁵⁰, N. Hod^{163a}, M.C. Hodgkinson¹⁴¹, P. Hodgson¹⁴¹,
 A. Hoecker³², M.R. Hoferkamp¹⁰⁷, F. Hoenic¹⁰², D. Hohn²³, T.R. Holmes³³, M. Homann⁴⁶,
 S. Honda¹⁶⁴, T. Honda⁶⁹, T.M. Hong¹²⁷, B.H. Hooberman¹⁶⁹, W.H. Hopkins¹¹⁸, Y. Horii¹⁰⁵,
 A.J. Horton¹⁴⁴, J.-Y. Hostachy⁵⁸, S. Hou¹⁵³, A. Hoummada^{137a}, J. Howarth⁴⁵, J. Hoya⁷⁴,
 M. Hrabovsky¹¹⁷, J. Hrdinka³², I. Hristova¹⁷, J. Hrivnac¹¹⁹, T. Hryn'ova⁵, A. Hrynevich⁹⁶, P.J. Hsu⁶³,
 S.-C. Hsu¹⁴⁰, Q. Hu^{36a}, S. Hu^{36c}, Y. Huang^{35a}, Z. Hubacek¹³⁰, F. Hubaut⁸⁸, F. Huegging²³,

T.B. Huffman¹²², E.W. Hughes³⁸, G. Hughes⁷⁵, M. Huhtinen³², P. Huo¹⁵⁰, N. Huseynov^{68,b}, J. Huston⁹³, J. Huth⁵⁹, G. Iacobucci⁵², G. Iakovidis²⁷, I. Ibragimov¹⁴³, L. Iconomidou-Fayard¹¹⁹, Z. Idrissi^{137e}, P. Iengo³², O. Igonkina^{109,x}, T. Iizawa¹⁷⁴, Y. Ikegami⁶⁹, M. Ikeno⁶⁹, Y. Ilchenko^{11,y}, D. Iliadis¹⁵⁶, N. Ilic¹⁴⁵, G. Introzzi^{123a,123b}, P. Ioannou^{9,*}, M. Iodice^{136a}, K. Iordanidou³⁸, V. Ippolito⁵⁹, M.F. Isacson¹⁶⁸, N. Ishijima¹²⁰, M. Ishino¹⁵⁷, M. Ishitsuka¹⁵⁹, C. Issever¹²², S. Istin^{20a}, F. Ito¹⁶⁴, J.M. Iturbe Ponce⁸⁷, R. Iuppa^{162a,162b}, H. Iwasaki⁶⁹, J.M. Izen⁴⁴, V. Izzo^{106a}, S. Jabbar³, P. Jackson¹, R.M. Jacobs²³, V. Jain², K.B. Jakobi⁸⁶, K. Jakobs⁵¹, S. Jakobsen⁶⁵, T. Jakoubek¹²⁹, D.O. Jamin¹¹⁶, D.K. Jana⁸², R. Jansky⁶⁵, J. Janssen²³, M. Janus⁵⁷, P.A. Janus^{41a}, G. Jarlskog⁸⁴, N. Javadov^{68,b}, T. Javůrek⁵¹, M. Javurkova⁵¹, F. Jeanneau¹³⁸, L. Jeanty¹⁶, J. Jejelava^{54a,z}, A. Jelinskas¹⁷³, P. Jenni^{51,aa}, C. Jeske¹⁷³, S. Jézéquel⁵, H. Ji¹⁷⁶, J. Jia¹⁵⁰, H. Jiang⁶⁷, Y. Jiang^{36a}, Z. Jiang¹⁴⁵, S. Jiggins⁸¹, J. Jimenez Pena¹⁷⁰, S. Jin^{35a}, A. Jinaru^{28b}, O. Jinnouchi¹⁵⁹, H. Jivan^{147c}, P. Johansson¹⁴¹, K.A. Johns⁷, C.A. Johnson⁶⁴, W.J. Johnson¹⁴⁰, K. Jon-And^{148a,148b}, R.W.L. Jones⁷⁵, S.D. Jones¹⁵¹, S. Jones⁷, T.J. Jones⁷⁷, J. Jongmanns^{60a}, P.M. Jorge^{128a,128b}, J. Jovicevic^{163a}, X. Ju¹⁷⁶, A. Juste Rozas^{13,u}, M.K. Köhler¹⁷⁵, A. Kaczmarek⁴², M. Kado¹¹⁹, H. Kagan¹¹³, M. Kagan¹⁴⁵, S.J. Kahn⁸⁸, T. Kaji¹⁷⁴, E. Kajomovitz⁴⁸, C.W. Kalderon⁸⁴, A. Kaluza⁸⁶, S. Kama⁴³, A. Kamenshchikov¹³², N. Kanaya¹⁵⁷, L. Kanjir⁷⁸, V.A. Kantserov¹⁰⁰, J. Kanzaki⁶⁹, B. Kaplan¹¹², L.S. Kaplan¹⁷⁶, D. Kar^{147c}, K. Karakostas¹⁰, N. Karastathis¹⁰, M.J. Kareem⁵⁷, E. Karentzos¹⁰, S.N. Karpov⁶⁸, Z.M. Karpova⁶⁸, K. Karthik¹¹², V. Kartvelishvili⁷⁵, A.N. Karyukhin¹³², K. Kasahara¹⁶⁴, L. Kashif¹⁷⁶, R.D. Kass¹¹³, A. Kastanas¹⁴⁹, Y. Kataoka¹⁵⁷, C. Kato¹⁵⁷, A. Katre⁵², J. Katzy⁴⁵, K. Kawade⁷⁰, K. Kawagoe⁷³, T. Kawamoto¹⁵⁷, G. Kawamura⁵⁷, E.F. Kay⁷⁷, V.F. Kazanin^{111,c}, R. Keeler¹⁷², R. Kehoe⁴³, J.S. Keller⁴⁵, J.J. Kempster⁸⁰, H. Keoshkerian¹⁶¹, O. Kepka¹²⁹, B.P. Kerševan⁷⁸, S. Kersten¹⁷⁸, R.A. Keyes⁹⁰, M. Khader¹⁶⁹, F. Khalil-zada¹², A. Khanov¹¹⁶, A.G. Kharlamov^{111,c}, T. Kharlamova^{111,c}, A. Khodinov¹⁶⁰, T.J. Khoo⁵², V. Khovanskiy^{99,*}, E. Khramov⁶⁸, J. Khubua^{54b,ab}, S. Kido⁷⁰, C.R. Kilby⁸⁰, H.Y. Kim⁸, S.H. Kim¹⁶⁴, Y.K. Kim³³, N. Kimura¹⁵⁶, O.M. Kind¹⁷, B.T. King⁷⁷, D. Kirchmeier⁴⁷, J. Kirk¹³³, A.E. Kiryunin¹⁰³, T. Kishimoto¹⁵⁷, D. Kisielewska^{41a}, K. Kiuchi¹⁶⁴, O. Kivernyk⁵, E. Kladiva^{146b}, T. Klapdor-Kleingrothaus⁵¹, M.H. Klein³⁸, M. Klein⁷⁷, U. Klein⁷⁷, K. Kleinknecht⁸⁶, P. Klimek¹¹⁰, A. Klimentov²⁷, R. Klingenberg⁴⁶, T. Klingl²³, T. Klioutchnikova³², E.-E. Kluge^{60a}, P. Kluit¹⁰⁹, S. Kluth¹⁰³, J. Knapik⁴², E. Kneringer⁶⁵, E.B.F.G. Knoop⁸⁸, A. Knue¹⁰³, A. Kobayashi¹⁵⁷, D. Kobayashi¹⁵⁹, T. Kobayashi¹⁵⁷, M. Kobel⁴⁷, M. Kocian¹⁴⁵, P. Kodys¹³¹, T. Koffas³¹, E. Koffeman¹⁰⁹, N.M. Köhler¹⁰³, T. Koi¹⁴⁵, M. Kolb^{60b}, I. Koletsou⁵, A.A. Komar^{98,*}, Y. Komori¹⁵⁷, T. Kondo⁶⁹, N. Kondrashova^{36c}, K. Köneke⁵¹, A.C. König¹⁰⁸, T. Kono^{69,ac}, R. Konoplich^{112,ad}, N. Konstantinidis⁸¹, R. Kopeliansky⁶⁴, S. Koperny^{41a}, A.K. Kopp⁵¹, K. Korcyl⁴², K. Kordas¹⁵⁶, A. Korn⁸¹, A.A. Korol^{111,c}, I. Korolkov¹³, E.V. Korolkova¹⁴¹, O. Kortner¹⁰³, S. Kortner¹⁰³, T. Kosek¹³¹, V.V. Kostyukhin²³, A. Kotwal⁴⁸, A. Koulouris¹⁰, A. Kourkumeli-Charalampidi^{123a,123b}, C. Kourkumelis⁹, E. Kourlitis¹⁴¹, V. Kouskoura²⁷, A.B. Kowalewska⁴², R. Kowalewski¹⁷², T.Z. Kowalski^{41a}, C. Kozakai¹⁵⁷, W. Kozanecki¹³⁸, A.S. Kozhin¹³², V.A. Kramarenko¹⁰¹, G. Kramberger⁷⁸, D. Krasnopevtsev¹⁰⁰, M.W. Krasny⁸³, A. Krasznahorkay³², D. Krauss¹⁰³, J.A. Kremer^{41a}, J. Kretschmar⁷⁷, K. Kreutzfeldt⁵⁵, P. Krieger¹⁶¹, K. Krizka³³, K. Kroeninger⁴⁶, H. Kroha¹⁰³, J. Kroll¹²⁹, J. Kroll¹²⁴, J. Kroseberg²³, J. Krstic¹⁴, U. Kruchonak⁶⁸, H. Krüger²³, N. Krumnack⁶⁷, M.C. Kruse⁴⁸, T. Kubota⁹¹, H. Kucuk⁸¹, S. Kuday^{4b}, J.T. Kuechler¹⁷⁸, S. Kuehn³², A. Kugel^{160c}, F. Kuger¹⁷⁷, T. Kuhl⁴⁵, V. Kukhtin⁶⁸, R. Kukla⁸⁸, Y. Kulchitsky⁹⁵, S. Kuleshov^{34b}, Y.P. Kulinich¹⁶⁹, M. Kuna^{134a,134b}, T. Kunigo⁷¹, A. Kupco¹²⁹, O. Kuprash¹⁵⁵, H. Kurashige⁷⁰, L.L. Kurchaninov^{163a}, Y.A. Kurochkin⁹⁵, M.G. Kurth^{35a}, V. Kus¹²⁹, E.S. Kuwertz¹⁷², M. Kuze¹⁵⁹, J. Kvita¹¹⁷, T. Kwan¹⁷², D. Kyriazopoulos¹⁴¹, A. La Rosa¹⁰³, J.L. La Rosa Navarro^{26d}, L. La Rotonda^{40a,40b}, C. Lacasta¹⁷⁰, F. Lacava^{134a,134b}, J. Lacey⁴⁵, H. Lacker¹⁷, D. Lacour⁸³, E. Ladygin⁶⁸, R. Lafaye⁵, B. Laforge⁸³, T. Lagouri¹⁷⁹, S. Lai⁵⁷, S. Lammers⁶⁴, W. Lamp¹⁷, E. Lançon²⁷, U. Landgraf⁵¹, M.P.J. Landon⁷⁹, M.C. Lanfermann⁵², V.S. Lang^{60a}, J.C. Lange¹³, R.J. Langenberg³², A.J. Lankford¹⁶⁶, F. Lanni²⁷, K. Lantzsck²³, A. Lanza^{123a}, A. Lapertosa^{53a,53b},

S. Laplace⁸³, J.F. Laporte¹³⁸, T. Lari^{94a}, F. Lasagni Manghi^{22a,22b}, M. Lassnig³², P. Laurelli⁵⁰,
 W. Lavrijsen¹⁶, A.T. Law¹³⁹, P. Laycock⁷⁷, T. Lazovich⁵⁹, M. Lazzaroni^{94a,94b}, B. Le⁹¹, O. Le Dortz⁸³,
 E. Le Guirriec⁸⁸, E.P. Le Quilleuc¹³⁸, M. LeBlanc¹⁷², T. LeCompte⁶, F. Ledroit-Guillon⁵⁸, C.A. Lee²⁷,
 G.R. Lee^{133,ae}, S.C. Lee¹⁵³, L. Lee⁵⁹, B. Lefebvre⁹⁰, G. Lefebvre⁸³, M. Lefebvre¹⁷², F. Legger¹⁰²,
 C. Leggett¹⁶, A. Lehan⁷⁷, G. Lehmann Miotto³², X. Lei⁷, W.A. Leight⁴⁵, M.A.L. Leite^{26d}, R. Leitner¹³¹,
 D. Lellouch¹⁷⁵, B. Lemmer⁵⁷, K.J.C. Leney⁸¹, T. Lenz²³, B. Lenzi³², R. Leone⁷, S. Leone^{126a,126b},
 C. Leonidopoulos⁴⁹, G. Lerner¹⁵¹, C. Leroy⁹⁷, A.A.J. Lesage¹³⁸, C.G. Lester³⁰, M. Levchenko¹²⁵,
 J. Levêque⁵, D. Levin⁹², L.J. Levinson¹⁷⁵, M. Levy¹⁹, D. Lewis⁷⁹, B. Li^{36a,af}, C. Li^{36a}, H. Li¹⁵⁰,
 L. Li^{36c}, Q. Li^{35a}, S. Li⁴⁸, X. Li^{36c}, Y. Li¹⁴³, Z. Liang^{35a}, B. Liberti^{135a}, A. Liblong¹⁶¹, K. Lie^{62c},
 J. Liebal²³, W. Liebig¹⁵, A. Limosani¹⁵², S.C. Lin^{153,ag}, T.H. Lin⁸⁶, B.E. Lindquist¹⁵⁰, A.E. Lioni⁵²,
 E. Lipeles¹²⁴, A. Lipniacka¹⁵, M. Lisovyi^{60b}, T.M. Liss¹⁶⁹, A. Lister¹⁷¹, A.M. Litke¹³⁹, B. Liu^{153,ah},
 H. Liu⁹², H. Liu²⁷, J.K.K. Liu¹²², J. Liu^{36b}, J.B. Liu^{36a}, K. Liu⁸⁸, L. Liu¹⁶⁹, M. Liu^{36a}, Y.L. Liu^{36a},
 Y. Liu^{36a}, M. Livan^{123a,123b}, A. Lleres⁵⁸, J. Llorente Merino^{35a}, S.L. Lloyd⁷⁹, C.Y. Lo^{62b},
 F. Lo Sterzo¹⁵³, E.M. Lobodzinska⁴⁵, P. Loch⁷, F.K. Loebinger⁸⁷, K.M. Loew²⁵, A. Loginov^{179,*},
 T. Lohse¹⁷, K. Lohwasser⁴⁵, M. Lokajicek¹²⁹, B.A. Long²⁴, J.D. Long¹⁶⁹, R.E. Long⁷⁵, L. Longo^{76a,76b},
 K.A. Looper¹¹³, J.A. Lopez^{34b}, D. Lopez Mateos⁵⁹, I. Lopez Paz¹³, A. Lopez Solis⁸³, J. Lorenz¹⁰²,
 N. Lorenzo Martinez⁵, M. Losada²¹, P.J. Lösel¹⁰², X. Lou^{35a}, A. Lounis¹¹⁹, J. Love⁶, P.A. Love⁷⁵,
 H. Lu^{62a}, N. Lu⁹², Y.J. Lu⁶³, H.J. Lubatti¹⁴⁰, C. Luci^{134a,134b}, A. Lucotte⁵⁸, C. Luedtke⁵¹, F. Luehring⁶⁴,
 W. Lukas⁶⁵, L. Luminari^{134a}, O. Lundberg^{148a,148b}, B. Lund-Jensen¹⁴⁹, P.M. Luzi⁸³, D. Lynn²⁷,
 R. Lysak¹²⁹, E. Lytken⁸⁴, V. Lyubushkin⁶⁸, H. Ma²⁷, L.L. Ma^{36b}, Y. Ma^{36b}, G. Maccarrone⁵⁰,
 A. Macchiolo¹⁰³, C.M. Macdonald¹⁴¹, B. Maček⁷⁸, J. Machado Miguens^{124,128b}, D. Madaffari⁸⁸,
 R. Madar³⁷, H.J. Maddocks¹⁶⁸, W.F. Mader⁴⁷, A. Madsen⁴⁵, J. Maeda⁷⁰, S. Maeland¹⁵, T. Maeno²⁷,
 A.S. Maevskiy¹⁰¹, E. Magradze⁵⁷, J. Mahlstedt¹⁰⁹, C. Maiani¹¹⁹, C. Maidantchik^{26a}, A.A. Maier¹⁰³,
 T. Maier¹⁰², A. Maio^{128a,128b,128d}, S. Majewski¹¹⁸, Y. Makida⁶⁹, N. Makovec¹¹⁹, B. Malaescu⁸³,
 Pa. Malecki⁴², V.P. Maleev¹²⁵, F. Malek⁵⁸, U. Mallik⁶⁶, D. Malon⁶, C. Malone³⁰, S. Maltezos¹⁰,
 S. Malyukov³², J. Mamuzic¹⁷⁰, G. Mancini⁵⁰, L. Mandelli^{94a}, I. Mandić⁷⁸, J. Maneira^{128a,128b},
 L. Manhaes de Andrade Filho^{26b}, J. Manjarres Ramos⁴⁷, A. Mann¹⁰², A. Manousos³², B. Mansoulié¹³⁸,
 J.D. Mansour^{35a}, R. Mantifel⁹⁰, M. Mantoani⁵⁷, S. Manzoni^{94a,94b}, L. Mapelli³², G. Marceca²⁹,
 L. March⁵², L. Marchese¹²², G. Marchiori⁸³, M. Marcisovsky¹²⁹, M. Marjanovic³⁷, D.E. Marley⁹²,
 F. Marroquim^{26a}, S.P. Marsden⁸⁷, Z. Marshall¹⁶, M.U.F. Martensson¹⁶⁸, S. Marti-Garcia¹⁷⁰,
 C.B. Martin¹¹³, T.A. Martin¹⁷³, V.J. Martin⁴⁹, B. Martin dit Latour¹⁵, M. Martinez^{13,u},
 V.I. Martinez Outschoorn¹⁶⁹, S. Martin-Haugh¹³³, V.S. Martoiu^{28b}, A.C. Martyniuk⁸¹, A. Marzin³²,
 L. Masetti⁸⁶, T. Mashimo¹⁵⁷, R. Mashinistov⁹⁸, J. Masik⁸⁷, A.L. Maslennikov^{111,c}, L. Massa^{135a,135b},
 P. Mastrandrea⁵, A. Mastroberardino^{40a,40b}, T. Masubuchi¹⁵⁷, P. Mättig¹⁷⁸, J. Maurer^{28b}, S.J. Maxfield⁷⁷,
 D.A. Maximov^{111,c}, R. Mazini¹⁵³, I. Maznas¹⁵⁶, S.M. Mazza^{94a,94b}, N.C. Mc Fadden¹⁰⁷,
 G. Mc Goldrick¹⁶¹, S.P. Mc Kee⁹², A. McCarn⁹², R.L. McCarthy¹⁵⁰, T.G. McCarthy¹⁰³,
 L.I. McClymont⁸¹, E.F. McDonald⁹¹, J.A. McFayden⁸¹, G. Mchedlidge⁵⁷, S.J. McMahon¹³³,
 P.C. McNamara⁹¹, R.A. McPherson^{172,o}, S. Meehan¹⁴⁰, T.J. Megy⁵¹, S. Mehlhase¹⁰², A. Mehta⁷⁷,
 T. Meideck⁵⁸, K. Meier^{60a}, B. Meirose⁴⁴, D. Melini^{170,ai}, B.R. Mellado Garcia^{147c}, J.D. Mellenthin⁵⁷,
 M. Melo^{146a}, F. Meloni¹⁸, S.B. Menary⁸⁷, L. Meng⁷⁷, X.T. Meng⁹², A. Mengarelli^{22a,22b}, S. Menke¹⁰³,
 E. Meoni^{40a,40b}, S. Mergelmeyer¹⁷, P. Mermod⁵², L. Merola^{106a,106b}, C. Meroni^{94a}, F.S. Merritt³³,
 A. Messina^{134a,134b}, J. Metcalfe⁶, A.S. Mete¹⁶⁶, C. Meyer¹²⁴, J-P. Meyer¹³⁸, J. Meyer¹⁰⁹,
 H. Meyer Zu Theenhausen^{60a}, F. Miano¹⁵¹, R.P. Middleton¹³³, S. Miglioranzi^{53a,53b}, L. Mijović⁴⁹,
 G. Mikenberg¹⁷⁵, M. Mikesikova¹²⁹, M. Mikuž⁷⁸, M. Milesi⁹¹, A. Milic¹⁶¹, D.W. Miller³³, C. Mills⁴⁹,
 A. Milov¹⁷⁵, D.A. Milstead^{148a,148b}, A.A. Minaenko¹³², Y. Minami¹⁵⁷, I.A. Minashvili⁶⁸, A.I. Mincer¹¹²,
 B. Mindur^{41a}, M. Mineev⁶⁸, Y. Minegishi¹⁵⁷, Y. Ming¹⁷⁶, L.M. Mir¹³, K.P. Mistry¹²⁴, T. Mitani¹⁷⁴,
 J. Mitrevski¹⁰², V.A. Mitsou¹⁷⁰, A. Miucci¹⁸, P.S. Miyagawa¹⁴¹, A. Mizukami⁶⁹, J.U. Mjörnmark⁸⁴,

T. Mkrtchyan¹⁸⁰, M. Mlynarikova¹³¹, T. Moa^{148a,148b}, K. Mochizuki⁹⁷, P. Mogg⁵¹, S. Mohapatra³⁸, S. Molander^{148a,148b}, R. Moles-Valls²³, R. Monden⁷¹, M.C. Mondragon⁹³, K. Mönig⁴⁵, J. Monk³⁹, E. Monnier⁸⁸, A. Montalbano¹⁵⁰, J. Montejo Berlingen³², F. Monticelli⁷⁴, S. Monzani^{94a,94b}, R.W. Moore³, N. Morange¹¹⁹, D. Moreno²¹, M. Moreno Llácer⁵⁷, P. Morettini^{53a}, S. Morgenstern³², D. Mori¹⁴⁴, T. Mori¹⁵⁷, M. Morii⁵⁹, M. Morinaga¹⁵⁷, V. Morisbak¹²¹, A.K. Morley¹⁵², G. Mornacchi³², J.D. Morris⁷⁹, L. Morvaj¹⁵⁰, P. Moschovakos¹⁰, M. Mosidze^{54b}, H.J. Moss¹⁴¹, J. Moss^{145,aj}, K. Motohashi¹⁵⁹, R. Mount¹⁴⁵, E. Mountricha²⁷, E.J.W. Moyse⁸⁹, S. Muanza⁸⁸, R.D. Mudd¹⁹, F. Mueller¹⁰³, J. Mueller¹²⁷, R.S.P. Mueller¹⁰², D. Muenstermann⁷⁵, P. Mullen⁵⁶, G.A. Mullier¹⁸, F.J. Munoz Sanchez⁸⁷, W.J. Murray^{173,133}, H. Musheghyan¹⁸¹, M. Muškinja⁷⁸, A.G. Myagkov^{132,ak}, M. Myska¹³⁰, B.P. Nachman¹⁶, O. Nackenhorst⁵², K. Nagai¹²², R. Nagai^{69,ac}, K. Nagano⁶⁹, Y. Nagasaka⁶¹, K. Nagata¹⁶⁴, M. Nagel⁵¹, E. Nagy⁸⁸, A.M. Nairz³², Y. Nakahama¹⁰⁵, K. Nakamura⁶⁹, T. Nakamura¹⁵⁷, I. Nakano¹¹⁴, R.F. Naranjo Garcia⁴⁵, R. Narayan¹¹, D.I. Narrias Villar^{60a}, I. Naryshkin¹²⁵, T. Naumann⁴⁵, G. Navarro²¹, R. Nayyar⁷, H.A. Neal⁹², P.Yu. Nechaeva⁹⁸, T.J. Neep¹³⁸, A. Negri^{123a,123b}, M. Negrini^{22a}, S. Nektarijevic¹⁰⁸, C. Nellist¹¹⁹, A. Nelson¹⁶⁶, M.E. Nelson¹²², S. Nemecek¹²⁹, P. Nemethy¹¹², M. Nessi^{32,al}, M.S. Neubauer¹⁶⁹, M. Neumann¹⁷⁸, P.R. Newman¹⁹, T.Y. Ng^{62c}, T. Nguyen Manh⁹⁷, R.B. Nickerson¹²², R. Nicolaidou¹³⁸, J. Nielsen¹³⁹, V. Nikolaenko^{132,ak}, I. Nikolic-Audit⁸³, K. Nikolopoulos¹⁹, J.K. Nilsen¹²¹, P. Nilsson²⁷, Y. Ninomiya¹⁵⁷, A. Nisati^{134a}, N. Nishu^{35c}, R. Nisius¹⁰³, T. Nobe¹⁵⁷, Y. Noguchi⁷¹, M. Nomachi¹²⁰, I. Nomidis³¹, M.A. Nomura²⁷, T. Nooney⁷⁹, M. Nordberg³², N. Norjoharuddeen¹²², O. Novgorodova⁴⁷, S. Nowak¹⁰³, M. Nozaki⁶⁹, L. Nozka¹¹⁷, K. Ntekas¹⁶⁶, E. Nurse⁸¹, F. Nuti⁹¹, K. O'connor²⁵, D.C. O'Neil¹⁴⁴, A.A. O'Rourke⁴⁵, V. O'Shea⁵⁶, F.G. Oakham^{31,d}, H. Oberlack¹⁰³, T. Obermann²³, J. Ocariz⁸³, A. Ochi⁷⁰, I. Ochoa³⁸, J.P. Ochoa-Ricoux^{34a}, S. Oda⁷³, S. Odaka⁶⁹, H. Ogren⁶⁴, A. Oh⁸⁷, S.H. Oh⁴⁸, C.C. Ohm¹⁶, H. Ohman¹⁶⁸, H. Oide^{53a,53b}, H. Okawa¹⁶⁴, Y. Okumura¹⁵⁷, T. Okuyama⁶⁹, A. Olariu^{28b}, L.F. Oleiro Seabra^{128a}, S.A. Olivares Pino⁴⁹, D. Oliveira Damazio²⁷, A. Olszewski⁴², J. Olszowska⁴², A. Onofre^{128a,128e}, K. Onogi¹⁰⁵, P.U.E. Onyisi^{11,y}, M.J. Oreglia³³, Y. Oren¹⁵⁵, D. Orestano^{136a,136b}, N. Orlando^{62b}, R.S. Orr¹⁶¹, B. Osculati^{53a,53b,*}, R. Ospanov^{36a}, G. Otero y Garzon²⁹, H. Otono⁷³, M. Ouchrif^{137d}, F. Ould-Saada¹²¹, A. Ouraou¹³⁸, K.P. Oussoren¹⁰⁹, Q. Ouyang^{35a}, M. Owen⁵⁶, R.E. Owen¹⁹, V.E. Ozcan^{20a}, N. Ozturk⁸, K. Pachal¹⁴⁴, A. Pacheco Pages¹³, L. Pacheco Rodriguez¹³⁸, C. Padilla Aranda¹³, S. Pagan Griso¹⁶, M. Paganini¹⁷⁹, F. Paige²⁷, G. Palacino⁶⁴, S. Palazzo^{40a,40b}, S. Palestini³², M. Palka^{41b}, D. Pallin³⁷, E.St. Panagiotopoulou¹⁰, I. Panagoulas¹⁰, C.E. Pandini⁸³, J.G. Panduro Vazquez⁸⁰, P. Pani³², S. Panitkin²⁷, D. Pantea^{28b}, L. Paolozzi⁵², Th.D. Papadopoulou¹⁰, K. Papageorgiou⁹, A. Paramonov⁶, D. Paredes Hernandez¹⁷⁹, A.J. Parker⁷⁵, M.A. Parker³⁰, K.A. Parker⁴⁵, F. Parodi^{53a,53b}, J.A. Parsons³⁸, U. Parzefall⁵¹, V.R. Pascuzzi¹⁶¹, J.M. Pasner¹³⁹, E. Pasqualucci^{134a}, S. Passaggio^{53a}, Fr. Pastore⁸⁰, S. Pataraiia¹⁷⁸, J.R. Pater⁸⁷, T. Pauly³², B. Pearson¹⁰³, S. Pedraza Lopez¹⁷⁰, R. Pedro^{128a,128b}, S.V. Peleganchuk^{111,c}, O. Penc¹²⁹, C. Peng^{35a}, H. Peng^{36a}, J. Penwell⁶⁴, B.S. Peralva^{26b}, M.M. Perego¹³⁸, D.V. Perepelitsa²⁷, L. Perini^{94a,94b}, H. Pernegger³², S. Perrella^{106a,106b}, R. Peschke⁴⁵, V.D. Peshekhonov^{68,*}, K. Peters⁴⁵, R.F.Y. Peters⁸⁷, B.A. Petersen³², T.C. Petersen³⁹, E. Petit⁵⁸, A. Petridis¹, C. Petridou¹⁵⁶, P. Petroff¹¹⁹, E. Petrolo^{134a}, M. Petrov¹²², F. Petrucci^{136a,136b}, N.E. Pettersson⁸⁹, A. Peyaud¹³⁸, R. Pezoa^{34b}, F.H. Phillips⁹³, P.W. Phillips¹³³, G. Piacquadio¹⁵⁰, E. Pianori¹⁷³, A. Picazio⁸⁹, E. Piccaro⁷⁹, M.A. Pickering¹²², R. Piegai²⁹, J.E. Pilcher³³, A.D. Pilkington⁸⁷, A.W.J. Pin⁸⁷, M. Pinamonti^{135a,135b}, J.L. Pinfold³, H. Pirumov⁴⁵, M. Pitt¹⁷⁵, L. Plazak^{146a}, M.-A. Pleier²⁷, V. Pleskot⁸⁶, E. Plotnikova⁶⁸, D. Pluth⁶⁷, P. Podberezko¹¹¹, R. Poettgen^{148a,148b}, R. Poggi^{123a,123b}, L. Poggioli¹¹⁹, D. Pohl²³, G. Polesello^{123a}, A. Poley⁴⁵, A. Policicchio^{40a,40b}, R. Polifka³², A. Polini^{22a}, C.S. Pollard⁵⁶, V. Polychronakos²⁷, K. Pommès³², D. Ponomarenko¹⁰⁰, L. Pontecorvo^{134a}, B.G. Pope⁹³, G.A. Popeneciu^{28d}, A. Poppleton³², S. Pospisil¹³⁰, K. Potamianos¹⁶, I.N. Potrap⁶⁸, C.J. Potter³⁰, G. Poulard³², T. Poulsen⁸⁴, J. Poveda³², M.E. Pozo Astigarraga³², P. Pralavorio⁸⁸, A. Pranko¹⁶, S. Prell⁶⁷, D. Price⁸⁷, L.E. Price⁶,

M. Primavera^{76a}, S. Prince⁹⁰, N. Proklova¹⁰⁰, K. Prokofiev^{62c}, F. Prokoshin^{34b}, S. Protopopescu²⁷,
J. Proudfoot⁶, M. Przybycien^{41a}, A. Puri¹⁶⁹, P. Puzo¹¹⁹, J. Qian⁹², G. Qin⁵⁶, Y. Qin⁸⁷, A. Quadt⁵⁷,
M. Queitsch-Maitland⁴⁵, D. Quilty⁵⁶, S. Raddum¹²¹, V. Radeka²⁷, V. Radescu¹²²,
S.K. Radhakrishnan¹⁵⁰, P. Radloff¹¹⁸, P. Rados⁹¹, F. Ragusa^{94a,94b}, G. Rahal¹⁸², J.A. Raine⁸⁷,
S. Rajagopalan²⁷, C. Rangel-Smith¹⁶⁸, T. Rashid¹¹⁹, S. Raspopov⁵, M.G. Ratti^{94a,94b}, D.M. Rauch⁴⁵,
F. Rauscher¹⁰², S. Rave⁸⁶, I. Ravinovich¹⁷⁵, J.H. Rawling⁸⁷, M. Raymond³², A.L. Read¹²¹,
N.P. Readioff⁵⁸, M. Reale^{76a,76b}, D.M. Rebuffi^{123a,123b}, A. Redelbach¹⁷⁷, G. Redlinger²⁷, R. Reece¹³⁹,
R.G. Reed^{147c}, K. Reeves⁴⁴, L. Rehnisch¹⁷, J. Reichert¹²⁴, A. Reiss⁸⁶, C. Rembser³², H. Ren^{35a},
M. Rescigno^{134a}, S. Resconi^{94a}, E.D. Resseguie¹²⁴, S. Rettie¹⁷¹, E. Reynolds¹⁹, O.L. Rezanova^{111,c},
P. Reznicek¹³¹, R. Rezvani⁹⁷, R. Richter¹⁰³, S. Richter⁸¹, E. Richter-Was^{41b}, O. Ricken²³, M. Ridel⁸³,
P. Rieck¹⁰³, C.J. Riegel¹⁷⁸, J. Rieger⁵⁷, O. Rifki¹¹⁵, M. Rijssenbeek¹⁵⁰, A. Rimoldi^{123a,123b},
M. Rimoldi¹⁸, L. Rinaldi^{22a}, G. Ripellino¹⁴⁹, B. Ristic⁵², E. Ritsch³², I. Riu¹³, F. Rizatdinova¹¹⁶,
E. Rizvi⁷⁹, C. Rizzi¹³, R.T. Roberts⁸⁷, S.H. Robertson^{90,o}, A. Robichaud-Veronneau⁹⁰, D. Robinson³⁰,
J.E.M. Robinson⁴⁵, A. Robson⁵⁶, E. Rocco⁸⁶, C. Roda^{126a,126b}, Y. Rodina^{88,am}, S. Rodriguez Bosca¹⁷⁰,
A. Rodriguez Perez¹³, D. Rodriguez Rodriguez¹⁷⁰, S. Roe³², C.S. Rogan⁵⁹, O. Røhne¹²¹, J. Roloff⁵⁹,
A. Romaniouk¹⁰⁰, M. Romano^{22a,22b}, S.M. Romano Saez³⁷, E. Romero Adam¹⁷⁰, N. Rompotis⁷⁷,
M. Ronzani⁵¹, L. Roos⁸³, S. Rosati^{134a}, K. Rosbach⁵¹, P. Rose¹³⁹, N.-A. Rosien⁵⁷, E. Rossi^{106a,106b},
L.P. Rossi^{53a}, J.H.N. Rosten³⁰, R. Rosten¹⁴⁰, M. Rotaru^{28b}, I. Roth¹⁷⁵, J. Rothberg¹⁴⁰, D. Rousseau¹¹⁹,
A. Rozanov⁸⁸, Y. Rozen¹⁵⁴, X. Ruan^{147c}, F. Rubbo¹⁴⁵, F. Rühr⁵¹, A. Ruiz-Martinez³¹, Z. Rurikova⁵¹,
N.A. Rusakovich⁶⁸, H.L. Russell⁹⁰, J.P. Rutherford⁷, N. Ruthmann³², Y.F. Ryabov¹²⁵, M. Rybar¹⁶⁹,
G. Rybkin¹¹⁹, S. Ryu⁶, A. Ryzhov¹³², G.F. Rzehorz⁵⁷, A.F. Saavedra¹⁵², G. Sabato¹⁰⁹, S. Sacerdoti²⁹,
H.F.-W. Sadrozinski¹³⁹, R. Sadykov⁶⁸, F. Safai Tehrani^{134a}, P. Saha¹¹⁰, M. Sahinsoy^{60a}, M. Saimpert⁴⁵,
M. Saito¹⁵⁷, T. Saito¹⁵⁷, H. Sakamoto¹⁵⁷, Y. Sakurai¹⁷⁴, G. Salamanna^{136a,136b}, J.E. Salazar Loyola^{34b},
D. Salek¹⁰⁹, P.H. Sales De Bruin¹⁶⁸, D. Salihagic¹⁰³, A. Salnikov¹⁴⁵, J. Salt¹⁷⁰, D. Salvatore^{40a,40b},
F. Salvatore¹⁵¹, A. Salvucci^{62a,62b,62c}, A. Salzburger³², D. Sammel⁵¹, D. Sampsonidis¹⁵⁶,
D. Sampsonidou¹⁵⁶, J. Sánchez¹⁷⁰, V. Sanchez Martinez¹⁷⁰, A. Sanchez Pineda^{167a,167c}, H. Sandaker¹²¹,
R.L. Sandbach⁷⁹, C.O. Sander⁴⁵, M. Sandhoff¹⁷⁸, C. Sandoval²¹, D.P.C. Sankey¹³³, M. Sannino^{53a,53b},
A. Sansoni⁵⁰, C. Santoni³⁷, R. Santonico^{135a,135b}, H. Santos^{128a}, I. Santoyo Castillo¹⁵¹, A. Saprnov⁶⁸,
J.G. Saraiva^{128a,128d}, B. Sarrazin²³, O. Sasaki⁶⁹, K. Sato¹⁶⁴, E. Sauvan⁵, G. Savage⁸⁰, P. Savard^{161,d},
N. Savic¹⁰³, C. Sawyer¹³³, L. Sawyer^{82,t}, J. Saxon³³, C. Sbarra^{22a}, A. Sbrizzi^{22a,22b}, T. Scanlon⁸¹,
D.A. Scannicchio¹⁶⁶, M. Scarcella¹⁵², V. Scarfone^{40a,40b}, J. Schaarschmidt¹⁴⁰, P. Schacht¹⁰³,
B.M. Schachtner¹⁰², D. Schaefer³², L. Schaefer¹²⁴, R. Schaefer⁴⁵, J. Schaeffer⁸⁶, S. Schaepe²³,
S. Schaezel^{60b}, U. Schäfer⁸⁶, A.C. Schaffer¹¹⁹, D. Schaile¹⁰², R.D. Schamberger¹⁵⁰, V. Scharf^{60a},
V.A. Schegelsky¹²⁵, D. Scheirich¹³¹, M. Schernau¹⁶⁶, C. Schiavi^{53a,53b}, S. Schier¹³⁹, L.K. Schildgen²³,
C. Schillo⁵¹, M. Schioppa^{40a,40b}, S. Schlenker³², K.R. Schmidt-Sommerfeld¹⁰³, K. Schmieden³²,
C. Schmitt⁸⁶, S. Schmitt⁴⁵, S. Schmitz⁸⁶, U. Schnoor⁵¹, L. Schoeffel¹³⁸, A. Schoening^{60b},
B.D. Schoenrock⁹³, E. Schopf²³, M. Schott⁸⁶, J.F.P. Schouwenberg¹⁰⁸, J. Schovancova¹⁸¹,
S. Schramm⁵², N. Schuh⁸⁶, A. Schulte⁸⁶, M.J. Schultens²³, H.-C. Schultz-Coulon^{60a}, H. Schulz¹⁷,
M. Schumacher⁵¹, B.A. Schumm¹³⁹, Ph. Schune¹³⁸, A. Schwartzman¹⁴⁵, T.A. Schwarz⁹²,
H. Schweiger⁸⁷, Ph. Schwemling¹³⁸, R. Schwienhorst⁹³, J. Schwindling¹³⁸, A. Sciandra²³, G. Sciolla²⁵,
F. Scuri^{126a,126b}, F. Scutti⁹¹, J. Searcy⁹², P. Seema²³, S.C. Seidel¹⁰⁷, A. Seiden¹³⁹, J.M. Seixas^{26a},
G. Sekhniadze^{106a}, K. Sekhon⁹², S.J. Sekula⁴³, N. Semprini-Cesari^{22a,22b}, S. Senkin³⁷, C. Serfon¹²¹,
L. Serin¹¹⁹, L. Serkin^{167a,167b}, M. Sessa^{136a,136b}, R. Seuster¹⁷², H. Severini¹¹⁵, T. Sfiligoj⁷⁸, F. Sforza³²,
A. Sfyrla⁵², E. Shabalina⁵⁷, N.W. Shaikh^{148a,148b}, L.Y. Shan^{35a}, R. Shang¹⁶⁹, J.T. Shank²⁴, M. Shapiro¹⁶,
P.B. Shatalov⁹⁹, K. Shaw^{167a,167b}, S.M. Shaw⁸⁷, A. Shcherbakova^{148a,148b}, C.Y. Shehu¹⁵¹, Y. Shen¹¹⁵,
P. Sherwood⁸¹, L. Shi^{153,an}, S. Shimizu⁷⁰, C.O. Shimmin¹⁷⁹, M. Shimojima¹⁰⁴, I.P.J. Shipsey¹²²,
S. Shirabe⁷³, M. Shiyakova^{68,ao}, J. Shlomi¹⁷⁵, A. Shmeleva⁹⁸, D. Shoaleh Saadi⁹⁷, M.J. Shochet³³,

S. Shojaii^{94a}, D.R. Shope¹¹⁵, S. Shrestha¹¹³, E. Shulga¹⁰⁰, M.A. Shupe⁷, P. Sicho¹²⁹, A.M. Sickles¹⁶⁹,
 P.E. Sidebo¹⁴⁹, E. Sideras Haddad^{147c}, O. Sidiropoulou¹⁷⁷, A. Sidoti^{22a,22b}, F. Siegert⁴⁷, Dj. Sijacki¹⁴,
 J. Silva^{128a,128d}, S.B. Silverstein^{148a}, V. Simak¹³⁰, Lj. Simic¹⁴, S. Simion¹¹⁹, E. Simioni⁸⁶,
 B. Simmons⁸¹, M. Simon⁸⁶, P. Sinervo¹⁶¹, N.B. Sinev¹¹⁸, M. Sioli^{22a,22b}, G. Siragusa¹⁷⁷, I. Siral⁹²,
 S.Yu. Sivoklov¹⁰¹, J. Sjölin^{148a,148b}, M.B. Skinner⁷⁵, P. Skubic¹¹⁵, M. Slater¹⁹, T. Slavicek¹³⁰,
 M. Slawinska⁴², K. Sliwa¹⁶⁵, R. Slovak¹³¹, V. Smakhtin¹⁷⁵, B.H. Smart⁵, J. Smiesko^{146a}, N. Smirnov¹⁰⁰,
 S.Yu. Smirnov¹⁰⁰, Y. Smirnov¹⁰⁰, L.N. Smirnova^{101.ap}, O. Smirnova⁸⁴, J.W. Smith⁵⁷, M.N.K. Smith³⁸,
 R.W. Smith³⁸, M. Smizanska⁷⁵, K. Smolek¹³⁰, A.A. Snesarev⁹⁸, I.M. Snyder¹¹⁸, S. Snyder²⁷,
 R. Sobie^{172.o}, F. Socher⁴⁷, A. Soffer¹⁵⁵, D.A. Soh¹⁵³, G. Sokhranyi⁷⁸, C.A. Solans Sanchez³²,
 M. Solar¹³⁰, E.Yu. Soldatov¹⁰⁰, U. Soldevila¹⁷⁰, A.A. Solodkov¹³², A. Soloshenko⁶⁸,
 O.V. Solovyanov¹³², V. Solovyev¹²⁵, P. Sommer⁵¹, H. Son¹⁶⁵, H.Y. Song^{36a,aq}, A. Sopczak¹³⁰,
 D. Sosa^{60b}, C.L. Sotiropoulou^{126a,126b}, R. Soualah^{167a,167c}, A.M. Soukharev^{111.c}, D. South⁴⁵,
 B.C. Sowden⁸⁰, S. Spagnolo^{76a,76b}, M. Spalla^{126a,126b}, M. Spangenberg¹⁷³, F. Spanò⁸⁰, D. Sperlich¹⁷,
 F. Spettel¹⁰³, T.M. Spieker^{60a}, R. Spighi^{22a}, G. Spigo³², L.A. Spiller⁹¹, M. Spousta¹³¹,
 R.D. St. Denis^{56,*}, A. Stabile^{94a}, R. Stamen^{60a}, S. Stamm¹⁷, E. Stanecka⁴², R.W. Stanek⁶,
 C. Stanescu^{136a}, M.M. Stanitzki⁴⁵, S. Stapnes¹²¹, E.A. Starchenko¹³², G.H. Stark³³, J. Stark⁵⁸,
 S.H. Stark³⁹, P. Staroba¹²⁹, P. Starovoitov^{60a}, S. Stärz³², R. Staszewski⁴², P. Steinberg²⁷, B. Stelzer¹⁴⁴,
 H.J. Stelzer³², O. Stelzer-Chilton^{163a}, H. Stenzel⁵⁵, G.A. Stewart⁵⁶, M.C. Stockton¹¹⁸, M. Stoebe⁹⁰,
 G. Stoicea^{28b}, P. Stolte⁵⁷, S. Stonjek¹⁰³, A.R. Stradling⁸, A. Straessner⁴⁷, M.E. Stramaglia¹⁸,
 J. Strandberg¹⁴⁹, S. Strandberg^{148a,148b}, A. Strandlie¹²¹, M. Strauss¹¹⁵, P. Strizenc^{146b}, R. Ströhmer¹⁷⁷,
 D.M. Strom¹¹⁸, R. Stroynowski⁴³, A. Strubig¹⁰⁸, S.A. Stucci²⁷, B. Stugu¹⁵, N.A. Styles⁴⁵, D. Su¹⁴⁵,
 J. Su¹²⁷, S. Suchek^{60a}, Y. Sugaya¹²⁰, M. Suk¹³⁰, V.V. Sulin⁹⁸, S. Sultansoy^{4c}, T. Sumida⁷¹, S. Sun⁵⁹,
 X. Sun³, K. Suruliz¹⁵¹, C.J.E. Suster¹⁵², M.R. Sutton¹⁵¹, S. Suzuki⁶⁹, M. Svatos¹²⁹, M. Swiatlowski³³,
 S.P. Swift², I. Sykora^{146a}, T. Sykora¹³¹, D. Ta⁵¹, K. Tackmann⁴⁵, J. Taenzer¹⁵⁵, A. Taffard¹⁶⁶,
 R. Tafirout^{163a}, N. Taiblum¹⁵⁵, H. Takai²⁷, R. Takashima⁷², E.H. Takasugi¹⁰³, T. Takeshita¹⁴²,
 Y. Takubo⁶⁹, M. Talby⁸⁸, A.A. Talyshev^{111.c}, J. Tanaka¹⁵⁷, M. Tanaka¹⁵⁹, R. Tanaka¹¹⁹, S. Tanaka⁶⁹,
 R. Tanioka⁷⁰, B.B. Tannenwald¹¹³, S. Tapia Araya^{34b}, S. Tapprogge⁸⁶, S. Tarem¹⁵⁴, G.F. Tartarelli^{94a},
 P. Tas¹³¹, M. Tasevsky¹²⁹, T. Tashiro⁷¹, E. Tassi^{40a,40b}, A. Tavares Delgado^{128a,128b}, Y. Tayalati^{137e},
 A.C. Taylor¹⁰⁷, G.N. Taylor⁹¹, P.T.E. Taylor⁹¹, W. Taylor^{163b}, P. Teixeira-Dias⁸⁰, D. Temple¹⁴⁴,
 H. Ten Kate³², P.K. Teng¹⁵³, J.J. Teoh¹²⁰, F. Tepe¹⁷⁸, S. Terada⁶⁹, K. Terashi¹⁵⁷, J. Terron⁸⁵, S. Terzo¹³,
 M. Testa⁵⁰, R.J. Teuscher^{161.o}, T. Theveneaux-Pelzer⁸⁸, J.P. Thomas¹⁹, J. Thomas-Wilsker⁸⁰,
 P.D. Thompson¹⁹, A.S. Thompson⁵⁶, L.A. Thomsen¹⁷⁹, E. Thomson¹²⁴, M.J. Tibbetts¹⁶,
 R.E. Ticse Torres⁸⁸, V.O. Tikhomirov^{98.ar}, Yu.A. Tikhonov^{111.c}, S. Timoshenko¹⁰⁰, P. Tipton¹⁷⁹,
 S. Tisserant⁸⁸, K. Todome¹⁵⁹, S. Todorova-Nova⁵, J. Tojo⁷³, S. Tokár^{146a}, K. Tokushuku⁶⁹, E. Tolley⁵⁹,
 L. Tomlinson⁸⁷, M. Tomoto¹⁰⁵, L. Tompkins^{145.as}, K. Toms¹⁰⁷, B. Tong⁵⁹, P. Tornambe⁵¹,
 E. Torrence¹¹⁸, H. Torres¹⁴⁴, E. Torró Pastor¹⁴⁰, J. Toth^{88.at}, F. Touchard⁸⁸, D.R. Tovey¹⁴¹,
 C.J. Treado¹¹², T. Trefzger¹⁷⁷, F. Tresoldi¹⁵¹, A. Tricoli²⁷, I.M. Trigger^{163a}, S. Trincaz-Duvoid⁸³,
 M.F. Tripiana¹³, W. Trischuk¹⁶¹, B. Trocmé⁵⁸, A. Trofymov⁴⁵, C. Troncon^{94a}, M. Trotter-McDonald¹⁶,
 M. Trovatelli¹⁷², L. Truong^{167a,167c}, M. Trzebinski⁴², A. Trzupek⁴², K.W. Tsang^{62a}, J.C.-L. Tseng¹²²,
 P.V. Tsiareshka⁹⁵, G. Tsiopolitis¹⁰, N. Tsirintanis⁹, S. Tsiskaridze¹³, V. Tsiskaridze⁵¹,
 E.G. Tskhadadze^{54a}, K.M. Tsui^{62a}, I.I. Tsukerman⁹⁹, V. Tsulaia¹⁶, S. Tsuno⁶⁹, D. Tsybychev¹⁵⁰,
 Y. Tu^{62b}, A. Tudorache^{28b}, V. Tudorache^{28b}, T.T. Tulbure^{28a}, A.N. Tuna⁵⁹, S.A. Tupputi^{22a,22b},
 S. Turchikhin⁶⁸, D. Turgeman¹⁷⁵, I. Turk Cakir^{4b,au}, R. Turra^{94a,94b}, P.M. Tuts³⁸, G. Uccielli^{22a,22b},
 I. Ueda⁶⁹, M. Ughetto^{148a,148b}, F. Ukegawa¹⁶⁴, G. Unal³², A. Undrus²⁷, G. Unel¹⁶⁶, F.C. Ungaro⁹¹,
 Y. Unno⁶⁹, C. Unverdorben¹⁰², J. Urban^{146b}, P. Urquijo⁹¹, P. Urrejola⁸⁶, G. Usai⁸, J. Usui⁶⁹,
 L. Vacavant⁸⁸, V. Vacek¹³⁰, B. Vachon⁹⁰, C. Valderanis¹⁰², E. Valdes Santurio^{148a,148b},
 S. Valentineti^{22a,22b}, A. Valero¹⁷⁰, L. Valéry¹³, S. Valkar¹³¹, A. Vallier⁵, J.A. Valls Ferrer¹⁷⁰,

W. Van Den Wollenberg¹⁰⁹, H. van der Graaf¹⁰⁹, P. van Gemmeren⁶, J. Van Nieuwkoop¹⁴⁴, I. van Vulpen¹⁰⁹, M.C. van Woerden¹⁰⁹, M. Vanadia^{135a,135b}, W. Vandelli³², A. Vaniachine¹⁶⁰, P. Vankov¹⁰⁹, G. Vardanyan¹⁸⁰, R. Vari^{134a}, E.W. Varnes⁷, C. Varni^{53a,53b}, T. Varol⁴³, D. Varouchas¹¹⁹, A. Vartapetian⁸, K.E. Varvell¹⁵², J.G. Vasquez¹⁷⁹, G.A. Vasquez^{34b}, F. Vazeille³⁷, T. Vazquez Schroeder⁹⁰, J. Veatch⁵⁷, V. Veeraraghavan⁷, L.M. Veloce¹⁶¹, F. Veloso^{128a,128c}, S. Veneziano^{134a}, A. Ventura^{76a,76b}, M. Venturi¹⁷², N. Venturi¹⁶¹, A. Venturini²⁵, V. Vercesi^{123a}, M. Verducci^{136a,136b}, W. Verkerke¹⁰⁹, J.C. Vermeulen¹⁰⁹, M.C. Vetterli^{144,d}, N. Viaux Maira^{34b}, O. Viazlo⁸⁴, I. Vichou^{169,*}, T. Vickey¹⁴¹, O.E. Vickey Boeriu¹⁴¹, G.H.A. Viehhauser¹²², S. Viel¹⁶, L. Vigani¹²², M. Villa^{22a,22b}, M. Villaplana Perez^{94a,94b}, E. Vilucchi⁵⁰, M.G. Vinciter³¹, V.B. Vinogradov⁶⁸, A. Vishwakarma⁴⁵, C. Vittori^{22a,22b}, I. Vivarelli¹⁵¹, S. Vlachos¹⁰, M. Vlasak¹³⁰, M. Vogel¹⁷⁸, P. Vokac¹³⁰, G. Volpi^{126a,126b}, H. von der Schmitt¹⁰³, E. von Toerne²³, V. Vorobel¹³¹, K. Vorobev¹⁰⁰, M. Vos¹⁷⁰, R. Voss³², J.H. Vosseveld⁷⁷, N. Vranjes¹⁴, M. Vranjes Milosavljevic¹⁴, V. Vrba¹³⁰, M. Vreeswijk¹⁰⁹, R. Vuillermet³², I. Vukotic³³, P. Wagner²³, W. Wagner¹⁷⁸, J. Wagner-Kuhr¹⁰², H. Wahlberg⁷⁴, S. Wahrenmund⁴⁷, J. Wakabayashi¹⁰⁵, J. Walder⁷⁵, R. Walker¹⁰², W. Walkowiak¹⁴³, V. Wallangen^{148a,148b}, C. Wang^{35b}, C. Wang^{36b,aw}, F. Wang¹⁷⁶, H. Wang¹⁶, H. Wang³, J. Wang⁴⁵, J. Wang¹⁵², Q. Wang¹¹⁵, R. Wang⁶, S.M. Wang¹⁵³, T. Wang³⁸, W. Wang^{153,aw}, W. Wang^{36a}, Z. Wang^{36c}, C. Wanotayaroj¹¹⁸, A. Warburton⁹⁰, C.P. Ward³⁰, D.R. Wardrope⁸¹, A. Washbrook⁴⁹, P.M. Watkins¹⁹, A.T. Watson¹⁹, M.F. Watson¹⁹, G. Watts¹⁴⁰, S. Watts⁸⁷, B.M. Waugh⁸¹, A.F. Webb¹¹, S. Webb⁸⁶, M.S. Weber¹⁸, S.W. Weber¹⁷⁷, S.A. Weber³¹, J.S. Webster⁶, A.R. Weidberg¹²², B. Weinert⁶⁴, J. Weingarten⁵⁷, M. Weirich⁸⁶, C. Weiser⁵¹, H. Weits¹⁰⁹, P.S. Wells³², T. Wenaus²⁷, T. Wengler³², S. Wenig³², N. Wermes²³, M.D. Werner⁶⁷, P. Werner³², M. Wessels^{60a}, K. Whalen¹¹⁸, N.L. Whallon¹⁴⁰, A.M. Wharton⁷⁵, A.S. White⁹², A. White⁸, M.J. White¹, R. White^{34b}, D. Whiteson¹⁶⁶, F.J. Wickens¹³³, W. Wiedenmann¹⁷⁶, M. Wielers¹³³, C. Wiglesworth³⁹, L.A.M. Wiik-Fuchs²³, A. Wildauer¹⁰³, F. Wilk⁸⁷, H.G. Wilkens³², H.H. Williams¹²⁴, S. Williams¹⁰⁹, C. Willis⁹³, S. Willocq⁸⁹, J.A. Wilson¹⁹, I. Wingerter-Seez⁵, E. Winkels¹⁵¹, F. Winklmeier¹¹⁸, O.J. Winston¹⁵¹, B.T. Winter²³, M. Wittgen¹⁴⁵, M. Wobisch^{82,t}, T.M.H. Wolf¹⁰⁹, R. Wolff⁸⁸, M.W. Wolter⁴², H. Wolters^{128a,128c}, V.W.S. Wong¹⁷¹, S.D. Worm¹⁹, B.K. Wosiek⁴², J. Wotschack³², K.W. Wozniak⁴², M. Wu³³, S.L. Wu¹⁷⁶, X. Wu⁵², Y. Wu⁹², T.R. Wyatt⁸⁷, B.M. Wynne⁴⁹, S. Xella³⁹, Z. Xi⁹², L. Xia^{35c}, D. Xu^{35a}, L. Xu²⁷, B. Yabsley¹⁵², S. Yacoob^{147a}, D. Yamaguchi¹⁵⁹, Y. Yamaguchi¹²⁰, A. Yamamoto⁶⁹, S. Yamamoto¹⁵⁷, T. Yamanaka¹⁵⁷, M. Yamatani¹⁵⁷, K. Yamauchi¹⁰⁵, Y. Yamazaki⁷⁰, Z. Yan²⁴, H. Yang^{36c}, H. Yang¹⁶, Y. Yang¹⁵³, Z. Yang¹⁵, W-M. Yao¹⁶, Y.C. Yap⁸³, Y. Yasu⁶⁹, E. Yatsenko⁵, K.H. Yau Wong²³, J. Ye⁴³, S. Ye²⁷, I. Yeletsikh⁶⁸, E. Yigitbasi²⁴, E. Yildirim⁸⁶, K. Yorita¹⁷⁴, K. Yoshihara¹²⁴, C. Young¹⁴⁵, C.J.S. Young³², D.R. Yu¹⁶, J. Yu⁸, J. Yu⁶⁷, S.P.Y. Yuen²³, I. Yusuff^{30,ax}, B. Zabinski⁴², G. Zacharis¹⁰, R. Zaidan¹³, A.M. Zaitsev^{132,ak}, N. Zakharchuk⁴⁵, J. Zalieckas¹⁵, A. Zaman¹⁵⁰, S. Zambito⁵⁹, D. Zanzi⁹¹, C. Zeitnitz¹⁷⁸, A. Zemla^{41a}, J.C. Zeng¹⁶⁹, Q. Zeng¹⁴⁵, O. Zenin¹³², T. Ženiš^{146a}, D. Zerwas¹¹⁹, D. Zhang⁹², F. Zhang¹⁷⁶, G. Zhang^{36a,aa}, H. Zhang^{35b}, J. Zhang⁶, L. Zhang⁵¹, L. Zhang^{36a}, M. Zhang¹⁶⁹, P. Zhang^{35b}, R. Zhang²³, R. Zhang^{36a,av}, X. Zhang^{36b}, Y. Zhang^{35a}, Z. Zhang¹¹⁹, X. Zhao⁴³, Y. Zhao^{36b,ay}, Z. Zhao^{36a}, A. Zhemchugov⁶⁸, B. Zhou⁹², C. Zhou¹⁷⁶, L. Zhou⁴³, M. Zhou^{35a}, M. Zhou¹⁵⁰, N. Zhou^{35c}, C.G. Zhu^{36b}, H. Zhu^{35a}, J. Zhu⁹², Y. Zhu^{36a}, X. Zhuang^{35a}, K. Zhukov⁹⁸, A. Zibell¹⁷⁷, D. Zieminska⁶⁴, N.I. Zimine⁶⁸, C. Zimmermann⁸⁶, S. Zimmermann⁵¹, Z. Zinonos¹⁰³, M. Zinser⁸⁶, M. Ziolkowski¹⁴³, L. Živković¹⁴, G. Zobernig¹⁷⁶, A. Zoccoli^{22a,22b}, R. Zou³³, M. zur Nedden¹⁷, L. Zwalinski³².

¹ Department of Physics, University of Adelaide, Adelaide, Australia

² Physics Department, SUNY Albany, Albany NY, United States of America

³ Department of Physics, University of Alberta, Edmonton AB, Canada

⁴ (a) Department of Physics, Ankara University, Ankara; (b) Istanbul Aydin University, Istanbul; (c)

Division of Physics, TOBB University of Economics and Technology, Ankara, Turkey

⁵ LAPP, CNRS/IN2P3 and Université Savoie Mont Blanc, Annecy-le-Vieux, France

⁶ High Energy Physics Division, Argonne National Laboratory, Argonne IL, United States of America

⁷ Department of Physics, University of Arizona, Tucson AZ, United States of America

⁸ Department of Physics, The University of Texas at Arlington, Arlington TX, United States of America

⁹ Physics Department, National and Kapodistrian University of Athens, Athens, Greece

¹⁰ Physics Department, National Technical University of Athens, Zografou, Greece

¹¹ Department of Physics, The University of Texas at Austin, Austin TX, United States of America

¹² Institute of Physics, Azerbaijan Academy of Sciences, Baku, Azerbaijan

¹³ Institut de Física d'Altes Energies (IFAE), The Barcelona Institute of Science and Technology, Barcelona, Spain

¹⁴ Institute of Physics, University of Belgrade, Belgrade, Serbia

¹⁵ Department for Physics and Technology, University of Bergen, Bergen, Norway

¹⁶ Physics Division, Lawrence Berkeley National Laboratory and University of California, Berkeley CA, United States of America

¹⁷ Department of Physics, Humboldt University, Berlin, Germany

¹⁸ Albert Einstein Center for Fundamental Physics and Laboratory for High Energy Physics, University of Bern, Bern, Switzerland

¹⁹ School of Physics and Astronomy, University of Birmingham, Birmingham, United Kingdom

²⁰ ^(a) Department of Physics, Bogazici University, Istanbul; ^(b) Department of Physics Engineering, Gaziantep University, Gaziantep; ^(d) Istanbul Bilgi University, Faculty of Engineering and Natural Sciences, Istanbul; ^(e) Bahcesehir University, Faculty of Engineering and Natural Sciences, Istanbul, Turkey

²¹ Centro de Investigaciones, Universidad Antonio Narino, Bogota, Colombia

²² ^(a) INFN Sezione di Bologna; ^(b) Dipartimento di Fisica e Astronomia, Università di Bologna, Bologna, Italy

²³ Physikalisches Institut, University of Bonn, Bonn, Germany

²⁴ Department of Physics, Boston University, Boston MA, United States of America

²⁵ Department of Physics, Brandeis University, Waltham MA, United States of America

²⁶ ^(a) Universidade Federal do Rio De Janeiro COPPE/EE/IF, Rio de Janeiro; ^(b) Electrical Circuits Department, Federal University of Juiz de Fora (UFJF), Juiz de Fora; ^(c) Federal University of Sao Joao del Rei (UFSJ), Sao Joao del Rei; ^(d) Instituto de Fisica, Universidade de Sao Paulo, Sao Paulo, Brazil

²⁷ Physics Department, Brookhaven National Laboratory, Upton NY, United States of America

²⁸ ^(a) Transilvania University of Brasov, Brasov; ^(b) Horia Hulubei National Institute of Physics and Nuclear Engineering, Bucharest; ^(c) Department of Physics, Alexandru Ioan Cuza University of Iasi, Iasi; ^(d) National Institute for Research and Development of Isotopic and Molecular Technologies, Physics Department, Cluj Napoca; ^(e) University Politehnica Bucharest, Bucharest; ^(f) West University in Timisoara, Timisoara, Romania

²⁹ Departamento de Física, Universidad de Buenos Aires, Buenos Aires, Argentina

³⁰ Cavendish Laboratory, University of Cambridge, Cambridge, United Kingdom

³¹ Department of Physics, Carleton University, Ottawa ON, Canada

³² CERN, Geneva, Switzerland

³³ Enrico Fermi Institute, University of Chicago, Chicago IL, United States of America

³⁴ ^(a) Departamento de Física, Pontificia Universidad Católica de Chile, Santiago; ^(b) Departamento de Física, Universidad Técnica Federico Santa María, Valparaíso, Chile

³⁵ ^(a) Institute of High Energy Physics, Chinese Academy of Sciences, Beijing; ^(b) Department of Physics, Nanjing University, Jiangsu; ^(c) Physics Department, Tsinghua University, Beijing 100084,

China

³⁶ ^(a) Department of Modern Physics and State Key Laboratory of Particle Detection and Electronics, University of Science and Technology of China, Anhui; ^(b) School of Physics, Shandong University, Shandong; ^(c) Department of Physics and Astronomy, Key Laboratory for Particle Physics, Astrophysics and Cosmology, Ministry of Education; Shanghai Key Laboratory for Particle Physics and Cosmology, Shanghai Jiao Tong University, Shanghai(also at PKU-CHEP);, China

³⁷ Université Clermont Auvergne, CNRS/IN2P3, LPC, Clermont-Ferrand, France

³⁸ Nevis Laboratory, Columbia University, Irvington NY, United States of America

³⁹ Niels Bohr Institute, University of Copenhagen, Kobenhavn, Denmark

⁴⁰ ^(a) INFN Gruppo Collegato di Cosenza, Laboratori Nazionali di Frascati; ^(b) Dipartimento di Fisica, Università della Calabria, Rende, Italy

⁴¹ ^(a) AGH University of Science and Technology, Faculty of Physics and Applied Computer Science, Krakow; ^(b) Marian Smoluchowski Institute of Physics, Jagiellonian University, Krakow, Poland

⁴² Institute of Nuclear Physics Polish Academy of Sciences, Krakow, Poland

⁴³ Physics Department, Southern Methodist University, Dallas TX, United States of America

⁴⁴ Physics Department, University of Texas at Dallas, Richardson TX, United States of America

⁴⁵ DESY, Hamburg and Zeuthen, Germany

⁴⁶ Lehrstuhl für Experimentelle Physik IV, Technische Universität Dortmund, Dortmund, Germany

⁴⁷ Institut für Kern- und Teilchenphysik, Technische Universität Dresden, Dresden, Germany

⁴⁸ Department of Physics, Duke University, Durham NC, United States of America

⁴⁹ SUPA - School of Physics and Astronomy, University of Edinburgh, Edinburgh, United Kingdom

⁵⁰ INFN Laboratori Nazionali di Frascati, Frascati, Italy

⁵¹ Fakultät für Mathematik und Physik, Albert-Ludwigs-Universität, Freiburg, Germany

⁵² Departement de Physique Nucleaire et Corpusculaire, Université de Genève, Geneva, Switzerland

⁵³ ^(a) INFN Sezione di Genova; ^(b) Dipartimento di Fisica, Università di Genova, Genova, Italy

⁵⁴ ^(a) E. Andronikashvili Institute of Physics, Iv. Javakhishvili Tbilisi State University, Tbilisi; ^(b) High Energy Physics Institute, Tbilisi State University, Tbilisi, Georgia

⁵⁵ II Physikalisches Institut, Justus-Liebig-Universität Giessen, Giessen, Germany

⁵⁶ SUPA - School of Physics and Astronomy, University of Glasgow, Glasgow, United Kingdom

⁵⁷ II Physikalisches Institut, Georg-August-Universität, Göttingen, Germany

⁵⁸ Laboratoire de Physique Subatomique et de Cosmologie, Université Grenoble-Alpes, CNRS/IN2P3, Grenoble, France

⁵⁹ Laboratory for Particle Physics and Cosmology, Harvard University, Cambridge MA, United States of America

⁶⁰ ^(a) Kirchoff-Institut für Physik, Ruprecht-Karls-Universität Heidelberg, Heidelberg; ^(b)

Physikalisches Institut, Ruprecht-Karls-Universität Heidelberg, Heidelberg; ^(c) ZITI Institut für technische Informatik, Ruprecht-Karls-Universität Heidelberg, Mannheim, Germany

⁶¹ Faculty of Applied Information Science, Hiroshima Institute of Technology, Hiroshima, Japan

⁶² ^(a) Department of Physics, The Chinese University of Hong Kong, Shatin, N.T., Hong Kong; ^(b)

Department of Physics, The University of Hong Kong, Hong Kong; ^(c) Department of Physics and Institute for Advanced Study, The Hong Kong University of Science and Technology, Clear Water Bay, Kowloon, Hong Kong, China

⁶³ Department of Physics, National Tsing Hua University, Taiwan, Taiwan

⁶⁴ Department of Physics, Indiana University, Bloomington IN, United States of America

⁶⁵ Institut für Astro- und Teilchenphysik, Leopold-Franzens-Universität, Innsbruck, Austria

⁶⁶ University of Iowa, Iowa City IA, United States of America

⁶⁷ Department of Physics and Astronomy, Iowa State University, Ames IA, United States of America

- 68 Joint Institute for Nuclear Research, JINR Dubna, Dubna, Russia
- 69 KEK, High Energy Accelerator Research Organization, Tsukuba, Japan
- 70 Graduate School of Science, Kobe University, Kobe, Japan
- 71 Faculty of Science, Kyoto University, Kyoto, Japan
- 72 Kyoto University of Education, Kyoto, Japan
- 73 Research Center for Advanced Particle Physics and Department of Physics, Kyushu University, Fukuoka, Japan
- 74 Instituto de Física La Plata, Universidad Nacional de La Plata and CONICET, La Plata, Argentina
- 75 Physics Department, Lancaster University, Lancaster, United Kingdom
- 76 ^(a) INFN Sezione di Lecce; ^(b) Dipartimento di Matematica e Fisica, Università del Salento, Lecce, Italy
- 77 Oliver Lodge Laboratory, University of Liverpool, Liverpool, United Kingdom
- 78 Department of Experimental Particle Physics, Jožef Stefan Institute and Department of Physics, University of Ljubljana, Ljubljana, Slovenia
- 79 School of Physics and Astronomy, Queen Mary University of London, London, United Kingdom
- 80 Department of Physics, Royal Holloway University of London, Surrey, United Kingdom
- 81 Department of Physics and Astronomy, University College London, London, United Kingdom
- 82 Louisiana Tech University, Ruston LA, United States of America
- 83 Laboratoire de Physique Nucléaire et de Hautes Energies, UPMC and Université Paris-Diderot and CNRS/IN2P3, Paris, France
- 84 Fysiska institutionen, Lunds universitet, Lund, Sweden
- 85 Departamento de Física Teórica C-15, Universidad Autónoma de Madrid, Madrid, Spain
- 86 Institut für Physik, Universität Mainz, Mainz, Germany
- 87 School of Physics and Astronomy, University of Manchester, Manchester, United Kingdom
- 88 CPPM, Aix-Marseille Université and CNRS/IN2P3, Marseille, France
- 89 Department of Physics, University of Massachusetts, Amherst MA, United States of America
- 90 Department of Physics, McGill University, Montreal QC, Canada
- 91 School of Physics, University of Melbourne, Victoria, Australia
- 92 Department of Physics, The University of Michigan, Ann Arbor MI, United States of America
- 93 Department of Physics and Astronomy, Michigan State University, East Lansing MI, United States of America
- 94 ^(a) INFN Sezione di Milano; ^(b) Dipartimento di Fisica, Università di Milano, Milano, Italy
- 95 B.I. Stepanov Institute of Physics, National Academy of Sciences of Belarus, Minsk, Republic of Belarus
- 96 Research Institute for Nuclear Problems of Byelorussian State University, Minsk, Republic of Belarus
- 97 Group of Particle Physics, University of Montreal, Montreal QC, Canada
- 98 P.N. Lebedev Physical Institute of the Russian Academy of Sciences, Moscow, Russia
- 99 Institute for Theoretical and Experimental Physics (ITEP), Moscow, Russia
- 100 National Research Nuclear University MEPhI, Moscow, Russia
- 101 D.V. Skobeltsyn Institute of Nuclear Physics, M.V. Lomonosov Moscow State University, Moscow, Russia
- 102 Fakultät für Physik, Ludwig-Maximilians-Universität München, München, Germany
- 103 Max-Planck-Institut für Physik (Werner-Heisenberg-Institut), München, Germany
- 104 Nagasaki Institute of Applied Science, Nagasaki, Japan
- 105 Graduate School of Science and Kobayashi-Maskawa Institute, Nagoya University, Nagoya, Japan
- 106 ^(a) INFN Sezione di Napoli; ^(b) Dipartimento di Fisica, Università di Napoli, Napoli, Italy
- 107 Department of Physics and Astronomy, University of New Mexico, Albuquerque NM, United States

of America

¹⁰⁸ Institute for Mathematics, Astrophysics and Particle Physics, Radboud University Nijmegen/Nikhef, Nijmegen, Netherlands

¹⁰⁹ Nikhef National Institute for Subatomic Physics and University of Amsterdam, Amsterdam, Netherlands

¹¹⁰ Department of Physics, Northern Illinois University, DeKalb IL, United States of America

¹¹¹ Budker Institute of Nuclear Physics, SB RAS, Novosibirsk, Russia

¹¹² Department of Physics, New York University, New York NY, United States of America

¹¹³ Ohio State University, Columbus OH, United States of America

¹¹⁴ Faculty of Science, Okayama University, Okayama, Japan

¹¹⁵ Homer L. Dodge Department of Physics and Astronomy, University of Oklahoma, Norman OK, United States of America

¹¹⁶ Department of Physics, Oklahoma State University, Stillwater OK, United States of America

¹¹⁷ Palacký University, RCPTM, Olomouc, Czech Republic

¹¹⁸ Center for High Energy Physics, University of Oregon, Eugene OR, United States of America

¹¹⁹ LAL, Univ. Paris-Sud, CNRS/IN2P3, Université Paris-Saclay, Orsay, France

¹²⁰ Graduate School of Science, Osaka University, Osaka, Japan

¹²¹ Department of Physics, University of Oslo, Oslo, Norway

¹²² Department of Physics, Oxford University, Oxford, United Kingdom

¹²³ ^(a) INFN Sezione di Pavia; ^(b) Dipartimento di Fisica, Università di Pavia, Pavia, Italy

¹²⁴ Department of Physics, University of Pennsylvania, Philadelphia PA, United States of America

¹²⁵ National Research Centre "Kurchatov Institute" B.P.Konstantinov Petersburg Nuclear Physics Institute, St. Petersburg, Russia

¹²⁶ ^(a) INFN Sezione di Pisa; ^(b) Dipartimento di Fisica E. Fermi, Università di Pisa, Pisa, Italy

¹²⁷ Department of Physics and Astronomy, University of Pittsburgh, Pittsburgh PA, United States of America

¹²⁸ ^(a) Laboratório de Instrumentação e Física Experimental de Partículas - LIP, Lisboa; ^(b) Faculdade de Ciências, Universidade de Lisboa, Lisboa; ^(c) Department of Physics, University of Coimbra, Coimbra; ^(d) Centro de Física Nuclear da Universidade de Lisboa, Lisboa; ^(e) Departamento de Física, Universidade do Minho, Braga; ^(f) Departamento de Física Teórica y del Cosmos and CAFPE, Universidad de Granada, Granada; ^(g) Dep Física and CEFITEC of Faculdade de Ciências e Tecnologia, Universidade Nova de Lisboa, Caparica, Portugal

¹²⁹ Institute of Physics, Academy of Sciences of the Czech Republic, Praha, Czech Republic

¹³⁰ Czech Technical University in Prague, Praha, Czech Republic

¹³¹ Charles University, Faculty of Mathematics and Physics, Prague, Czech Republic

¹³² State Research Center Institute for High Energy Physics (Protvino), NRC KI, Russia

¹³³ Particle Physics Department, Rutherford Appleton Laboratory, Didcot, United Kingdom

¹³⁴ ^(a) INFN Sezione di Roma; ^(b) Dipartimento di Fisica, Sapienza Università di Roma, Roma, Italy

¹³⁵ ^(a) INFN Sezione di Roma Tor Vergata; ^(b) Dipartimento di Fisica, Università di Roma Tor Vergata, Roma, Italy

¹³⁶ ^(a) INFN Sezione di Roma Tre; ^(b) Dipartimento di Matematica e Fisica, Università Roma Tre, Roma, Italy

¹³⁷ ^(a) Faculté des Sciences Ain Chock, Réseau Universitaire de Physique des Hautes Energies - Université Hassan II, Casablanca; ^(b) Centre National de l'Énergie des Sciences Techniques Nucleaires, Rabat; ^(c) Faculté des Sciences Semlalia, Université Cadi Ayyad, LPHEA-Marrakech; ^(d) Faculté des Sciences, Université Mohamed Premier and LPTPM, Oujda; ^(e) Faculté des sciences, Université Mohammed V, Rabat, Morocco

- ¹³⁸ DSM/IRFU (Institut de Recherches sur les Lois Fondamentales de l'Univers), CEA Saclay (Commissariat à l'Energie Atomique et aux Energies Alternatives), Gif-sur-Yvette, France
- ¹³⁹ Santa Cruz Institute for Particle Physics, University of California Santa Cruz, Santa Cruz CA, United States of America
- ¹⁴⁰ Department of Physics, University of Washington, Seattle WA, United States of America
- ¹⁴¹ Department of Physics and Astronomy, University of Sheffield, Sheffield, United Kingdom
- ¹⁴² Department of Physics, Shinshu University, Nagano, Japan
- ¹⁴³ Department Physik, Universität Siegen, Siegen, Germany
- ¹⁴⁴ Department of Physics, Simon Fraser University, Burnaby BC, Canada
- ¹⁴⁵ SLAC National Accelerator Laboratory, Stanford CA, United States of America
- ¹⁴⁶ ^(a) Faculty of Mathematics, Physics & Informatics, Comenius University, Bratislava; ^(b) Department of Subnuclear Physics, Institute of Experimental Physics of the Slovak Academy of Sciences, Kosice, Slovak Republic
- ¹⁴⁷ ^(a) Department of Physics, University of Cape Town, Cape Town; ^(b) Department of Physics, University of Johannesburg, Johannesburg; ^(c) School of Physics, University of the Witwatersrand, Johannesburg, South Africa
- ¹⁴⁸ ^(a) Department of Physics, Stockholm University; ^(b) The Oskar Klein Centre, Stockholm, Sweden
- ¹⁴⁹ Physics Department, Royal Institute of Technology, Stockholm, Sweden
- ¹⁵⁰ Departments of Physics & Astronomy and Chemistry, Stony Brook University, Stony Brook NY, United States of America
- ¹⁵¹ Department of Physics and Astronomy, University of Sussex, Brighton, United Kingdom
- ¹⁵² School of Physics, University of Sydney, Sydney, Australia
- ¹⁵³ Institute of Physics, Academia Sinica, Taipei, Taiwan
- ¹⁵⁴ Department of Physics, Technion: Israel Institute of Technology, Haifa, Israel
- ¹⁵⁵ Raymond and Beverly Sackler School of Physics and Astronomy, Tel Aviv University, Tel Aviv, Israel
- ¹⁵⁶ Department of Physics, Aristotle University of Thessaloniki, Thessaloniki, Greece
- ¹⁵⁷ International Center for Elementary Particle Physics and Department of Physics, The University of Tokyo, Tokyo, Japan
- ¹⁵⁸ Graduate School of Science and Technology, Tokyo Metropolitan University, Tokyo, Japan
- ¹⁵⁹ Department of Physics, Tokyo Institute of Technology, Tokyo, Japan
- ¹⁶⁰ Tomsk State University, Tomsk, Russia
- ¹⁶¹ Department of Physics, University of Toronto, Toronto ON, Canada
- ¹⁶² ^(a) INFN-TIFPA; ^(b) University of Trento, Trento, Italy
- ¹⁶³ ^(a) TRIUMF, Vancouver BC; ^(b) Department of Physics and Astronomy, York University, Toronto ON, Canada
- ¹⁶⁴ Faculty of Pure and Applied Sciences, and Center for Integrated Research in Fundamental Science and Engineering, University of Tsukuba, Tsukuba, Japan
- ¹⁶⁵ Department of Physics and Astronomy, Tufts University, Medford MA, United States of America
- ¹⁶⁶ Department of Physics and Astronomy, University of California Irvine, Irvine CA, United States of America
- ¹⁶⁷ ^(a) INFN Gruppo Collegato di Udine, Sezione di Trieste, Udine; ^(b) ICTP, Trieste; ^(c) Dipartimento di Chimica, Fisica e Ambiente, Università di Udine, Udine, Italy
- ¹⁶⁸ Department of Physics and Astronomy, University of Uppsala, Uppsala, Sweden
- ¹⁶⁹ Department of Physics, University of Illinois, Urbana IL, United States of America
- ¹⁷⁰ Instituto de Física Corpuscular (IFIC) and Departamento de Física Atómica, Molecular y Nuclear and Departamento de Ingeniería Electrónica and Instituto de Microelectrónica de Barcelona

(IMB-CNM), University of Valencia and CSIC, Valencia, Spain

¹⁷¹ Department of Physics, University of British Columbia, Vancouver BC, Canada

¹⁷² Department of Physics and Astronomy, University of Victoria, Victoria BC, Canada

¹⁷³ Department of Physics, University of Warwick, Coventry, United Kingdom

¹⁷⁴ Waseda University, Tokyo, Japan

¹⁷⁵ Department of Particle Physics, The Weizmann Institute of Science, Rehovot, Israel

¹⁷⁶ Department of Physics, University of Wisconsin, Madison WI, United States of America

¹⁷⁷ Fakultät für Physik und Astronomie, Julius-Maximilians-Universität, Würzburg, Germany

¹⁷⁸ Fakultät für Mathematik und Naturwissenschaften, Fachgruppe Physik, Bergische Universität Wuppertal, Wuppertal, Germany

¹⁷⁹ Department of Physics, Yale University, New Haven CT, United States of America

¹⁸⁰ Yerevan Physics Institute, Yerevan, Armenia

¹⁸¹ CH-1211 Geneva 23, Switzerland

¹⁸² Centre de Calcul de l'Institut National de Physique Nucléaire et de Physique des Particules (IN2P3), Villeurbanne, France

^a Also at Department of Physics, King's College London, London, United Kingdom

^b Also at Institute of Physics, Azerbaijan Academy of Sciences, Baku, Azerbaijan

^c Also at Novosibirsk State University, Novosibirsk, Russia

^d Also at TRIUMF, Vancouver BC, Canada

^e Also at Department of Physics & Astronomy, University of Louisville, Louisville, KY, United States of America

^f Also at Physics Department, An-Najah National University, Nablus, Palestine

^g Also at Department of Physics, California State University, Fresno CA, United States of America

^h Also at Department of Physics, University of Fribourg, Fribourg, Switzerland

ⁱ Also at II Physikalisches Institut, Georg-August-Universität, Göttingen, Germany

^j Also at Departament de Física de la Universitat Autònoma de Barcelona, Barcelona, Spain

^k Also at Departamento de Física e Astronomia, Faculdade de Ciências, Universidade do Porto, Portugal

^l Also at Tomsk State University, Tomsk, Russia

^m Also at The Collaborative Innovation Center of Quantum Matter (CICQM), Beijing, China

ⁿ Also at Università di Napoli Parthenope, Napoli, Italy

^o Also at Institute of Particle Physics (IPP), Canada

^p Also at Horia Hulubei National Institute of Physics and Nuclear Engineering, Bucharest, Romania

^q Also at Department of Physics, St. Petersburg State Polytechnical University, St. Petersburg, Russia

^r Also at Borough of Manhattan Community College, City University of New York, New York City, United States of America

^s Also at Centre for High Performance Computing, CSIR Campus, Rosebank, Cape Town, South Africa

^t Also at Louisiana Tech University, Ruston LA, United States of America

^u Also at Institutio Catalana de Recerca i Estudis Avancats, ICREA, Barcelona, Spain

^v Also at Graduate School of Science, Osaka University, Osaka, Japan

^w Also at Fakultät für Mathematik und Physik, Albert-Ludwigs-Universität, Freiburg, Germany

^x Also at Institute for Mathematics, Astrophysics and Particle Physics, Radboud University Nijmegen/Nikhef, Nijmegen, Netherlands

^y Also at Department of Physics, The University of Texas at Austin, Austin TX, United States of America

^z Also at Institute of Theoretical Physics, Ilia State University, Tbilisi, Georgia

^{aa} Also at CERN, Geneva, Switzerland

^{ab} Also at Georgian Technical University (GTU), Tbilisi, Georgia

- ac* Also at Ochadai Academic Production, Ochanomizu University, Tokyo, Japan
- ad* Also at Manhattan College, New York NY, United States of America
- ae* Also at Departamento de Física, Pontificia Universidad Católica de Chile, Santiago, Chile
- af* Also at Department of Physics, The University of Michigan, Ann Arbor MI, United States of America
- ag* Also at Academia Sinica Grid Computing, Institute of Physics, Academia Sinica, Taipei, Taiwan
- ah* Also at School of Physics, Shandong University, Shandong, China
- ai* Also at Departamento de Física Teórica y del Cosmos and CAFPE, Universidad de Granada, Granada, Portugal
- aj* Also at Department of Physics, California State University, Sacramento CA, United States of America
- ak* Also at Moscow Institute of Physics and Technology State University, Dolgoprudny, Russia
- al* Also at Departement de Physique Nucleaire et Corpusculaire, Université de Genève, Geneva, Switzerland
- am* Also at Institut de Física d'Altes Energies (IFAE), The Barcelona Institute of Science and Technology, Barcelona, Spain
- an* Also at School of Physics, Sun Yat-sen University, Guangzhou, China
- ao* Also at Institute for Nuclear Research and Nuclear Energy (INRNE) of the Bulgarian Academy of Sciences, Sofia, Bulgaria
- ap* Also at Faculty of Physics, M.V.Lomonosov Moscow State University, Moscow, Russia
- aq* Also at Institute of Physics, Academia Sinica, Taipei, Taiwan
- ar* Also at National Research Nuclear University MEPhI, Moscow, Russia
- as* Also at Department of Physics, Stanford University, Stanford CA, United States of America
- at* Also at Institute for Particle and Nuclear Physics, Wigner Research Centre for Physics, Budapest, Hungary
- au* Also at Giresun University, Faculty of Engineering, Turkey
- av* Also at CPPM, Aix-Marseille Université and CNRS/IN2P3, Marseille, France
- aw* Also at Department of Physics, Nanjing University, Jiangsu, China
- ax* Also at University of Malaya, Department of Physics, Kuala Lumpur, Malaysia
- ay* Also at LAL, Univ. Paris-Sud, CNRS/IN2P3, Université Paris-Saclay, Orsay, France
- * Deceased